Computational Modelling and Experimental Verification of Quasioptical Components at Millimetre Wavelengths

Presented by

Paul McLaughlin, B.Sc.

A thesis submitted for the degree of

Master of Science

Department of Experimental Physics
National University of Ireland, Maynooth
Co. Kildare
Ireland

Head of Department
Professor J. Anthony Murphy, M.Sc., M.S., Ph.D
Research Supervisor
Dr. Neil Trappe, B.Sc., Ph.D.

May 2014

Contents

Abstract

This thesis describes various analysis techniques used in the optical characterisation of millimetre wave radiation. The results presented relate to both computational simulation and exerimental measurements carried out at NUI Maynooth. The majority of the analysis is centred around a frequency of 100 GHz, or a corresponding wavelength of 3 mm. Experimental measurements were performed on diffractive optical elements known as axicons, and the results were presented and compared with simulations. An introduction to KID devices was given, along with their potential uses and a potential analysis method using CST was outlined. These techniques using plane wave illumination in CST were compared and verified with Gaussian Beam Mode Analysis. A method of analysing the form of standing waves present in a system involving metallic rings was described. A method previously used for the analysis of standing waves between feedhorns was adapted to examine the form of the modes present in the resonant Fabry-Perot cavity. Detailed analysis was performed using CST, a full electromagnetic modelling package on resonant metallic cavities related to describing a waveguide coupled bolometer for the SAFARI instrument on the proposed SPICA space telescope mission. A cavity geometry was optimsed manually for optimum cavity size and absorber size and location by performing a large number of simulations. SCATTER, an in-house mode matching software was used to verify the results from CST in a simple case. Various other cavity geometries were also investigated briefly. A simplified cavity model which could potentially be manufactured to perform measurements at NUI maynooth was outlined, as well as a potential detector method known as a patch antenna. Patch antennas were designed for use at 100 GHz and briefly examined in operation within a cavity using CST.

Acknowledgements

I owe a lot of gratitude to a number of people for helping me along the way.

Firstly, I would like to thank Dr. Neil Trappe, my supervisor, for all the help over the past two years, and also throughout my four years as an undergraduate. Your door was always open, and you were always eager to assist in any way you could, in a patient and understanding way. Also to Prof. Anthony Murphy, for placing the facilities of the department at my disposal.

Thanks must also go to the entire staff of the Experimental Physics department at NUI Maynooth. All of those who lectured me as an undergraduate, in particular Dr. Frank Mulligan, Dr. Créidhe O'Sullivan and Dr. Michael Cawley. Thanks also to Dr. Marcin Grądziel, for his help with running experimental meaurements in the THz laboratory and along the way as a lecturer. Also to Mr. John Kelly for always being there to help when there were technology problems, Pat Seery for helping out in the lab and letting me use his workshop, and to Derek Gleeson for making sure I had enough teaching hours to keep me going. And to Gráinne Roche, for helping out with virtually anything, and keeping us all organised! Thanks again to everyone in the department for all of the interesting conversations over coffee!

Thanks also to all my fellow postrgads, in particular those who I shared an office with at one time or another. Darragh and Stephen- there was always some Physics talk, but more non-Physics talk, and always the welcome distraction of a coffee trip. Anthony and Darragh, I miss some of those very strange conversations. To Darragh in particular, thanks for being a great office mate for two years and a good friend for longer.

Thanks also to those who I shared that house in Parklands with throughout the two years. Brian and Donnacha, thanks for all the kitchen games, late night or early morning! And Brian- thanks for being a friend since school- I'm not following you any more! And Deirdre, thanks for being there for me, and putting up with my moods throughout, especially towards the most stressful parts at the end.

Last but not least, to my family, for always being there to help me out along the way, and always believing in me. To my Mum and Dad, my sister Tracy

and my brother Karol, thanks.

Chapter 1

Introduction

1.1 Introduction to Millimetre Wave Optics

Millimetre-wave optics describes the branch of optics concerned with the region of the electromagnetic spectrum where the wavelength, λ, is of the order of 1 mm. In fact, we often extend the phrase "millimetre-wave" to shorter wavelengths and into the "terahertz" region, where the wavelength can be much shorter than 1 mm. Therefore, when terahertz radiation is spoken of, or indeed sub-mm astronomy, we are dealing with the same approximate region of the spectrum, where similar techniques are applicable. The region of interest for our purposes is variously described in the literature as "mm-wave", "sub-mm", "terahertz" and "far-infrared". For example, when we are at the far end of the terahertz regime at frequencies of around 10 THz, the wavelength is around 3×10^{-5} m or .03 mm. Clearly, by definition, this is not millimetre-wavelength radiation. However, we can largely apply very similar techniques and approaches as would be used at wavelengths of 1 mm, although we will generally not discuss radiation of such high frequencies. In fact, for the work carried out and discussed in this thesis, we deal primarily with radiation having a wavelength of 3 mm, or a frequency of 100 GHz. In this thesis, for example, SAFARI, a proposed spectrometer mission to map astronomical sources operates from 1-10 THz, which is truly in the terahertz frequency range. The majority of the experimental and simulation work presented in this thesis is centred at aound 100 GHz or a wavelength, λ, of 3 mm which could be defined as millimetre wave but the boundary between both regimes is not well defined.

In figure 1.1 we see a very detailed illustration of the electromagnetic spec-

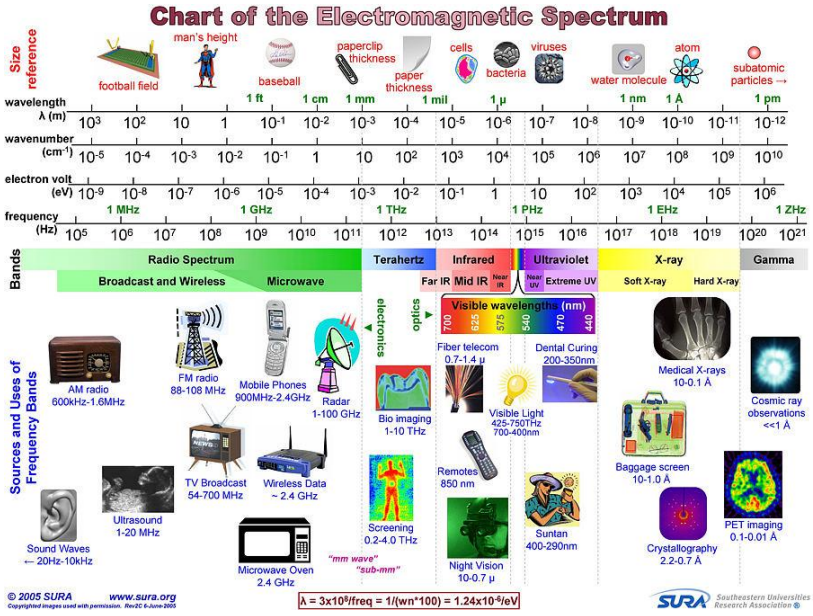

Figure 1.1: Detailed diagram showing electromagnetic spectrum and applications. Source: [1].

trum. We note that this diagram defines the terahertz band as beginning at wavelengths of very slightly more than 1 mm, hence our previous discussion of varying definitions of the regions of the spectrum. We see, then, that the terahertz region is not merely confined to frequencies of 1-10 THz, as one might imagine. One intuitive, and perhaps the most instructive definition of our region of interest is that of the region "between electronics and optics", i.e. it is the region between where electronics are useful, in the form of radio wavelength electronic circuits, and that where traditional optics is useful, e.g. classical lenses and mirrors. As we note from figure 1.1, the terahertz region is sandwiched between the microwave, where electronic circuits are useful, and infrared and visible optics, where classical optics is used. The region is also sometimes referred to as the "terahertz gap", partly perhaps because it exists in the gap between these two methods of analysis, and also because there has been relatively little technological advancement in this area, in comparison to many other regions of the electromagnetic spectrum. In section 1.2, we shall describe applications relevant to various different areas of the broadly defined region of the terahertz region of the electromagnetic spectrum. An important characteristic which increases the scope of potential uses of terahertz radiation is the fact that it is non-ionising, and therefore is not harmful to biological tissue. This is in contrast to many common testing and scanning techniques which utilise higher energy X-ray photons.

1.2 Millimetre Wave Optics and its Applications

1.2.1 Commercial Applications

Millimetre-wave and terahertz technology has been employed and is widely being developed for a wide range of commercial applications, including security, food production and art. Figure 1.2 details the use of frequency modulated continuous wave (FMCW) scanning at 600 GHz for use in battlefiled security checkpoints and aiport security screenings. This research was performed at the Jet Propulsion Laboratory, California [2]. The image shows a person carrying an item with the characteristics of a pipe bomb, strapped to the chest and concealed with clothing. The bottom right panel of the figure then overlays the resulting image produced by the 1 second scan onto the image of the person. It is then clear that the person is carrying a concealed weapon.

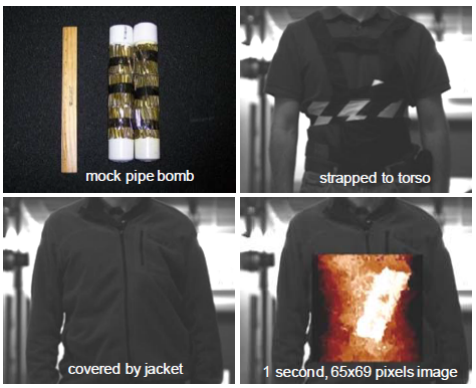

Figure 1.2: Security scanner image detailing the real-time detection of concealed weaponry. Source [2].

Another application with similar potential uses is that of narcotic detection [3]. In figure 1.3, three spectral profiles are shown across the 1-2 THz range. These represent samples of two illegal drugs; MDMA and methamphetamine, along with a sample of aspirin. The drugs were contained in polyethylene bags placed inside a paper envelope. This indicates the potential use of such technology in screening mail containing illegal drugs, as the spectral profiles of each drug can easily be distinguished. Also, the use may be extended to screening for explosives, as each explosive will also contain its own spectral fingerprint. The non-ionising nature of terahertz radiation also lends itself to applications in non-destructive testing of samples. These may include

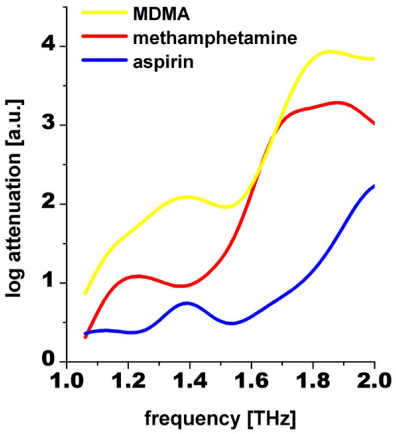

Figure 1.3: Security scanner image detailing the real-time detection of narcotics using spectral fingerprints. Source: [3].

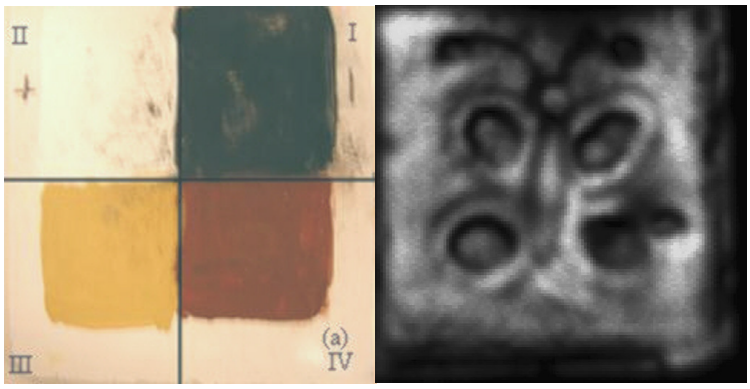

Figure 1.4: Visible image and time-domain integration THz reflection image from a plaster/graphite/plaster interface. Source: [4].

food samples in a quality assurance environment or in the non-destructive testing of works of art, as shown in figure 1.4 [4]. In this experiment, a graphite image was produced on a layer of plaster. This was then covered by another plaster layer, and subsequently painted over, using four different pigmentations. The reconstructed image produced from the experiment shows an ability to clearly distinguish the image of the butterfly without the need to damage the piece. It was also found that the three different colours of paint used produced spectral profiles which were readily differentiable. This experiment was performed over the range from approximately 0.1-1 THz. Numerous commercial applications exist for this technology. For example, antique paintings will often have been restored with newer paint, and will contain numerous layers of paint. It would be possible with this technology to differentiate these layers and to view the underlying images, without the requirement of destructively removing the topmost layers.

1.2.2 Medicine

Applications of terahertz and millimetre-wave radiation are becoming more widespread, with many technologies being tested for viability in biological aplications [5, 6]. Terahertz technology has been shown to be potentially very useful for the diagnosis of cancer in humans. In [7], terahertz pulse imaging was used to study basal cell carcinoma ex vivo, in a noninvasive manner, and some results of this are shown in figure 1.5. The diseased tissue (on the left of each image) is bounded by a solid black line, while the normal tissue is bounded by a dashed black line.

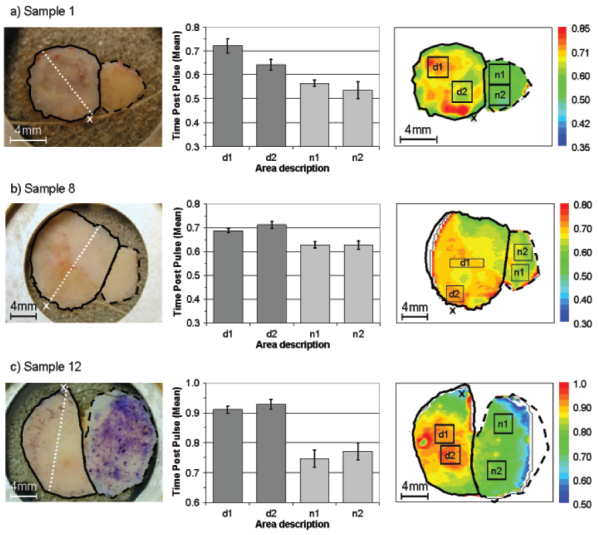

Figure 1.5: Visible (left) and terahertz (right) images of diseased samples. Source: [7].

The diseased areas of tissue showed increased absorption levels, and indeed fine structural details. This increased absorption may be due to an increase in the interstitial water within the diseased tissue, or a change in the vibrational modes of water molecules with other functional groups [7].

An in-line measurement technique for determining the coating thickness of individual pharmaceutical tablets during film coating in a pan coating unit using pulsed terahertz technology has been described [8]. Using this method, it is possible to measure film coating thicknesses of between 40 μm-1 mm with sub-micron resolution, with an ability to assess the thickness of a single tablet in less than 9 ms during the process, without interfering with the coating process.

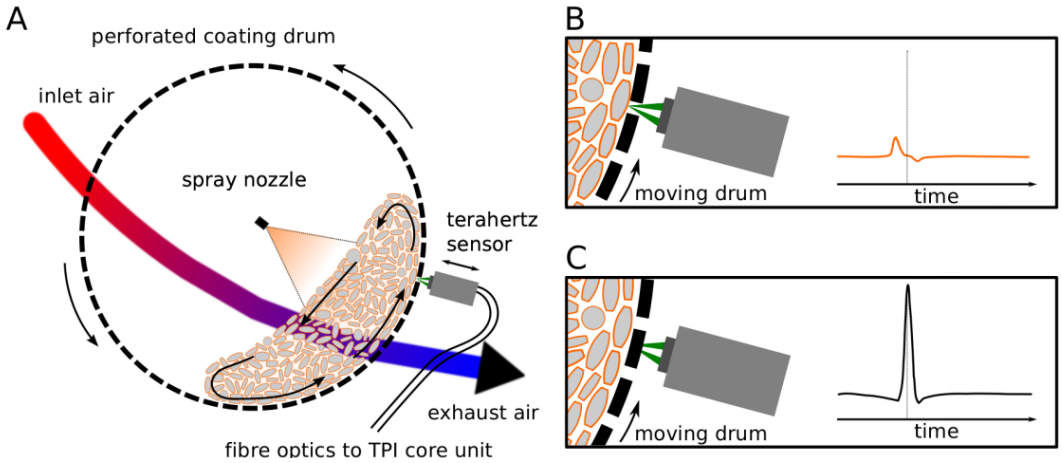

Figure 1.6: Tablet coating system in moving drum showing fitted in-line THz sensor. Source: [8].

1.2.3 Astronomy

Sub-mm and far infrared astronomy has been largely publicised in recent years. This is due to the large number of projects launched and those currently in development. The Herschel and Planck space telescopes were launched together in 2009, and NUIM had a large involvement in the development of components for both telescopes. There is also heavy involvement in SAFARI, an instrument on the proposed JAXA-ESA mission SPICA, and QUBIC, a ground-based experiment which will measure polarisation anisotropies in the Cosmic Microwave Background. Another ground based experiment which had involvement from Maynooth is ALMA; a large interferometric array of radio telescopes, which can be moved to create numerous diferent baselines (figure 1.7).

Figure 1.7: Image showing ALMA in the Atacama desert in Northern Chile.

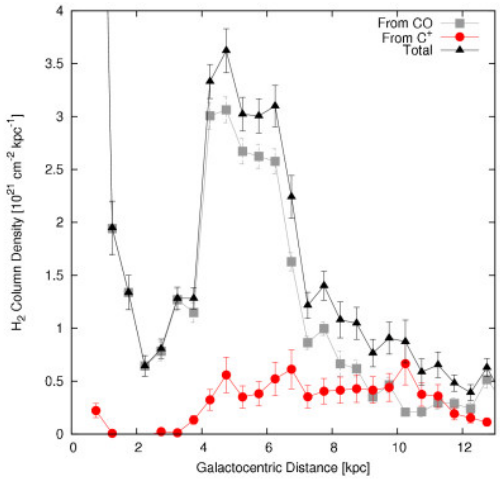

Figure 1.8: Distribution of molecular gas across the plane of the Milky Way. Source: [9].

Figure 1.8 is a plot produced as a result of observations with the HIFI instrument on the Herschel Space Observatory, the optics for which were partly designed at NUI Maynooth. The plot shows the distribution of molecular gas across the plane of the Milky Way as a function of distance from the Galactic Centre. The graph shows the density of molecular gas as probed via two different indirect tracers: carbon monoxide (CO) shown in grey, and ionised carbon (C^+) shown in red. The cumulative distribution, taking into account both components, is shown in black. The use of C^+ as a tracer, instead of just CO suggest that almost one third of all molecular gas in the Milky Way had remained undetected until now [9].

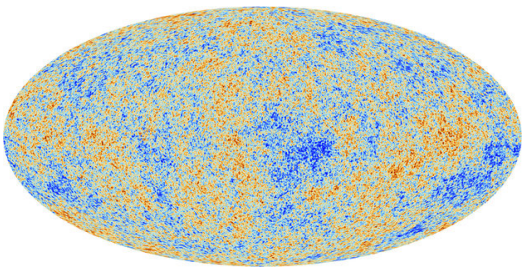

Figure 1.9: CMB anisotropies, observed by Planck. Source: [10].

Figure 1.9 shows the Planck all-sky map, released in March 2013. The image is based on the initial 15.5 months of data from Planck, and constitutes the most detailed map of the cosmic microwave background; the leftover radiation from the Big Bang. This map shows tiny temperature fluctuations that correspond to regions of slightly different densities. One of the most surprising findings is that the fluctuations in the CMB temperatures at large angular scales do not match those predicted by the standard model- their sig-

nals are not as strong as expected from the smaller scale structure revealed by Planck [10].

Figure 1.10 shows a basic illustration of the QUBIC telescope setup, which is still in the design phase. Radiation from the sky, which passes though a feed-horn array, is transformed by telescope optics and focused onto a bolometer array. The aim of QUBIC is to detect so-called "E" (even parity) and "B" (odd parity) modes. It is the "B" modes which are of particular interest, as these would imply an inflationary universe [11].

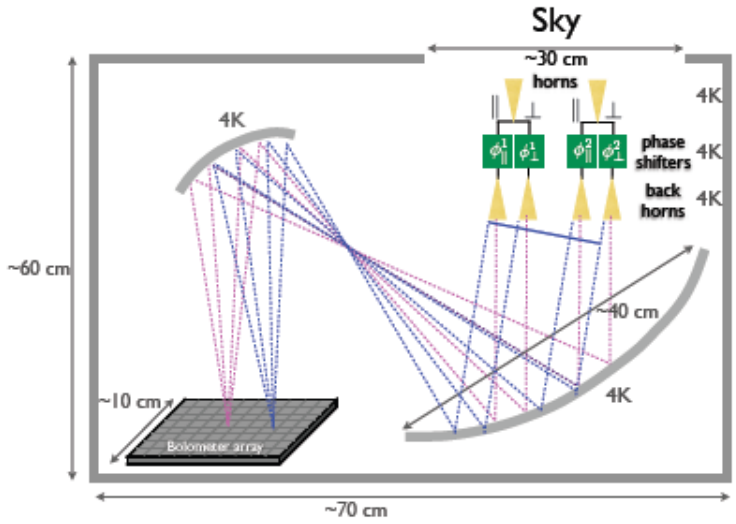

Figure 1.10: Ilustration of QUBIC focal plane. Source: [11].

The analysis techniques presented in this thesis are used to design, analyse and verify the receivers for such projects, and indeed some of this analysis will be specifically presented in relation to the SAFARI project, in chapter 6.

1.3 Outline of Thesis

- **Chapter 2**

  Chapter 2 introduces the background theory appropriate to describe the propagation of mm-wave radiation. The Gaussian beam mode theory will be introduced and developed, and specific mathematical techniques will be described. The principles behind an electromagnetic simulation

package will be discussed, as well as a description of measurement techniques in the mm-wave regime, and specific concepts which will be used in subsequent chapters.

- **Chapter 3**
  Chapter 3 briefly describes the principles behind Kinetic Inductance Detectors, and outlines useful contributions that may be made in the optical design of the system. A method of plane wave illummination is also described, which would be of use in modelling such a system in astronomy related applications.

- **Chapter 4**
  Chapter 4 introduces pseudo- Bessel beams at millimetre wavelengths and uses Gaussian Beam Mode Analysis to analyse axicons, quasioptical components which can be used in the production of such beams. Experimental measurements are performed on such components, and the results analysed.

- **Chapter 5**
  Chapter 5 describes multiple reflections between two metallic rings or discs. Simulations are performed on a model system, and results presented for a variety of setups. The form of the modes present inside a resonant Fabry-Perot cavity is analysed.

- **Chapter 6**
  Chapter 6 introduces the background to the SAFARI space telescope instrument, and analysis is performed on a resonant metallic cavity of various geometries, in most cases containing absorber material. A simplification of the system is outlined, which could potentially be manufactured and analysed.

- **Chapter 7**
  Chapter 7 provides conclusions on the work cariried out in this thesis.

1.4 Author's Specific Contribution to Thesis

Chapter 3

Gaussian Beam mode analysis (GBMA) of an axicon element of varying

geometries has been performed. A relatively simple process for creating a collimated beam has been outlined, without the need for off-axis optics as are often used, which dramatically add to the size of the optical system. One axicon has been designed and manufactured, and measurements and analysis were performed on both this and an existing axicon. Measurements have also been performed with a corrugated horn.

Chapter 4

A potential contribution from Maynooth in the development of imaging technology employing Kinetic Inductance Detectors is detailed. A comparison of plane wave analysis techniques in CST was undertaken.

Chapter 5

A simple resonant system involving metallic rings or discs has been modelled using GBMA. A matrix analysis technique used for the analysis of feedhorn propagation modes has been adapted to the analysis of resonant modes inside a Fabry-Perot cavity.

Chapter 6

A simple cavity geometry including absorber material was optimised through simulations performed using the commercial software package CST. This cavity analysis was extrapolated to cavities of alternative geometies. Computational analysis was also performed on a possible detector method in a simple physical model of such a cavity.

Chapter 2

Theory

2.1 Quasioptics

Geometrical optics is the technique used to describe the propagation of electromagnetic radiation in the visible region, where the assumption that $\lambda \approx 0$, where λ is the wavelength, is a valid approximation, i.e. where the value of λ is of the order of ≈ 500 nm. The assumption made by the geometrical optics theory is that, because the wavelength of the radiation is so small with respect to the size of the optical components used, it can be treated as tending towards zero.
When the dimensions of the components of the system are of the order of λ however, effects such as diffraction become important and can in fact dominate the propagation of radiation through optical trains.

In the mm-wave region of the spectrum, we are closer to the second case, as the system dimensions are moderately large compared with λ. In this case, due to the limited accuracy of geometrical optics we would benefit from a full electromagnetic treatment of the problem, where Maxwell's equations are computed fully. However, this is computationally intensive, and we find that other less intensive methods are accurate and computationally less exhaustive than solving differential equations continuously, but are still highly useful for many purposes. This allows for the use of the elegant theory of Gaussian Beam Mode Analysis (GBMA), where the effects of diffraction are included within reasonable limits and a scalar aproximation is used. An important point of note regarding GBMA is that a large number of antenna types used

at mm-wavelengths have a high Gaussicity, and so are naturally represented using this convention.

2.2 Gaussian Beam Mode (GBM) Theory

Gaussian Beam Mode theory was first widely used in the area of laser beam propagation [12], where light beams are usually very well collimated. They are also of great interest for our purposes of quasioptical propagation and analysis in millimetre systems. Later we will analyse the form of Laser cavity modes using this elegant technique.

2.2.1 Derivation of Freespace Gaussian Beam Modes

The propagation of electromagnetic fields in free space is governed by the scalar wave equation [13]

$$[\bigtriangledown^2 + k^2]\tilde{E}(x, y, z) = 0, \tag{2.1}$$

where $\tilde{E}(x, y, z)$ is the complex amplitude of a sinusoidally varying field in three-dimensional space and k is the wavenumber, defined as equal to $2\pi/\lambda$, where λ is the wavelength of the radiation. We mainly concern ourselves with beams propagating primarily in the z-direction by convention, so that the primary spatial dependence of $\tilde{E}(x, y, z)$ will be of the form $exp(-jkz)$. We can write the distribution for any component of the electric field then (where we have suppressed the time dependence) as

$$E(x, y, z) = u(x, y, z)exp(-jkz), \tag{2.2}$$

where u is a complex scalar function that defines the non-plane wave part of the beam, and the exponential term represents the spatial variation of a plane wave. Substituting this into equation 2.1 yields the *reduced wave equation* [14]

$$\frac{\delta^2 E}{\delta x^2} + \frac{\delta^2 E}{\delta y^2} + \frac{\delta^2 E}{\delta z^2} + k^2 E = 0. \tag{2.3a}$$

or, using the quasi-plane wave solution:

$$\frac{\delta^2 E}{\delta x^2} + \frac{\delta^2 E}{\delta y^2} + \frac{\delta^2 E}{\delta z^2} - 2jk\frac{\delta u}{\delta z} = 0. \tag{2.3b}$$

The assumption we will now make using *the paraxial approximation* is that the variation of the amplitude, u, along the direction of propagation will be small over distances of the order of a wavelength, and that the axial variation will be small compared to the variation perpendicular to this direction [15]. Due to *the paraxial approximation* then, and as each of the second partial derivative terms in equation 2.3b are much smaller than the fourth term, the second partial derivative involving z in particular may be dropped. This leaves what is termed the *paraxial wave equation*

$$\frac{\delta^2 E}{\delta x^2} + \frac{\delta^2 E}{\delta y^2} - 2jk\frac{\delta u}{\delta z} = 0. \tag{2.4}$$

2.2.2 Gaussian Modes

The solutions to the paraxial wave equation are the so-called Gaussian Beam Modes, the use of which is extremely widespread in quasioptical design and analysis [16, 17, 18]. A complex scalar field, (E), may be described using a linear superposition of modes (Ψ), weighted by the appropriate mode coefficients (A):

$$E = \sum_{0}^{n} A_n \Psi_n. \tag{2.5}$$

Ψ_n is an independently propagating free-space mode of order n and A_n is a mode coefficient which determines how much power is contained in the mode's transverse amplitude distribution. These coefficients may be determined by performing an appropriate overlap integral between the field and the mode set at a plane where the scalar electric field is known. The overlap integral in question takes the form [19]:

$$A_n = \int \Psi_n^* dA \tag{2.6}$$

To describe the field at an alternative plane simply involves propagating the modes and re-summing to construct the new field. The methods of calculating the specific parameters required to reconstruct the beam at an alternative plane will be outlined in section 2.4.

2.3 Gaussian Spherical Waves

We wish to have an analytical form for the solutions to the paraxial wave equation as follows. If we consider a uniform spherical wave diverging from a point source at x_0, y_0, z_0 incident on a point on a plane x, y, z, then if the axial distance $z - z_0$ is large in comparison to the transverse components x_0, y_0 and x, y then the field distribution at x, y, z can be written using the paraxial approximation as [12]

$$\begin{aligned}\tilde{u}(x,y,z) &= \frac{1}{z-z_0} exp\left[-jk\frac{(x-x_0)^2+(y-y_0)^2}{2(z-z_0)}\right] \\ &= \frac{1}{R(z)} exp\left[-jk\frac{(x-x_0)^2+(y-y_0)^2}{2R(z)}\right],\end{aligned} \tag{2.7}$$

where $R(z)$ is the radius of curvature of the wave as a function of z.Thus, the phase variation of this wave will have a form given by

$$\phi(x,y,z) = k\frac{(x-x_0)^2+(y-y_0)^2}{2R(z)}. \tag{2.8}$$

The radius of curvature at a plane z can be written as

$$R(z) = R_0 + z - z_0 \tag{2.9}$$

where R_0 is the radius of curvature at the source plane. If the radius of curvature $R > 0$, we say that the wave is diverging, whereas if $R < 0$, the wave is said to be converging. The phase variation given by equation 2.8 is only valid in the paraxial limit. We can assume that x_0 and y_0 are zero for simplicity and introduce the concept of a *complex point source* by including a complex quantity q_0, where $q(z) = q_0 + (z - z_0)$. We call $q(z)$ the complex beam parameter or complex radius of curvature, and we shall use it to replace the radius of curvature, $R(z)$. Equation 2.7 now becomes

$$\tilde{u}(x,y,z) = \frac{1}{q(z)} exp\left[-jk\frac{x^2+y^2}{2(q(z))}\right] \tag{2.10}$$

If $q(z)$ is complex, the real and imaginary parts may be separated to give the complex form $a + ib$

$$\frac{1}{q(z)} = \frac{1}{q_r(z)} - j\frac{1}{qim(z)}. \tag{2.11}$$

Then equation 2.10 can be written as

$$\tilde{u}(x,y,z) = \frac{1}{q(z)} exp\left[-jk\frac{x^2+y^2}{2(q_{re}(z))}\right] - k\frac{x^2+y^2}{2(q_{im}(z))} \tag{2.12}$$

This has an imaginary phase variation corresponding to a spherical wave with a real radius of curvature and also a purely real quadratic phase variation, giving a Gaussian amplitude profile with a transverse fall off described by the imaginary part of $1/q(z)$.

We assume that the field has a distribution of the exponential form as in equation 2.10 and allow equation 2.11 to take the form of a fundamental Gaussican distribution. Then the real part of $1/q(z)$ is equal to the phase radius of curvature and the imaginary part represents the Gaussian variation in off-axis amplitude we find that

$$\frac{1}{q(z)} = \frac{1}{R(z)} - j\left(\frac{\lambda}{\pi w(z)^2}\right), \tag{2.13}$$

where $w(z)$ is the beam width. $q(z)$ then varies with distance as

$$q(z) = q(0) + (z - z_0) \tag{2.14}$$

We can also use a differential approach by assuming a trial solution to the paraxial wave equation of the form [14]

$$u(x, y, z) = A(z)exp\left[-jk\frac{x^2 + y^2}{2q(z)}\right], \tag{2.15}$$

where $A(z)$ and $q(z)$ are unknown but complex. Substituting into the paraxial wave equation we obtain

$$\left(\frac{k}{2}\right)^2\left(\frac{dq(z)}{dz} - 1\right)(x^2 + y^2) - \left(\frac{2jk}{q(z)}\right)\left(\frac{q(z)}{A(z)}\frac{dA(z)}{dz} + 1\right) \tag{2.16}$$

This equation can only be satisfied for all x and y if

$$\frac{dq(z)}{dz} = 1 \tag{2.17a}$$

and

$$\frac{dA(z)}{dz} = -\frac{A(z)}{q(z)}. \tag{2.17b}$$

The solutions to these are given by [12]

$$q(z) = q(0) + (z - z_0) \tag{2.18a}$$

and

$$\frac{A(z)}{A_0} = \frac{q_0}{q(z)}, \tag{2.18b}$$

which is the same solution as found in equation 2.14, showing the validiity of this approach.

2.4 Gaussian Beam Mode solution in Cylindrical Coordinates

We now wish to derive the GBM solution applicable to systems having cylindrical symmetry, e.g. a cylindrical aperture. We will use r to represent the radial distance from the axis of propagation (z- axis) and φ for the azimuthal angle. Rewriting equation 2.15 in terms of polar coordinates, but assuming an axially symmetric solution, i.e. independent of φ we have:

$$u(r,z) = A(z)exp\left[\frac{-jkr^2}{2q(z)}\right]. \tag{2.19}$$

Substituting into the paraxial wave equation we find the same result as in equations 2.18a, 2.18b. Again, substituting the real and imaginary parts of $1/q(z)$ into equation 2.19, we find that the exponential term becomes [14]

$$exp\left[\left(\frac{-jkr^2}{2}\right)\left(\frac{1}{q_r(z)}\right) - \left(\frac{kr^2}{2}\right)\left(\frac{1}{q_{im}(z)}\right)\right]. \tag{2.20}$$

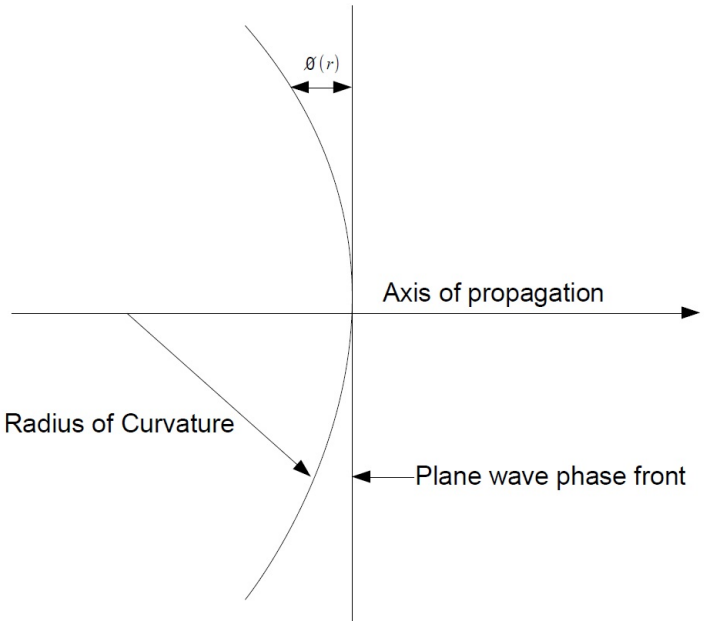

Figure 2.1: Phase variation of a spherical wave relative to a plane wave front.

The imaginary phase term has a spherical radius of curvature, R, and we now replace the real part of $q(z)$ with R, and define $\Phi(r)$ to be the phase variation relative to a plane wave at a plane z_0 as a function of r, as shown in figure 2.1.

The phase variation in the limit $r << R$ is described by [14]:

$$\Phi(r) = \frac{\pi r^2}{\lambda R} = \frac{kr^2}{2R}. \tag{2.21}$$

From 2.20 we can make the important equality of the real part of $1/q$ with the radius of curvaure of the beam

$$\left(\frac{1}{q_r}\right) = \frac{1}{R} \tag{2.22}$$

As q is a function of z, clearly the radius of curvature of the beam will depend on the position along the propagation axis.

The second part of the exponential expression in 2.20 is real and has a Gaussian variation as a function of distance from the axis of propagation. Taking the standard form for a Gaussian distribution

$$f(r) = f(0)exp\left[-\left(\frac{r}{r_0}\right)^2\right], \tag{2.23}$$

we may note that r_0 represents the distance to the $1/e$ point relative to the on-axis field value. To give this form to the second part of 2.20 we take

$$\left(\frac{1}{q}\right)_{im} = \frac{2}{kw^2(z)} = \frac{\lambda}{\pi w^2}, \tag{2.24}$$

defining the *beam radius*, w, which is the value of the radius at which the field falls to $1/e$ relative to its on-axis value. The beam radius as well as the radius of curvature will depend on the position along the axis of propagation. We thus see that the complete function q is given by

$$\frac{1}{q(z)} = \frac{1}{R(z)} - j\left(\frac{\lambda}{\pi w(z)^2}\right), \tag{2.25}$$

with R and w functions of z. Equation 2.25 is the same as equation 2.13, and emerges in this case from the differential approach used here. When $z = 0$ and $w(0) = [\lambda q(0)/j\pi]$, we get that 2.19 becomes

$$u(r,0) = u(0,0)exp\left(-\frac{r^2}{w_0^2}\right), \tag{2.26}$$

where w_0 is the beam width at $z = 0$, which is called the *beam waist radius*. From this definition, and from equation 2.18a we obtain:

$$q = \frac{j\pi w_0^2}{\lambda} + z. \tag{2.27}$$

From equations 2.25 and 2.27 we can find both the radius of curvature and the beam radius as a function of position along the axis of propagation:

$$R = z + \frac{1}{z}\left(\frac{\pi w_0^2}{\lambda}\right)^2 \tag{2.28a}$$

$$w = w_0\left[1 + \left(\frac{\lambda z}{\pi w_0^2}\right)^2\right]^{0.5} \tag{2.28b}$$

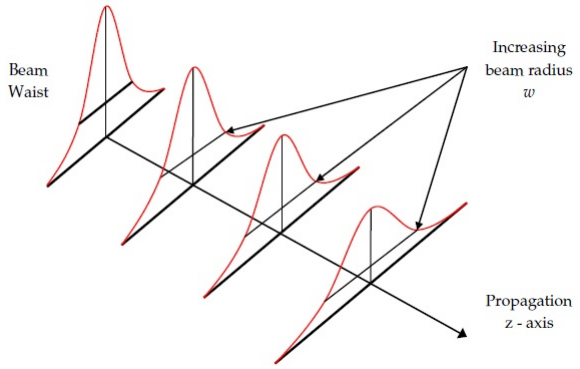

Figure 2.2: Amplitude variation of a Gaussian beam upon propagation. Source: [20]

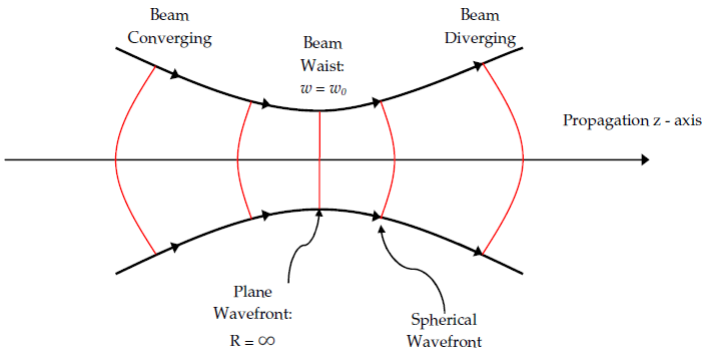

Figure 2.3: Variation of radius of curvature of a Gaussian beam upon propagation.Source: [20]

The beam waist radius is the minimum value of the beam radius and occurs at the beam waist, where the radius of curvature is infinite. Here, we effectively have a plane wave front. Figure 2.2 shows the variation of the amplitude of a Gaussian beam as it propagates. Figure 2.3 shows the variation of the radius of curvature of a Gaussian beam as it propagates. The quantity $\pi w_0^2/\lambda$ is known as the *confocal distance*. This will be described again later in section 2.7.2.

To complete the analysis of the Gaussian Beam equation, rewriting equations 2.17a and 2.17b, we have that $dA/A = -dz/q$ and $dz = q$. We infer that

$A(z)/A(0) = q(0)/q(z)$ and examining equation 2.27, we find that

$$\frac{A(z)}{A(0)} = \frac{1 + \frac{j\lambda z}{\pi w_0^2}}{1 + \left(\frac{\lambda z}{\pi w_0^2}\right)^2}. \tag{2.29}$$

We can express this in terms of a phasor, and defining

$$tan\phi_0 = \frac{\lambda z}{\pi w_0^2}, \tag{2.30}$$

we see that

$$\frac{A(z)}{A(0)} = \frac{w_0}{w} exp(j\phi_0). \tag{2.31}$$

Taking the amplitude on-axis to be unity, we have the complete expression for the fundamental Gaussian beam mode

$$u(r,z) = \frac{w_0}{w} exp\left(\frac{-r^2}{w^2} - \frac{j\pi r^2}{\lambda R} + j\phi_0\right) \tag{2.32}$$

The description for the electric field then can be obtained from equation 2.2, and simply involves including a plane wave phase factor, yielding

$$E(r,z) = \left(\frac{w_0}{w}\right) exp\left(\frac{-r^2}{w^2} - jkz - \frac{j\pi r^2}{\lambda R} + j\phi_0\right). \tag{2.33}$$

2.5 Normalization

To relate the exression above for the electric field to the total power in a Gaussian beam, we assume that the electric and magnetic field components are related to each other as in a plane wave. The total power, then, is proportional to the square of the electric field integrated over the area of the beam. For convenience, we normalize by setting $\int |E|^2 \cdot 2\pi r = 1$. Using equation 2.33 for E, evaluating at $z = 0$, we obtain equation 2.34

$$E(r,z) = \left(\frac{2}{\pi w_0^2}\right)^{0.5} exp\left(\frac{-r^2}{w^2} - jkz - \frac{j\pi r^2}{\lambda R} + j\phi_0\right), \tag{2.34}$$

which, along with the previously defined equations 2.28a, 2.28b and 2.30 fully describe the fundamental mode Gaussian Beam.

2.6 Higher order solutions

The fundamental Gaussian beam solution is very important in quasioptical analysis, but we also often require higher order modes to increase the accuracy of our analysis. Such solutions have certain polynomials superimposed on the fundamental mode field distribution. The higher order beam modes have the property of having a beam radius and a beam radius of curvature that have the same value as the fundamental mode, but their phase shifts are different. In cylindrical coordinates, higher order beam modes are used to better describe radiating systems that have axial symmetry but do not have perfectly Gaussian radiation patterns, e.g. corrugated feedhorns. Higher order beam modes in rectangular coordinates can also be useful where Cartesian symmetry exists.

It turns out that in cylindrical coordinates it is the Laguerre polynomials which will be important, whereas in rectangular coordinates it is the Hermite polynomials which are used. A solution to the paraxial wave equation in cylindrical coordinates is given by

$$\begin{aligned} E_{pm}(r,\varphi,z) = &\left[\frac{2p!}{\pi(p+m)!}\right]^{0.5} \frac{1}{w(z)} \left[\frac{\sqrt{2}r}{w(z)}\right]^{m} L_{pm}\left(\frac{2r^2}{w^2(z)}\right) \\ \cdot exp&\left[\frac{-r^2}{w^2(z)} - jkz - \frac{j\pi r^2}{\lambda R(z)} - j(2p+m+1)\phi_0(z)\right] \cdot exp(jm\varphi), \end{aligned} \tag{2.35}$$

where p is the radial index, m is the angular index, and L_{pm} is the generalized Laguerre polynomial. A significant point to note about the higher order mode field distribution is that the contribution to the overall phase shift is greater than that for the fundamental mode by an amount proportional to the mode parameters. These higher order Gaussian beam mode solutions are normalized so that each represents unit power flow, and obey the orthogonality relationship

$$\iint r \;\; drd\varphi E_{pm}(r,\varphi,z) = \delta_{pq}\delta_{mn}. \tag{2.36}$$

If we wish to consider axially symmtric modes(i.e. those that are independent of φ), we consides the modes described by equation 2.36 which have $m = 0$. These may be used to describe systems which are axially symmetric but which are not exactly described by the fundamental Gaussian Beam mode. These particular modes may be given by

$$E_{p0}(r,z) = \left[\frac{2}{\pi w^2}\right]^{0.5} L_{p0}\left(\frac{2r^2}{w^2}\right) exp\left[-\frac{r^2}{w^2} - jkz - \frac{j\pi r^2}{\lambda R} + j(2p+1)\phi_0\right]. \tag{2.37}$$

An example where we would not be able to make this simplification is that of a cylindrical smooth-walled horn. In this case the electric field is not radially symmetric, and would require Laguerre modes of order $m = 0$ and $m = 2$ to have an accurate description of the aperture field.

2.7 Propagation of Gaussian Beams

2.7.1 Edge Taper

The fundamental Gaussian beam mode has a Gaussian distribution of the electric field perpendicular to the propagation axis, and everywhere along this axis:

$$\frac{|E(r,z)|}{|E(0,z)|} = exp\left[-\frac{r}{w}^2\right], \tag{2.38}$$

[14] where r is the distance from the axis of propagation. The power density distribution is just proportional to this quantity squared:

$$\frac{P(r)}{P(0)} = exp\left[-2\left(\frac{r}{w}^2\right)\right], \tag{2.39}$$

and this also has a Gaussian profile. This can become confusing as we use the width of the field distribution to characterize the beam, although it is more often the power distribution which is measured directly. However, we use w to mean the distance from the axis of propagation at which the field has fallen to $1/e$ of its value on-axis. We define the *Edge Taper*, T_e to be the relative power density at a radius r_e, and it is given by

$$T_e(r_e) = exp\left(\frac{-2r_e^2}{w^2}\right). \tag{2.40}$$

Usually, the edge taper is quoted in decibels to accommodate a large dynamic range, and thus we have

$$T_e(dB) = -10log_{10}(T_e). \tag{2.41}$$

As an example,for a truncating aperture for a fundamental mode Gaussian beam, the edge taper at a radius from the centre of the beam equal to w is -8.7 dB. Alternatively, this means that 86.47 % of the power in the fundamental mode beam is contained within a diameter of $2w$. For the fundamental mode Gaussian in cylindrical coordinates, the fraction of total power contained

within a circle of radius r_e centred on the beam axis is found to be

$$F_e = \int_{r=0}^{r=r_e} |E(r)|^2 \cdot 2\pi r dr = 1 - T_e(r_e). \tag{2.42}$$

The particular formulation of equation 2.42 will be useful later (section 3.2) when we discuss axicons, and the method of illumination of this optical component.

2.7.2 Confocal Distance

The parameter known as the *confocal distance*, or sometimes the *Rayleigh range* is of particular importance. It is defined as [12, 14, 21]

$$z_c = \frac{\pi w_0^2}{\lambda}. \tag{2.43}$$

Using this definition for the confocal distance, the Gaussian beam parameters may be rewritten as

$$R = z + \frac{z_c^2}{z}, \tag{2.44a}$$

$$w = w_0 \left[1 + \left(\frac{z}{z_c}\right)^2\right]^{0.5}, \tag{2.44b}$$

$$\phi_0 = tan^{-1}\left(\frac{z}{z_c}\right). \tag{2.44c}$$

We can see from this that R, w, and ϕ_0 all change significantly between the beam waist at $z = 0$ and the confocal distance at $z = z_c$. We generally define the confocal distance as being the transition region between the "near field" ($z << z_c$) and the "far field"($z >> z_c$) of the propagating beam.
At the beam waist, the beam radius w reaches its minimum value w_0. The electric field and power distributions have their maximum on-axis values there, and the radius of curvature is infinite (as the phase front is planar). Recall that the phase shift is the on-axis phase of a Gaussian beam relative to a plane wave. Thus, it is zero at the beam waist. Another feature of the near field is that the beam radius changes only slowly relative to waist value, and the beam is said to remain essentially *collimated* within the confocal distance.

2.8 Gaussian Beam Transformation

We previously noted that a Gaussian beam will spread or diverge significantly upon propagation of a distance of the order of the confocal distance. When designing a quasioptical system therefore, it is important to confine the beam. The methods used are similar in principle to those used in standard geometrical optics, e.g. lenses or mirrors may be used to force a beam to converge rather than diverge for a certain distance.

By the nature of the radiation, we cannot usually achieve a "focus" in the sense of concentrating to a point. In reality what is done is to transform one beam waist to another waist, as in figure 2.4. We will now introduce a useful method for tracking the evolution of a Gaussian beam through simple quasioptical systems. This will be applied later in section 3.2 where we will use the method to track the evolution of beams through systems involving axicons. This method may also be used in other situations where we use GBMA, as it is a useful and simple method. If it is used, it will explicitly be stated that "ABCD matrices" are used.

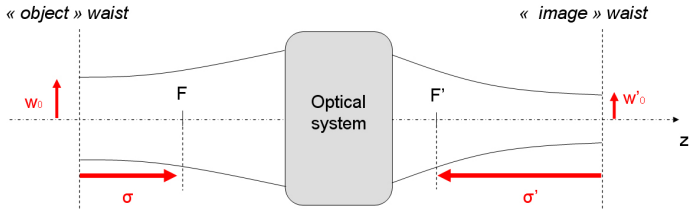

Figure 2.4: Variation of radius of curvature of a Gaussian beam upon propagation.

2.8.1 Ray Transfer Matrices

In the classical "ABCD" method, the location and slope of a ray at the output plane of a paraxial system are linear functions of the parameters of the input ray. This relationship is [14]:

$$\begin{aligned} r_{out} &= A \cdot r_{in} + B \cdot r_{in}^{'} \\ r_{out}^{'} &= C \cdot r_{in} + D \cdot r_{in}^{'}, \end{aligned} \tag{2.45}$$

where r is the position and r' is the slope. This can be described using matrix notation if the ray position and slope are treated as a column matrix,

using

$$\begin{bmatrix} r_{out} \\ r'_{out} \end{bmatrix} = \begin{bmatrix} A & B \\ C & D \end{bmatrix} \cdot \begin{bmatrix} r_{in} \\ r'_{in}. \end{bmatrix} \tag{2.46}$$

A system with any number of elements can be handled by multiplying the individual 2 x 2 matrices. The radius of curvature is defined as $R = r/r'$, thus

$$R_{out} = \frac{A \cdot R_{in} + B}{C \cdot R_{in} + D} \tag{2.47}$$

Extending to Gaussian beams, we have an analagous relation, where the four parameters describing an element of the optical system operate instead on the complex radius of curvature:

$$q_{out} = \frac{A \cdot q_{in} + B}{C \cdot q_{in} + D}. \tag{2.48}$$

The 2 x 2 matrix consisting of the elements A, B, C and D is known as the *ray transfer matrix* of the system. When combining elements using multiple ABCD matrices, we use the convention that the matrices are cascaded in reverse order to that in which they are encountered by the beam, so that the first element encountered by the beam will be represented by the rightmost element in the cascade as it is written. Using the equation for the complex beam parameter, 2.25 , we can determine the beam radius, and the radius of curvature, using

$$w_{out} = \left[\frac{\lambda}{\pi Im(-1/q_{out})}\right]^{0.5} = \sqrt{\left[\frac{-\lambda}{\pi Im\left(\frac{C + D/R_{in} - jD\lambda/\pi w_{in}^2}{A + B/R_{in} - jB\lambda/\pi w_{in}^2}\right)}\right]} \tag{2.49}$$

and

$$R_{out} = Re\left(\frac{1}{q}\right)^{-1} = Re\left(\frac{C + D/R_{in} - jD\lambda/\pi w_{in}^2)}{A + B/R_{in} - jB\lambda/\pi w_{in}^2}\right)^{-1}. \tag{2.50}$$

The most basic ray transfer matrix is that for propagation of length L in a medium of uniform refractive index. As shown in 2.5, the offset of the incoming ray is changed by an amount depending on r'_{in}, but the slope remains the same, in this case. The ray transfer matrix, or *ABCD Matrix* for the propagation of a ray through a uniform medium, then, is given by

$$M_{freesp.} = \begin{bmatrix} 1 & L \\ 0 & 1 \end{bmatrix}. \tag{2.51}$$

Other ABCD matrices may be constructed for increasingly complex elements, such as transitions between media of varying refractive indices, thin lenses,

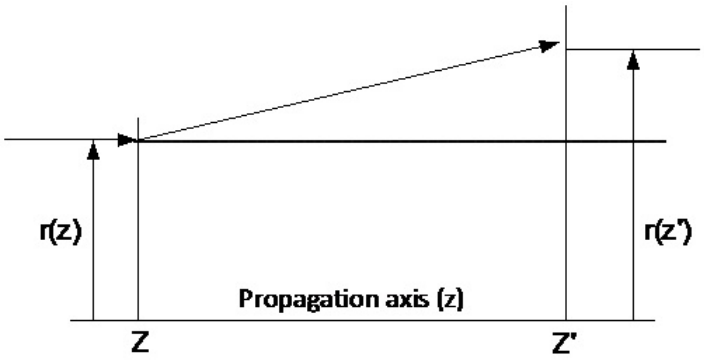

Figure 2.5: Propagation of a ray in free space.

etc., and these can be cascaded to find the system matrix.

As an example, we will take the case of a spherical mirror, of focal length 500 mm. For a beam with initial radius of 4 mm and radius of curvature of 80 mm at a wavelength of 3 mm (100 GHz). We can construct a $2f$ system using ABCD matrices, such that the final cascaded system matrix is given by:

$$M_{sys.} = \begin{bmatrix} 1 & 500 \\ 0 & 1 \end{bmatrix} \cdot \begin{bmatrix} 1 & 0 \\ -2/1000 & 1 \end{bmatrix} \cdot \begin{bmatrix} 1 & 500 \\ 0 & 1 \end{bmatrix} = \begin{bmatrix} 1 & 500 \\ -1/500 & 0 \end{bmatrix}. \quad (2.52)$$

This results in an output radius of curvature $R_{out} = -74367$ mm and a beam radius $w_{out} = 122$ mm, as expected.

2.9 CST® overview and technique

We will now describe a commercial simulation package used for electromagnetic modelling. Extensive use will be made of this package throughout this thesis, most notably in the analysis of waveguide cavities for SAFARI (chapter reference to be inserted here). Computer Simulation Technology (CST) Studio Suite® [22] is a commercial general purpose electromagnetic simulation package based on the Finite Integration Technique (FIT). Unlike most numerical methods, FIT discretises the integral form of Maxwell's equations rather than the differential form [23].

$$\oint_{\partial A} \vec{E}.\vec{ds} = -\int_{A} \frac{\partial \vec{B}}{\partial t}.d\vec{A}, \quad (2.53a)$$

$$\oint_{\partial A} \vec{H}.\vec{ds} = -\int_{A} \left(\frac{\partial \vec{B}}{\partial t} + \vec{J} \right) .d\vec{A}, \tag{2.53b}$$

$$\oint_{\partial V} \vec{D}.d\vec{A} = -\int_{V} \rho \; \partial V, \tag{2.53c}$$

$$\oint_{\partial V} \vec{B}.d\vec{A} = 0. \tag{2.53d}$$

To solve these equations numerically, we must first define a finite calcula-

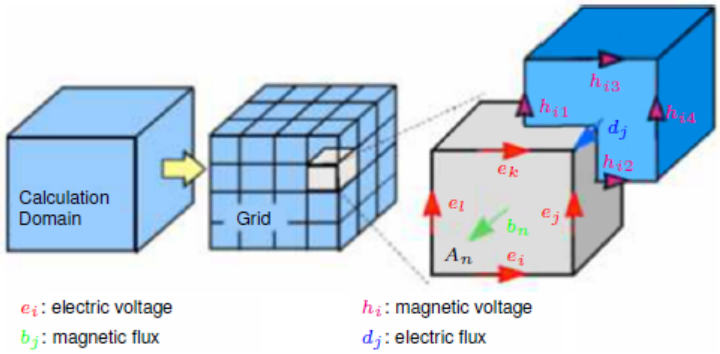

Figure 2.6: Illustration of meshing in CST - source: CST Studio Suite help [23].

tion domain to enclose the considered problem. A mesh is created which divides the domain ino many small grid cells. The primary mesh can then be visualised in CST using the *mesh view*. Internally, a second *dual mesh* is created which is orthogonal to the first one. Then, the spatial discretisation of Maxwell's equations is performed on these two orthogonal grid systems. To illustrate the FIT technique, consider Fig.2.6. Maxwell's equations are formulated for each of the cell facets separately. Now consider equation 2.53a. For a mesh cell, Faraday's law allows the closed integral $\vec{E}.\vec{dS}$ to be written as the sum of four grid voltages $(e_i + e_j - e_k - e_l)$.The time derivative of the magnetice flux on the enclosed cell facet (b_n) represents $\iint d\vec{A}$. Then, we have

$$(e_i + e_j - e_k - e_l) = -\frac{\partial}{\partial t} b_n. \tag{2.54}$$

Repeating this for all the cell facets we obtain the matrix formulation of equation 2.55, which can be expressed using operator notation (equation

2.56).

$$\underbrace{\begin{pmatrix} & . & . & . & & \\ 1 & . & 1 & . & -1 & . & -1 \\ & . & . & . & & \end{pmatrix}}_{\mathbf{C}} \underbrace{\begin{pmatrix} e_i \\ . \\ e_j \\ . \\ e_k \\ . \\ e_l \end{pmatrix}}_{\mathbf{e}} = -\frac{\partial}{\partial t} \underbrace{\begin{pmatrix} . \\ b_n \\ . \end{pmatrix}}_{b} \tag{2.55}$$

$$\mathbf{Ce} = -\frac{\partial}{\partial \mathbf{t}}\mathbf{b} \tag{2.56}$$

Applying this scheme to Ampere's law on the dual grid requires defining a corresponding dual discrete curl operator $\tilde{C}$. Similarly, discretising the remaining divergence equations results in the complete discrete set of *Maxwell's Grid Equations* (MGEs):

$$\mathbf{Ce} = -\frac{\mathbf{d}}{\mathbf{dt}}\mathbf{b}, \tag{2.57a}$$

$$\tilde{\mathbf{C}}\mathbf{h} = \frac{\mathbf{d}}{\mathbf{dt}}\mathbf{d} + \mathbf{j}, \tag{2.57b}$$

$$\tilde{\mathbf{S}}\mathbf{d} = \mathbf{q}, \tag{2.57c}$$

$$\mathbf{Sb} = \mathbf{0}. \tag{2.57d}$$

In the FIT technique, the properties of the continuous gradient, curl and divergence operators are maintained in grid space. In addition to orthogonal hexahedral grids as described here, FIT can also be applied to more general mesh types, such as topologically irregular and tetrahedral grids (Figure2.7).

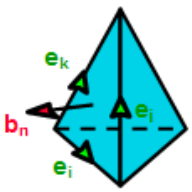

Figure 2.7: CST tetrahedral mesh cell, showing the allocation of the electric voltages and magnetic fluxes. Source: [23].

2.9.1 Solvers within CST

CST Studio Suite has a number of available solvers, however, only three of which are available specifically within the Microwave Studio (MWS) envi-

ronment. These are:

1. Transient Solver
2. Frequency Domain Solver
3. Eigenmode Solver

The transient solver, also called the time domain solver in some newer versions of CST, allows the simulation of a structure's behaviour in a wide frequency range in a single computation run. Therefore, it is an efficient solver for many problems, particularly for structures having large dimensions relative to the wavelengths in question. It is only available to use with the hexaedral mesh type and it is based on the discretised MGEs. Central differences are substituted for the time derivatives:

$$\mathbf{e^{n+1/2}} = \mathbf{e^{n-1/2}} + \mathbf{\Delta t M_\epsilon^{-1}} \left(\mathbf{\tilde{C} M_\mu^{-1} b^n} + \mathbf{j_s^n} \right), \tag{2.58a}$$

$$\mathbf{b^{n+1}} = \mathbf{b^n} - \mathbf{\Delta t C e^{n+1/2}}. \tag{2.58b}$$

Calculation variables are then given by electric voltages and magnetic fluxes. Both types of unknowns are located alternately in time, and the leap-frog updating scheme as shown in Fig.(2) is implemented.

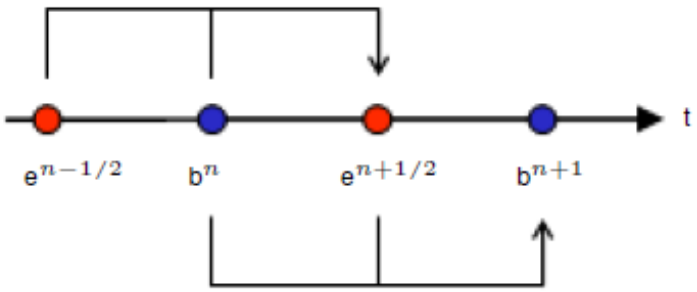

Figure 2.8: Leapfrog scheme as implemented in the transient solver of CST. Scource: [23].

The frequency domain solver can be used with the hexahedral or tetrahedral meshing schemes. It is also equipped with a special fast S-parameter calculation module for resonant, non-lossy structures, where field calculations are not required. The solver is based again on MGEs, here in the time harmonic case ($\partial/\partial t \rightarrow i\omega$).

$$\begin{aligned} \left(\Delta \times \mu^{-1} \Delta \times \left(-\omega^2 \epsilon\right)\right) \mathbf{E} &= -\mathbf{i}\omega\mathbf{J} \\ \Rightarrow \left((\mathbf{\tilde{C} M_{\mu^{-1}} C}) - \omega^2 \mathbf{M_\epsilon} \right) \mathbf{e} &= -\mathbf{i}\omega\mathbf{J} \end{aligned} \tag{2.59}$$

The eigenmode solver allows computation of the structures eigenmodes and corresponding eigenvalues. It is based on the eigenvalue equation for non-driven and loss-free time harmonic problems.

The work to be described in this thesis primarily concerned the use of both the frequency domain solvers. The transient solver is advantageous for the analysis of time varying problems and broadband signals. The frequency domain solver is generally considered only for narrow band problems, as each frequency sample requires a new simulation run. The frequency domain solver is useful for strongly resonant structures (more than the transient solver) due to the long settling times of the time domain signals. CST contains several types of excitation sources, primarily waveguide ports and plane wave sources. The type which we will primarily concern ourselves with is the waveguide port. This kind of port simulates an infinitely long waveguide connected to the structure which the waveguid port is in contact with.

2.10 Experimental arrangement Overview

As the thesis title suggests, a number of experimental results are to be presented. There are a number of scanning systems in use within the department for performing measurements at mm wavelengths, specifically at around 100 GHz, at a wavelength, $\lambda = 3$mm. When measurement techniques are described, a useful distinction can be made between two general types of measurements:

1. Total Power (Intensity) Measurements
2. Amplitude and Phase Measurements

1. Total power measurements are meaurements made with a detector where only the intensity of the detected signal is measured i.e. the square of the field amplitude rather than just the amplitude itself. This can be achieved by simply measuring the detected voltage. Two examples of such detectors are Schottky diodes and Golay cells. Both these detectors are used in alternate setups in the scanning system shown in Fig.2.9, an XYZ scanning system used within the department to perform measurements in mm-wave holography, among other uses.

Figure 2.9: Total power XYZ scanning system within the Experimental Physics Department at NUI Maynooth.

2. Amplitude and phase measurements measure the amplitude of the field itself rather than the square of the amplitude. These are known as vector measurements, and an example of such a system is a *Vector Network Analyser* (VNA). A VNA with an XYZ scanning system also exists within the department, and it is useful for very accurate field scans of quasioptical components, particularly those where the phase front of the field at the scanning plane is of interest.

The technical specifications of the amplitude and phase scanning system will now be discussed here. The test system is built around a Rhode and Schwarz ZVA-24 Vector Network Analyser (VNA). The system is based around a Rohde & Schwarz (R&S) ZVA-24 Vector Network Analyzer which has a base unit frequency range of 10 MHz to 24 GHz. Two ZVA-Z110 converter heads allow stepping up of the operating frequency to the W-Band (75-110 GHz) [24]. The VNA Test Facility is capable of accurate near-field beam pattern measurements for the frequency range 75 GHz to 110 GHz using a 2D planar scanning system with high spatial resolution (order 20 μ m) [25]. The frequency converter heads have WR-10 waveguide ports for direct interfacing with standard W-band components. Each is capable of coherent measurement of transmitted and received signals at its port, allowing full characterisation of a two port device in terms of its scattering matrix. The full dynamic range of measurements depends on the measurement point bandwidth that is used and with careful calibration it is in the 70-90 dB range.

For normal beam pattern measurements one VNA converter unit operates as a transmitter and feeds the Device Under Test (DUT), while the second converter unit (used as a receiver) is mounted on the scanner positioned in front of the DUT. A measurement probe (essentially a truncated WR-10 waveguide) is normally used on the scanning head for high spatial resolution. The achievable dynamic range of the S_{21} measurement with respect to the beam centre is up to 90 dB.

The transmitting VNA head is also placed on an accurate z translation stage to allow different measurement planes to be scanned after a single alignment procedure.

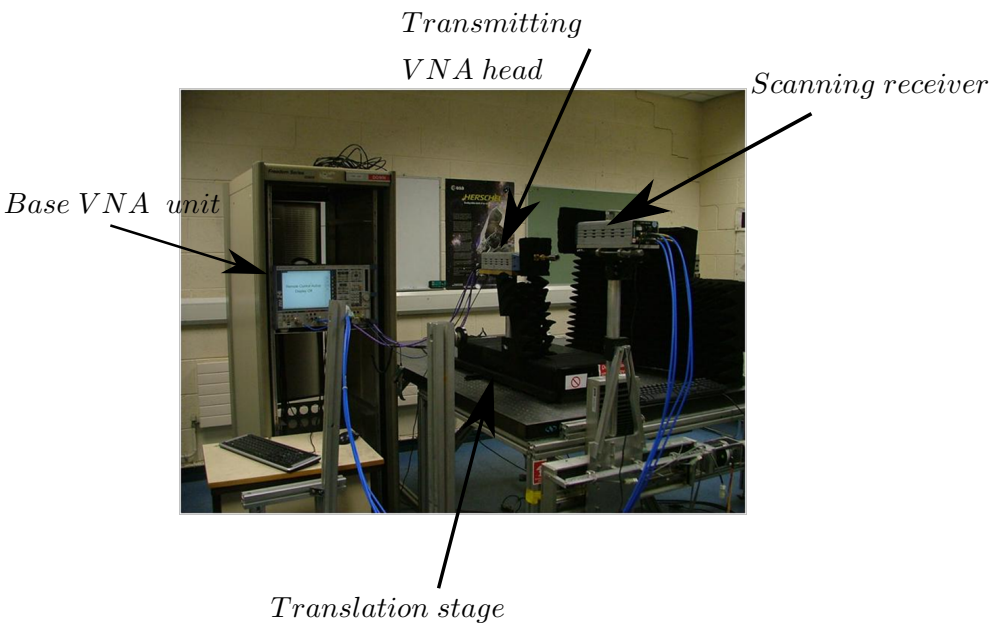

Figure 2.10: Schematic diagram showing VNA test facility.

It is also necessary to precisely calibrate the VNA before a series of measurements. Calibration is performed for each frequency in the 75-110 GHz range in steps of 100 MHz. The calibration is performed using a Rhode & Schwarz calibration kit. The calibration is a standard two-port Through Offset Short Match (TOSM) calibration. The calibration kit used is shown in figure 2.11.

2.11 Scattering Parameters

Further to our discussion of measurement techniques above, it will be instructive to describe in some detail the operation of scattering parameters or

Figure 2.11: Rhode & Schwarz calibration kit for calibration of VNA.

S-parameters in multiple port networks. These will become important later as they will be the measured quantity in measurements performed with the VNA, as well as being the quantity of interest in many CST simulations, and simulations involving multiple reflection systems. We will refine our discussions to two port networks, as this will describe the underlying theory which is extendable to networks of more than two ports, and also as two ports will sufficient for our purposes.

S-parameters are different from some traditional methods of network analysis, such as H-parameters, Y-parameters and Z-parameters, which variously relate total currents and total voltages at each port. S-parameters are instead calculated in terms of waves which are transmitted or reflected when a network is inserted into a transmission line of characteristic impedance, Z_L. S-parameters are relevant in microwave design because they are easier to measure at high frequencies than other two port network parameters. It must be kept in mind that S-parameters represent the *linear* behaviour of the two port network.

Consider a two port system as in Fig. 2.12. In a scattering matrix formulation, we may consider the device under test, i.e. the system which stands between our input and output ports, to be described by a simple 2 x 2 scattering matrix. Then, we have the matrix equation 2.60

$$\begin{bmatrix} b_1 \\ b_2 \end{bmatrix} = \begin{bmatrix} S_{11} & S_{12} \\ S_{21} & S_{22} \end{bmatrix} \begin{bmatrix} a_1 \\ a_2 \end{bmatrix}, \tag{2.60}$$

where each of S_{11}, S_{12}, S_{21} and S_{22} is itself a scattering matrix. The s-parameters themselves are ratios of incident and scattered wave parameters. With reference to Fig.2.12, we may see that S_{11} is then the ratio b_1/a_1, where $a_2 = 0$. S_{11} is just the *input reflection coefficient*, or the fraction of the input

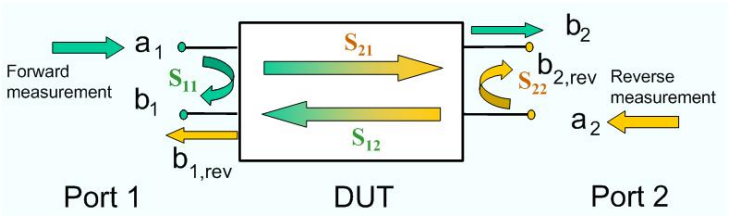

Figure 2.12: Illustration of S-Parameters in a twoport network.

signal which is received again at the output port. Similarly, S_{22} is the *output reflection coefficient*, it is what is reflected back at the output port from itself. S_{21} is the *forward transmission coefficient*, as it is the ratio of the signal which passes through the network from the input port (port 1) to the output port (port 2). Similarly again, S_{12} is the *reverse transmission coefficient*, as it measures the ratio which is measured at port 1 which originated at port 2. In all cases, one may remember which is the relevant S-parameter by the order of the subscript. The first element is the port at which the measurement is made, the second element is the port at which that signal originated. For example, S_{21} is what is measured at port 2, having originated at port 1.

As previously mentioned, s-parameters will be used extensively throughout this thesis, both in terms of where measurements are taken using the VNA, where the port measurements are converted internally to the s-parameters, and also where simulations are made using the correct scattering matrix formulations to obtain output s-parameters. When we characterise the performance of an optical cavity for example we will quote the S_{11} as the measure of the returned power from the incident waveguide.

2.12 Truncation by Quasioptical Elements

We have previously described (equation 2.5) the electric field using a linear sum of Gaussian modes in the form

$$E = \sum_{0}^{n} A_n \Psi_n, \tag{2.61}$$

where Ψ_n is an independently propagating free-space mode of order n and A_n is a mode coefficient. In modelling quasioptical systems, we will often include truncating quasioptical elements, i.e. elements which change the form of the field due to their finite size and real edges. These elements will only have

a finite radius. If we consider the element to be axially symmetric in the simplest case, then we can characterise the output electric field, E_o in terms of the input field, E_i in the form

$$\begin{aligned} E_0 &= E_i(r), \ r \leq a \\ E_0 &= 0, \ r \geq a, \end{aligned} \tag{2.62}$$

where a is the radius of the aperture or stop, and r is the distance off-axis. This is illustrated in figure 2.13, illustrating that radiation striking the areas outside the stop is effectively lost (truncated) from the system. The incident and output fields shall be described as

$$\begin{aligned} E_i &= \sum_0^n A_n \Psi_n(r) \\ E_o &= \sum_0^m B_m \Psi_m(r), \end{aligned} \tag{2.63}$$

where B_m are the set of output mode coefficents. In a similar way to how the input mode coefficients are calculated, the output coefficients are given by [26]

$$B_m = \int_0^a \Psi_m(r) E_o(r) 2\pi r dr. \tag{2.64}$$

Within the aperture the output field is the same as the incident field so we

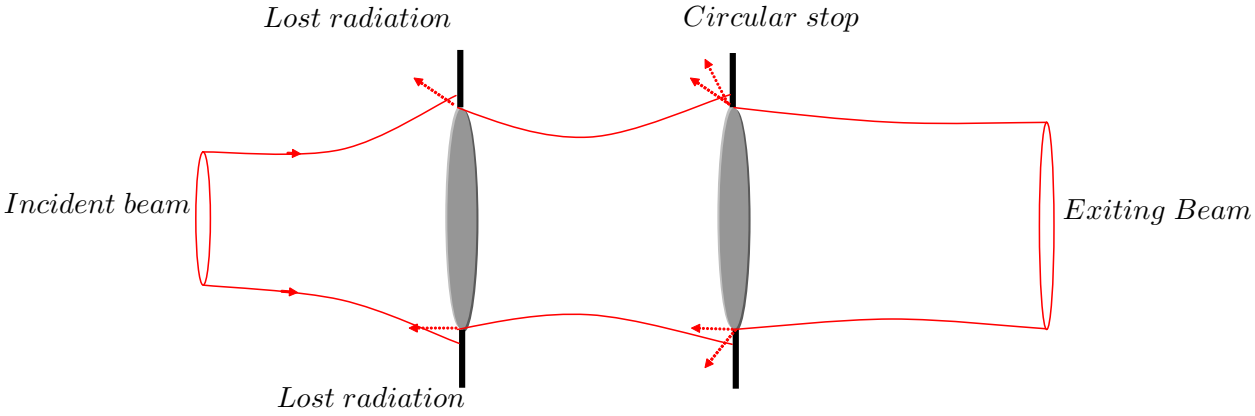

Figure 2.13: Illustration of the truncation in a quasioptical system due to circularly symmetric stops. Source [27].

may write

$$\begin{aligned} B_m &= \int_0^a \Psi_m(r) E_i 2\pi r dr \\ &= \sum_0^n A_n \int_0^a \Psi_m^*(r) \Psi_n(r) 2\pi r dr. \end{aligned} \tag{2.65}$$

We define

$$S_{mn} = \int_0^a \Psi_m^*(r)\Psi_n(r)2\pi r dr, \tag{2.66}$$

and call S_{mn} a *scattering matrix*. This matrix relates the output coefficients to the input coefficients through

$$B_m = \sum_0^n S_{mn}A_n. \tag{2.67}$$

Thus, in our optical modelling including truncating stops, we must calculate the initial mode coefficients A_n as usual, and also calculate the scattering matrix to find the output mode coefficients B_m. If the truncating stop is not axially symmetric, the computations become more complex, but we shall not require consideration of such cases here.

We wish to describe here also the operation of a corrugated horn (horn design with inner corrugations to create a symmetric beam). This horn is often represented by a HE_{11} (hybrid mode) which represents the shape of the beam well. A truncated Bessel beam of order zero is a good representation of the horn aperture shape. Truncated means the beam tapers to zero at the apaerture edge. In our experimental measurements at 100 GHz we will generally use a corrugated horn on the source antenna to produce a field that is approximately 98% Gaussian (e.g. we will use this to illuminate optical devices such as an axicon described in chapter 3). The feedhorn produces a beam which is analytically described by a Bessel function which is truncated by the width of the horn aperture, so that it is a very close approximation to a Gaussian shaped field. We shall take this opportunity to show the fields produced by the horn calculated using GBMA (theory described above).

Figure 2.14(a) shows the linear beam produced at the mouth of the corrugated horn with the appropriate overlap integral between a Laguerre-Gaussian mode set abd an electric field with the shape of a truncated Bessel. It does indeed have a Gaussian-like profile. As we have stated, it is described by a Bessel function, but it is truncated at the horn aperture radius (7.14 mm). Figure 2.14(b) shows the far field amplitude of the corrugated horn. Note the difference in the scales of both graphs. The beam has spread significantly when it has proagated to the far field, and we also note the presence of small sidelobes outside of the main beam due to the truncation of the horn

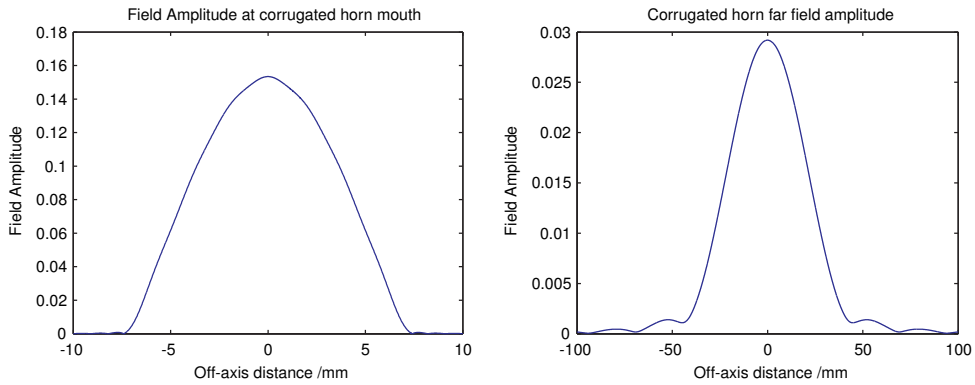

(a) Amplitude profile of beam produced at corrugated horn mouth.

(b) Far field amplitude profile of beam produced by corrugated horn.

Figure 2.14: Ampltiude profiles due to corrugated horn, at horn mouth and in horn far field.

aperture.

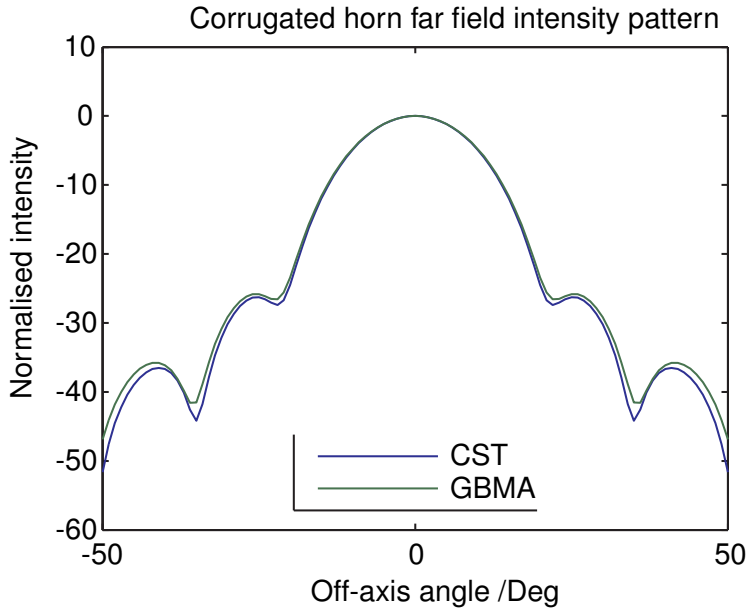

Figure 2.15: Comparison of corrugated horn far field patterns using CST and GBMA.

Figure 2.15 shows the far field pattern of the corrugated horn, produced using CST, and also using GBMA, plotted as a function of angle off-axis. The profiles agree extremely well in the main beam, and even outside of here there is only slight disagreement in the sidelobe structure. The reason for this is that the scalar approximation made in GBMA is only accurate to around 30° off-axis.

We will now illustrate the effects of truncation using a simple optical arrange-

ment. We wish to illustrate the effects of truncation by a circular stop by considering propagation of a field from a corrugated horn. Figure 2.16 shows the setup. Radiation is propagated from a corrugated horn a distance z_1 to a circular stop of radius a. Any radiation outside this radius is truncated, and only the radiation inside the aperture passes through to be recorded at an output plane. The propagation continues a distance z_2 where the amplitude profile is plotted. We will perform this simulation both with the truncating circular stop and without (i.e. propagation in free space) to compare the beam shape.

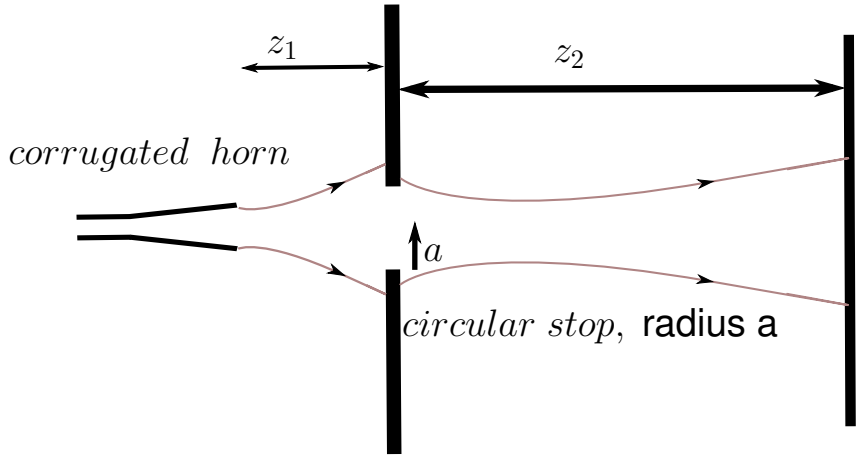

Figure 2.16: Propagation from a corrugated horn, illustrating truncation by a circular stop.

Figure 2.17(a) shows the output power upon propagation of z_1= 80 mm to a truncating stop of radius 25 mm and propagating another distance z_2= 20 mm. Note that the total beam radius is actually about 31 mm, as the beam has propagated a distance in free space after the stop. Figure 2.17(b) shows a logarithmic profile due to the truncating stop compared with no truncating stop, illustrating truncation by the circular stop outside its radius. The edge taper (see section 2.7.1, equation 2.41) due to this truncating stop at a radius of 25 mm from the centre of the beam is -12.05 dB. On a linear scale the ede taper is so low that it is not evident.

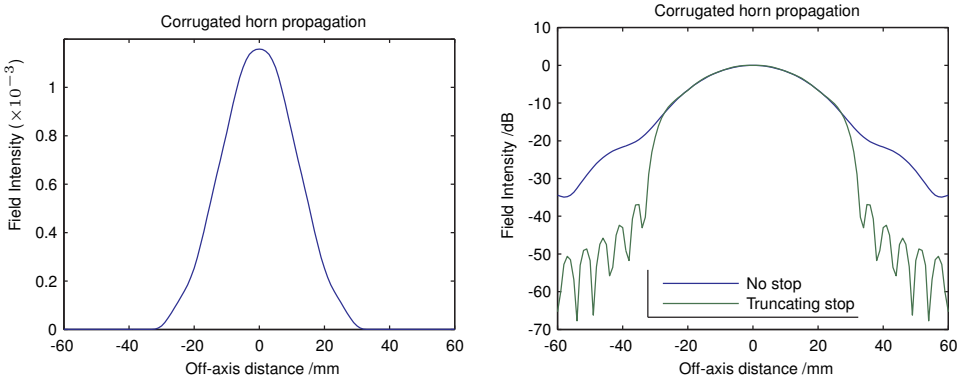

(a) Linear intensity profile of beam produced due to truncating stop of radius 25 mm.

(b) Logarithmic intensity profile of beam produced by propagation in free space with no truncation (blue), compared with the case where a truncating stop is included (green).

Figure 2.17: Intensity profiles after propagation from corrugated horn, with and without truncation by a circular stop, illustrating effective truncation outside the radius of the stop (2.17(b)).

Chapter 3

Axicon and Bessel Beam Analysis

We now wish to discuss the analysis and use of quasioptical components known as *axicons* to produce approximate *Bessel Beams*. Numerous other phase manipulating elements have been investigated. These include Ronchi phase gratings, Fresnel zone plates, and spiral phase plates [28, 29, 30]. Ronchi gratings are often used as beam splitters in interferometry. Fresnel zone plates are diffractive focusing lements composed of radially symmetric rings, alternating between opaque and transparent due to their height. Light diffracts around the opaque zones and constructively interferes at the desired focus. A spiral phase plate has a thickness (in the direction of propagation) which varies around the circumference of the plate. This causes a phase change to an incident mode passing through the plate which introduces a spiral element into its phase front. While these elements are all interesting, the axicon is very interesting and also very simple geometrically, meaning that these can be fabricated relatively quickly without the need for a very sophisticated process.

3.1 Background Theory

An unfortunate property of millimetre-wave radiation is that it suffers from significant diffraction upon propagation. This reduces the on-axis intensity of a beam, as the beam propagates. So-called "Bessel-beams" are cylindrically-symmetric solutions to the scalar wave equation which have the interesting

property of effectively not diffracting as they propagate. For such an ideal beam, the on-axis intensity would remain constant with propagation without any deviation in form. In real experimental situations, an infinite lateral extent of the optical element would be required to produce such a beam. Clearly then, this is an idealisation, however in reality "diffraction-limited" solutions are possible, which have a Bessel-like feature. This was first suggested by Durnin in 1987 [31].

The described solution to the wave equation described above is written as

$$E(r, z, t) = J_0(k_r r)exp(i(k_z z - wt)), \tag{3.1}$$

where J_0 is the zero-order Bessel function of the first kind, and k_r and k_z are the axial and radial wavenumbers respectively. It is much more difficult to produce "limited-diffraction" beams at submillimetre wavelengths than at optical wavelengths. The reason for this is that at optical wavelengths, optical components may be thousands of wavelengths in diameter due to the relatively short wavelengths, and as such the problem of the finite lateral extent is not as problematic. Durnin et al [32] used a lens with an annular aperture to produce a Bessel Beam. Methods using an *axicon* have been shown to be more efficient [27].

An axicon is a cyclindrically symmetric lens which has one conical surface. It can be used to transform an incident Gaussian type beam into a Bessel beam. This is of particular importance as most designed horn antennas have a Gaussian type radiation pattern.

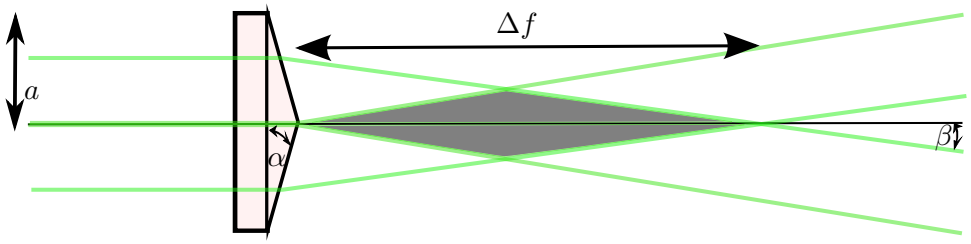

Figure 3.1: Schematic diagram showing axicon and its parameters.

Figure 3.1 shows the simple geometry of an axicon. The prism angle of the axicon is α, and its radius is a. The angle of deviation of the axicon is denoted by β. Due to its particular geometry, incoming radiation from different directions experiences refraction towards the propagation axis, and here the beam effectively interferes or *overlaps*. This occurs over the shaded region Δf.

The region over which the output field is still useful and contains limited diffraction is called the *limited-diffraction depth of focus*, Δf, and is given by the relation

$$\Delta f = a/tan\beta, \tag{3.2}$$

where $sin(\beta + \alpha) = n_r sin\alpha$. The central peak of a Bessel beam may be approximated by a simple Gaussian beam of radius w. However, the depth of focus of a Bessel beam is much larger than the usual confocal distance which would apply for a simple Gaussian. The essential difference between the two beams is that the Bessel beam contains low-level diffraction rings. This non-diffractive property of the output beam is potentially interesting as the beam remains collimated much longer than normal radiation patterns. This could be an interesting alternative to traditional optics at millimetre wavelengths in the focusing of beams for particular applications (e.g. mirrors or lenses). An axicon of finite diameter can produce an on-axis peak with very little diffraction over a range Δf. Illuminating the axicon with plane wave illumination can cause significant diffraction effects, however [33]. The beam needs to be apodised, and using Gaussian illumination is a way of achieving this in practice. The highly tapered beams produced by a metallic waveguide or scalar horn in fact have the form of the lowest order Bessel function $|J_0(k_r r)|^2$ [14] and are therefore compatible for the illumination of such diffractive elements. The fields produced by a corrugated horn and the far field of such a horn are described in section 2.12. Below we shall discuss an optical analysis of such devices and compare predictions from simulations to experimentally measured output beams measured at 100 GHz.

3.2 GBMA application to Axicon

Gaussian Beam Mode Analysis (GBMA) can be used to efficiently analyse the diffraction effects associated with the beam. Due to the cylindrical symmetry involved, the Laguerre- Gaussian modes are the most appropriate to use here. Higher order Laguerre- Gaussian modes have amplitude profiles similar to those of Bessel beams, and also remain collimated over longer distances than the confocal distance indicated for a simple Gaussian. We require a number of high order LG modes which accurately describe the behaviour of Bessel beams produced with axicon elements. The use of the correct mode set when analysing such beams is of critical importance. For high order LG modes,

the central peak contains only a small fraction of the total power, and one must consider the effective radius, as well as the diffraction rings produced with an axicon. Figure 3.2 shows such a Bessel form, with its narrow central peak and multiple diffraction rings extending off-axis.

GBMA is an efficient way to model these beams, as considerable insight can be found into the performance of axicons of finite diameter. The axicon will be considered to be a thin phase-transforming screen of finite diameter. A suitable phase term to be added to account for the phase transformation contribution of this thin lens is described below.

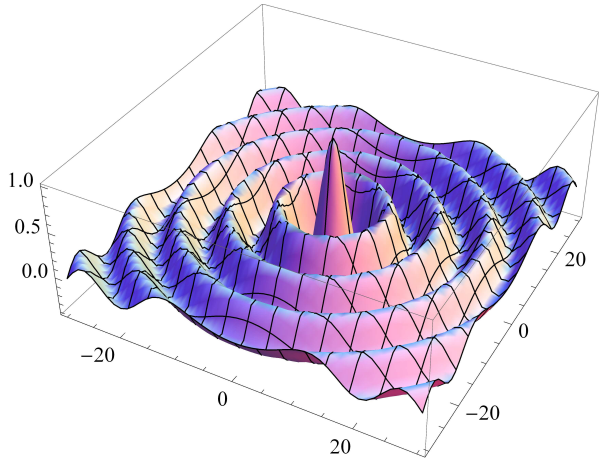

Figure 3.2: 3D plot showing the form of Bessel function, with narrow central peak and diffraction rings. The amplitude is normalised, and the x- and y- coordinates are given in mm off-axis.

Using the Fresnel diffraction approach, and assuming that the axicon introduces a conical phase transformation of the form $\delta(r) \propto r$, the amplitude $E(X,Y,Z)$ at a point (X,Y,Z) on a plane $z = Z$ is given by the Fresnel diffraction integral

$$E(X,Y,Z) \propto \int_0^{2\pi} \int_0^{a} \frac{exp(-jk_0\rho)}{\rho} r dr d\phi, \tag{3.3}$$

where $\rho = \sqrt{(X - rcos\phi)^2 + (Y - rsin\phi)^2 + Z^2}$ and (r,ϕ) are the polar coordinates on the axicon plane. The conical shape of the axicon introduces a variation in the optical path length across the incident beam with a linear variation from the centre. The cone thickness at a radius r is given by $t(r) = (a - r)tan\alpha$, giving the phase transformation at that distance from the centre as

$$\delta(r) = \delta_0 + k_0(n_r - 1)(a - r)tan\alpha, \tag{3.4}$$

where δ_0 is the phase slipage through the centre of the axicon and n_r is the refractive index of the material. High Density Polyethylene (HDPE) is a suitable material for submillimetre axicons, having $n_r = 1.52$. To achieve sufficient detail about the evolution of this beam would require evaluation of this diffraction integral for a large number of points and this is computationally intensive, as well as becoming unstable as $z \to 0$. The modal approach does not have such shortcomings and is relatively unintensive computationally when compared to the Fresnel diffraction integral method.

We require only the symmetric Laguerre-Gaussian modes of degree zero and, using the mode set described in chapter 2 (equation 2.37), we have the beam mode $\Psi_n(r,z)$ described as

$$\Psi_n(r,z) = \frac{1}{w(z)}\sqrt{\frac{2}{\pi}} L_n\left(\frac{2r^2}{w(z)^2}\right) exp(-\frac{r^2}{w(z)^2}) exp\left(-jk\left(\frac{r^2}{2R(z)}\right)\right) \times exp(-jkz) exp(j(2n+1))\Delta\phi_{00}(z), \tag{3.5}$$

where the terms are as described in detail in chapter 2. The mode coefficients are calculated, if the field scalar E is known, using the overlap integral

$$A_n = \iint \Psi_n*(r, z_0, w(z_0), R(z_0))E(r, z_0) r dr d\phi. \tag{3.6}$$

Ideally, we require a single high-order Laguerre-Gaussian mode $\Psi_n(r,z,w,R)$ that is a reasonable approximation to the axicon beam. When an axicon is placed in a proagating beam, the output beam is related to the input beam through $E_{out}(r,\phi) = E_{in}(r,\phi)exp(j\delta(r))$, with $\delta(r)$ as described above. In this approach the axicon is treated as a thin lens, and diffraction effects within the thickness of the axicon are ignored. The mode coefficients including the phase contribution due to the axicon are then calculated using

$$A_n = \int_0^{r=a} \int_0^{\phi=2\pi} \Psi_n^* \{E_{in}(r,\phi) exp(j(k_r r - \delta_0^{'})\} r dr d\phi, \tag{3.7}$$

where $k_r = (n_r - 1)tan\alpha$ and $\delta_0 = k_0(n_r - 1)atan\alpha$. We can firstly assume that the input field is a simple Gaussian as corrugated horns produce Gaussian beams with $\approx 98\%$ efficiency. The field at a plane beyond the axicon can be calculated once the mode coefficients are known, using the standard summation $\sum A_m \Psi_m(r,z,w(z),R(z))$. The beam effectively diffracts as the relative phase shifts accumulate between different modes, where we have also described the extra phase transformation inflicted by the axicon element.

We shall now follow a similar approach to that taken in [27] in choosing a suitable value of w_0, the beam width parameter, which will produce a mode set which most efficiently describes a propagating Bessel beam. The choice of the best mode set ensures that the axicon is described most accurately and efficiently with the minimum amount of computation required. We begin by computing the normalised power contained in each mode, for various values of w_0 (note: w_0 in mm). We are considering an axicon with a prism angle, $\alpha = 20°$, radius, a, of 30 mm and refractive index, n, of 1.52. Figure 3.3 shows the result of calculating the power contained in each of the first 20 modes, for various values of w_0.

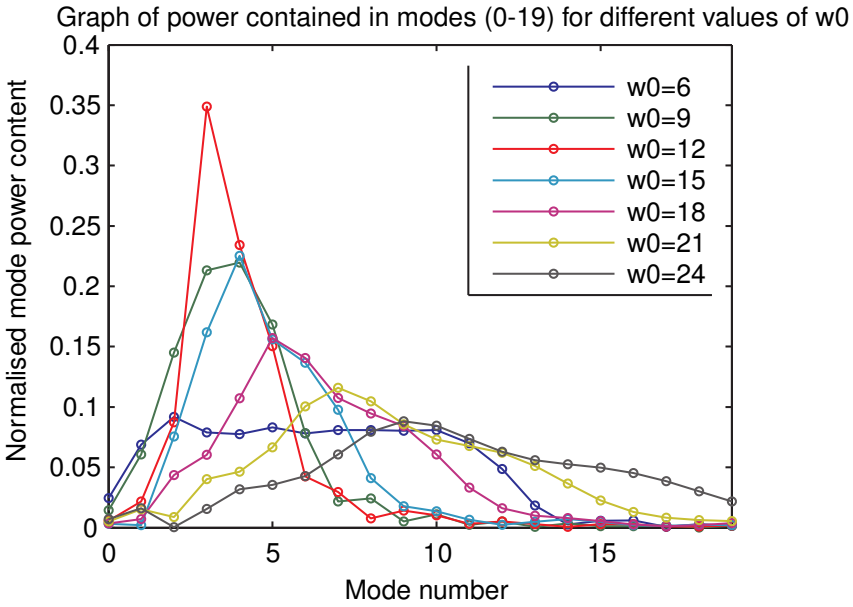

Figure 3.3: Power content of each of first 20 modes for different values of w_0.

We have stated that we wish the Bessel beam modal decomposition to be composed of a small number of Laguerre-Gaussian modes to achieve the most natural decomposition and ensure efficient computation. From figure 3.3 then, we see that the case where w_0=12 mm is most likely our best choice. This has a small number of modes from around $n = 2$ to $n = 5$ which clearly give a reasonable representation of the beam by themselves. Figure 3.4 shows how close to the total field we get by using just the modes from $n = 2 - 5$ in the modal summation. In this case we come very close to approximating the equivalent Bessel field.

It could also be argued that w_0=9 mm is fit for our purpose, as it contains a few neighbouring modes with high power content. However, a larger number of modes would be required to accurately reresent the beam in this case. For

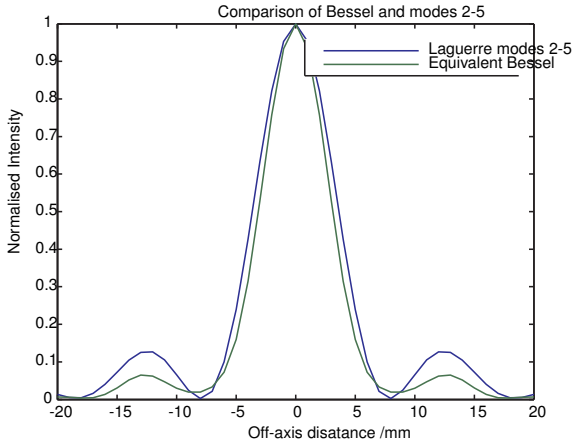

Figure 3.4: Comparison of modal summation of modes $2-5$ with equivalent total Bessel field.

Table 3.1: Higher order mode coefficients of a Bessel beam for w_0=12 mm and $\alpha = 20°$.

Mode number	Abs. value $\lvert A_m \rvert$	Power Content in each mode $\lvert A_m \rvert^2$
0	0.0764	0.0058
1	0.1470	0.0216
2	0.2956	0.0874
3	0.5905	0.3487
4	0.4839	0.2341
5	0.3879	0.1505
6	0.2063	0.0426
7	0.1716	0.0294
8	0.0883	0.0078
9	0.1188	0.0141
10	0.1010	0.0101
11	0.0572	0.0033
12	0.0714	0.0051
13	0.0539	0.0029
14	0.0281	0.0008
15	0.0539	0.0029
16	0.0552	0.0031
17	0.0312	0.0010
18	0.0291	0.0008
19	0.0416	0.0017

example, taking the case where w_0=12 mm, then the modes of order 2,3,4 & 5 together account for around 83% of the total power in the beam, whereas the same 4 modes in the w_0=9 mm case give us around 75% of the total beam power. Table 3.1 shows the coefficents and power content of each of the first 20 modes for w_0=12 mm. The most efficient mode set for describing the beam should also have a confocal distance approximately equal to the

limited diffraction depth of focus calculated for the Bessel beam, i.e.

$$\frac{\pi w_0^2}{\lambda} \approx \frac{a}{tan\beta}$$
$$\text{or } w_0 \approx \sqrt{\frac{\lambda a}{\pi tan\beta}}. \tag{3.8}$$

For the case in question, this gives us $w_0 \approx 11.97$ mm, i.e. in using a mode set where w_0=12 mm, we should obtain the most efficient Bessel beam.

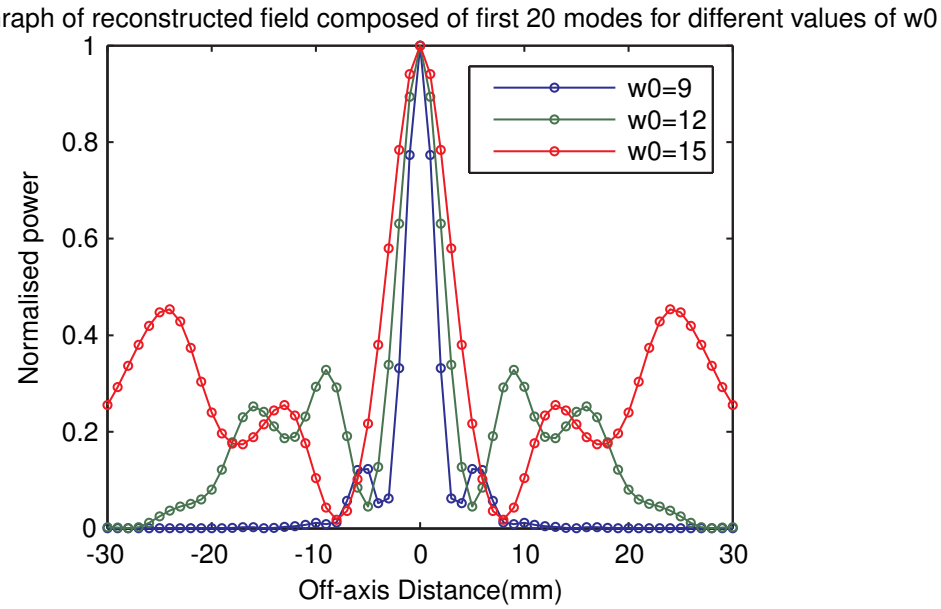

Figure 3.5: 1D cut through the Bessel output field created by summing the first 20 modes for three interesting values of w_0.

Figure 3.5 shows the field produced using the standard modal summations for three separate values of w_0; the two previously discussed (9 mm, 12 mm) and also 15 mm, as it also showed significant power in its modes in figure 3.3. We see that the beam shape for our chosen case of w_0=12 mm has a slightly wider beam than that for w_0=9 mm. For w_0=12 mm, mode numbers $3, 4, 5$ contain significant power. These modes are most physically similar to the Bessel beam. However, we also have a more Bessel-like profile, as desired, and the beam is narrower than that for w_0=15 mm.

We now wish to show plots of the axicon amplitude and phase for some representative propagation distances, to illustrate how collimated it remains compared to a normal horn antenna radiation pattern (using a Gaussian beam approximation). An application of equation 3.2, along with the relation $sin(\beta + \alpha) = n_r sin\alpha$, allows calculation of a value for the depth of focus for this axicon of $\approx$ 150 mm. Firstly, we will examine the variation of

on-axis intensity of the formed beam as a function of propagation distance, z, after having been phase-transformed by the axicon described above where a=30 mm, $n_r = 1.52$ (HDPE), and we examine radiation at a frequency of 100 GHz. Figure 3.6 shows this simulated variation over a propagation distance of 350 mm. To calculate this graph the modes and mode coefficients are summed at each z value and the on-axis intensity is recorded at each output distance from the axicon. The total power in the beam is normalised to unity, therefore the on-axis values quoted here are much less than unity. We notice that the beam reaches its maximum on axis value at a propagation distance of around 100 mm, and it contains significant power in the region from aproximately 75-125 mm. We had previously calculated the depth of focus of this axicon to be about 150 mm. The depth of focus is the region over which the field contains limited diffraction, and from the figure we can see that by the 150 mm point the power decreases significantly. Indeed, by 150 mm, it has decreased significantly, and therefore 150 mm can be reasonably thought of as the edge of the depth of focus.

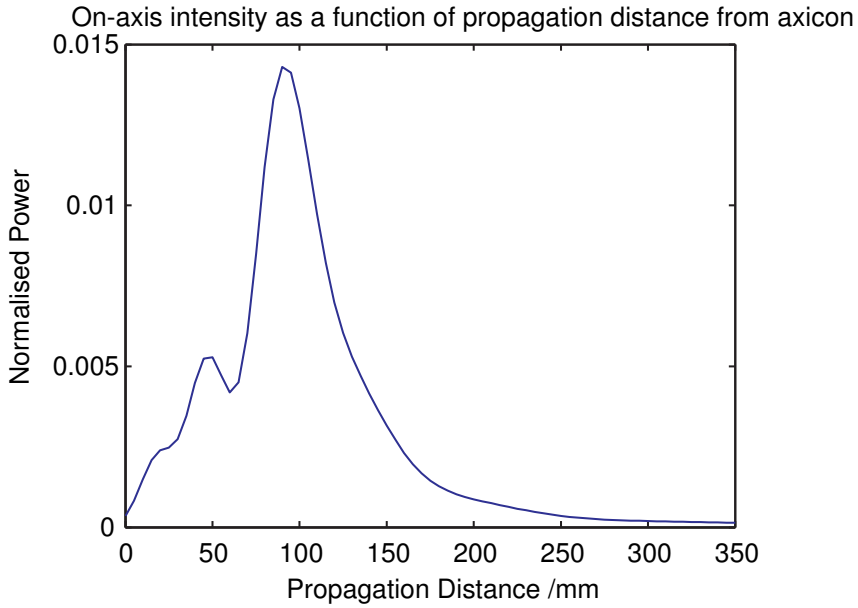

Figure 3.6: Variation of on-axis intensity of beam as a function of propagation distance $(0 - 350mm)$ after transformation by the axicon

With reference to figure 3.6 then, we may sensibly choose representative distances at which to plot the field and phase profiles of the beam. We choose 0 mm, where the beam has had the phase transformation due to the axicon, but has not propagated any distance, 75 mm, where the beam should be taking a Bessel characteristic shape, 100 mm, where the beam should contain aproximately its maximum power, and 200 mm, where the

beam should have dissipated, have a more spread out profile and contain little power on-axis, as it is beyond the expected collimation distance of the described axicon.

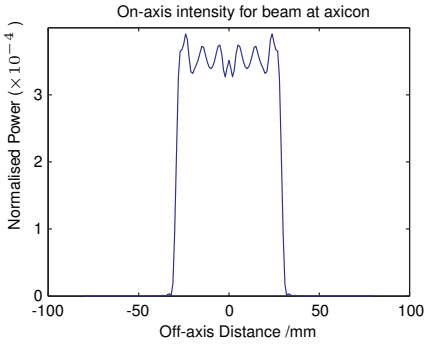

(a) Intensity profile of beam at axicon.

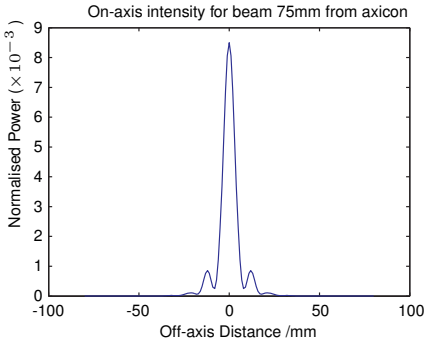

(b) Intensity profile of beam after propagating 75 mm from axicon.

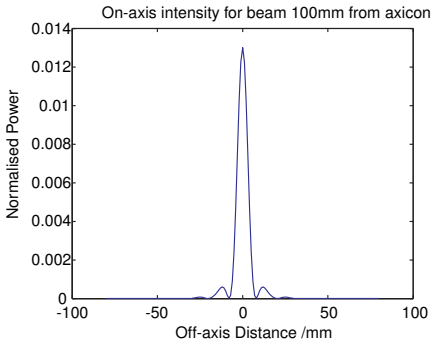

(c) Intensity profile of beam after propagating 100 mm from axicon.

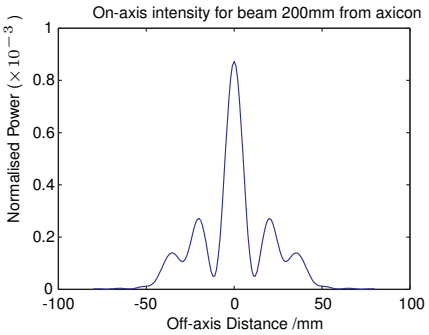

(d) Intensity profile of beam after propagating 200 mm from axicon.

Figure 3.7: Intensity profiles of beam after varying propagation distances for an axicon of radius 30 mm and prism angle 20°.

Figures 3.7 and 3.8 show the intensity and phase profiles, respectively, for each of these cases. We see that, before the beam has propagated, the intensity profile is very broad, and in fact resembles a top-hat profile of a circular aperture. The beam has effectively been truncated by a circular aperture with the same radius as the axicon (30 mm), and so it is not surprising to observe this form of profile. Here we assume that the axicon is illuminated with a large incident Gaussian beam, fully filling its aperture. We also notice that the phase profile rapidly oscillates from $-\pi$ to π, showing the presence of the phase transformation introduced by the axicon, at the locations of the nulls in the intensity. We observe that when the beam has reached a distance of 75 mm, the beam has become very focused, and contains some low order diffraction rings. Also, the corresponding phase profile has be-

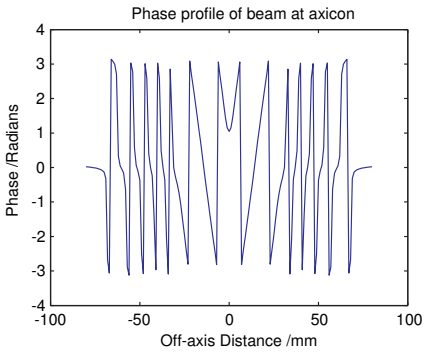

(a) Phase profile of beam at axicon.

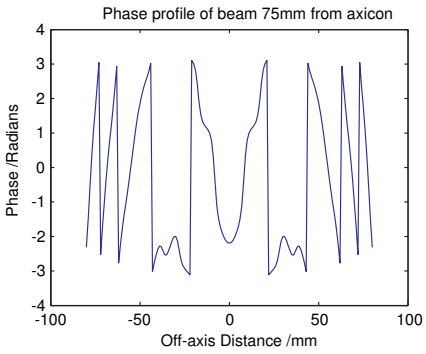

(b) Phase profile of beam after propagating 75 mm from axicon.

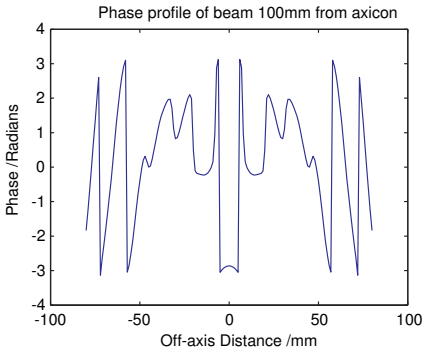

(c) Phase profile of beam after propagating 100 mm from axicon.

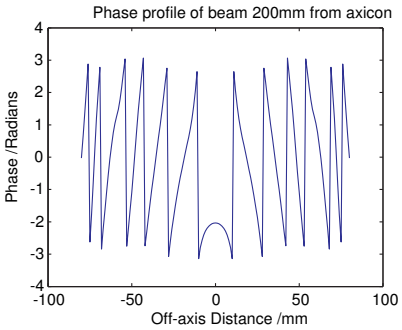

(d) Phase profile of beam after propagating 200 mm from axicon.

Figure 3.8: Phase profiles of beam after varying propagation distances for an axicon of radius 30 mm and prism angle 20°.

come more spread out, with the 2π discontinuities becoming less frequent. Upon propagation to a distance of 100 mm, the intensity profile is similar to that for 75 mm, with a higher level of power contained in the main beam. After propagating a distance of 200 mm, the power in the main beam has decreased significantly, as expected, and a relatively higher amount of power has spread into the diffraction rings. The interesting aspect here is that over a large distance of 150 mm we can have a collimated beam. Figure 3.9 illustrates this by comparing the intensity and phase profiles for a beam which has been transformed by an axicon and propagated 75 mm, and an equivalent Gaussian modal summation beam having propagated the same distance in free space. We notice that the non-axicon beam is much wider, and has its power spread out over a much wider area, and therefore is extremely small in height when plotted along with the equivalent beam transformed by the axicon. Also, in the phase profiles we notice the difference particularly in the main beam, where for the axicon beam the main beam is sharply defined, for

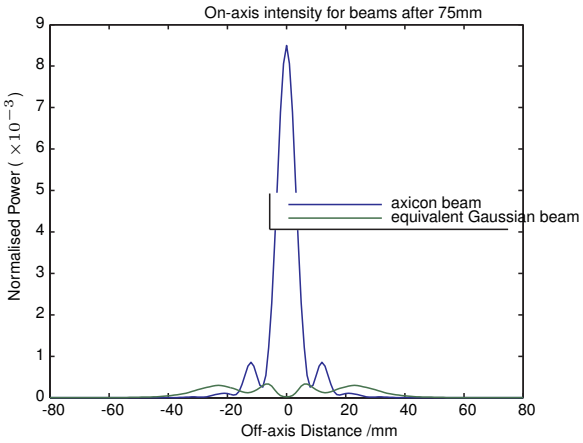

(a) Intensity profile of beam after propagation of 75 mm.

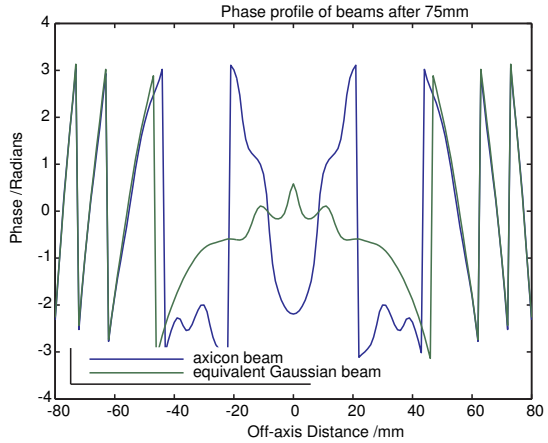

(b) Phase profile of beam after propagation of 75 mm.

Figure 3.9: Intensity and phase profiles for axicon beam and equivalent Gaussian beam summation after propagation of 75 mm.

the Gaussian beam this is not the case.

Figure 3.10 shows the on-axis intensity profiles for propagation over a range of 350 mm for a variety of axicon prism profile angles ($10° - 50°$). We have already examined the 20° case (figure 3.6). We notice a significant difference in the on-axis intensity profile for the axicon with prism angle 10° (figure 3.10(a)) and that with angle 20° (figure 3.6). In the 10° case, there is a much lower overall power than in the 20° case, and it reaches it maximum intensity after a longer propagation distance. However, it does contain a larger overlap region, - the region over which it produces a limited diffraction beam- although its maximum intensity is lower than that for the 20° axicon. As was discussed previously when it was shown in figure 3.6, the 20° axicon

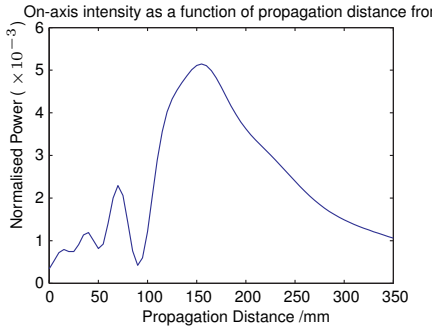

(a) On-axis Intensity for axicon with prism angle 10°.

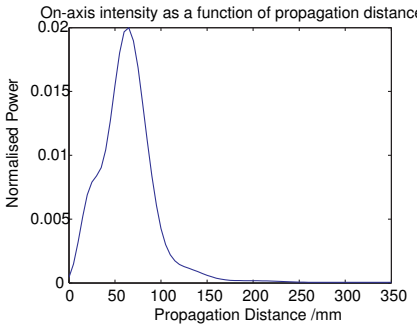

(b) On-axis Intensity for axicon with prism angle 30°.

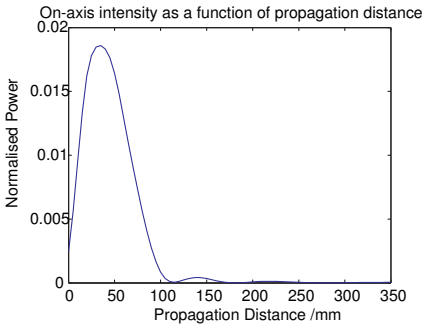

(c) On-axis Intensity for axicon with prism angle 40°.

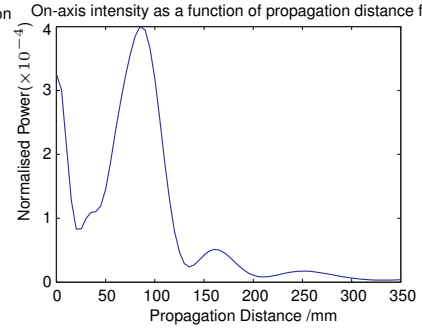

(d) On-axis Intensity for axicon with prism angle 50°.

Figure 3.10: On-axis Intensity profiles of beam after propagation from 0 to 350mm for an axicon of radius 30mm and prism angle varying from 10° to 50°.

creates a beam with a relatively high on-axis intensity in its overlap region, and this occurs over a relatively short overlap region. This is due to the rofile of the parent axicon and illustrates that different axicon designs could be used for different potential applications. For a prism angle of 30°, the maximum intensity value is higher than for the 20° case, and the overlap region occurs after a shorter propagation distance. For a prism angle of 40°, a similar situation occurs as for 30°, although the overlap rehion occurs and has completely ended after a propagation distance of less than 100 mm. Finally, for an axicon with prism angle of 50°, the on-axis intensity decreases significantly, in accordance with equation 3.2.

Of the axicons shown in figure 3.10 then, the 10° axicon would be of the most use if wishing to increase the on-axis intensity of a beam propagating around 150-200 mm. If a higher intensity beam is required over a much shorter distance, 40° or even 30° axicxon may be of use, whereas a middle ground is achieved with an axicon having a prism angle of 20°, where a relatively high power is achieved over an intermediate distance. In summary then, there is

a trade off when designing an axicon. If limited diffraction is required over a relatively large distance, the trade off will be diminished intensity in the main beam. Higher intensity levels may be achieved, but these will be over a shorter distance. The particular problem in question will generally dictate which parameter is of most importance, when used in a particular optical arragement.

3.3 Analysis of Existing Axicon

We now wish to proceed by analysing an existing axicon within the department which had been made for past measurements. We will perform GBM simulations as we have previously done for a 20° axicon. Experimental measurements will also be performed, using the departmental VNA facility, which allows phase and amplitude measurements.

The existing axicon has a radius, a, of 30 mm, refractive index, n, of 1.52, i.e. it is made from High-density polyethylene (HDPE). The only difference between this axicon and the one previously analysed in section 3.2 is that the axicon we analysed in section 3.2 had a prism angle of 20°, whereas this axicon has a prism angle of 10°. Clearly, the effects that these two axicons would have on an incoming beam would be significantly different. We shall now perform GBM analysis on the 10° axicon (figure 3.11).

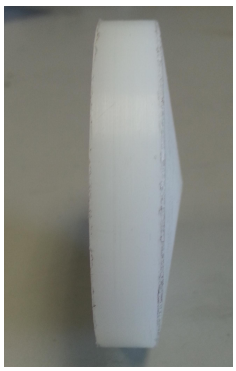

Figure 3.11: 10° axicon.

In section 3.2, we determined the best choice of beam width parameter for producing a Bessel-like beam with an axicon, using a small number of Laguerre-Gaussian modes. In an experimental setup, however, we will be

using the VNA and probe scanner system. The input signal from the VNA head will be launched in free space to the axicon from a corrugated cyclindrical feedhorn. The analytical expression to describe the width of a beam from a corrugated horn is given by [14]:

$$w = 0.644a, \tag{3.9}$$

where a is the radius of the horn aperture. For a corrugated cyclindrical horn having an aperture radius of 7.14 mm, then, the input beam width parameter will be 4.60 mm. We shall then use the form of the corrugated horn field in our simulations. This approach is effectively the same as the approach in section 3.2, except that the input beam modes are transformed by the appropriate Bessel form for the corrugated horn ($|J_0(k_r r)|^2$).

We now wish to describe the measurement process using the VNA/scanner system for the axicon. Figure 3.13 shows the measurement setup. Head 1 of the VNA acts as the detector. It has an X-Y scanning axis and is fixed in the Z-plane. Head 2 in this case acts as the source. It is often fixed during a scan but it may be mounted on a translation stage which allows motion during a scan in one plane, and in this way it is possible to perform an X-Y-Z scan (figure 2.10). The scan is performed over the selected X- and Y- planes. Then, the translation stage moves and the X-Y scan is performed again, this time with a new output position. We shall wish to perform a series of X-Y field scans at various z-values, i.e. various propagation distances after the axicon. We have designed a mounting bracket which attaches to a special axicon holder containing the axicon (figure 3.12). The bracket attaches to the movable translation stage. In this way, the axicon can be kept a fixed distance from the source, but the distance after the axicon to the detector probe can be varied, to characterise the output beam of the axicon. The lens holder is metallic but is shielded with microwave absorbing material to avoid unwanted standing wave reflections due to this additional metallic surface. A corrugated conical horn is used on the source head, and a scanning probe is used on the detector head. The distance from the corrugated horn opening to the axicon is denoted as z_2, and the distance from the point of the axicon to the scanning probe tip is denoted z_1.

A series of measurements were performed on the 10° axicon. All measurements were carried out in the w-band ($75 - 110$ GHz). The axicon was held in the specially designed lens holder which moves in the z-direction as the

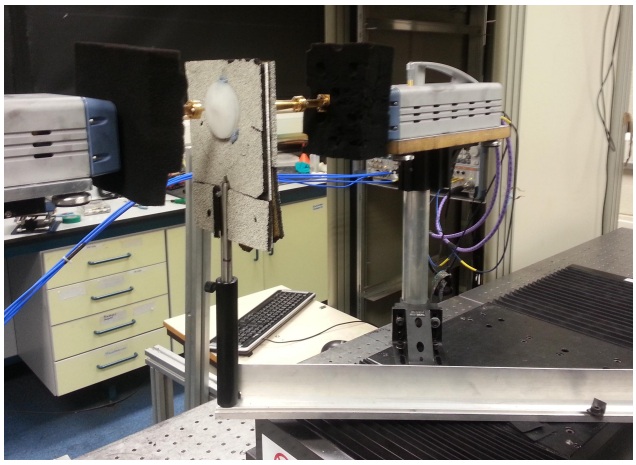

Figure 3.12: Axicon mounting bracket.

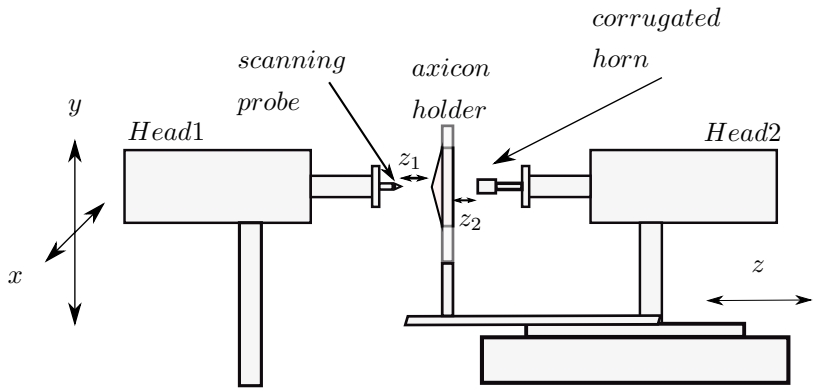

Figure 3.13: Schematic of axicon measurement setup showing axicon holder

source head moves, so that the distance between the source and axicon remains constant as the distance between axicon and detector is varied. With reference to figure 3.13, the distance from the horn to the axicon (z_2) is set as 16 mm, and the distance from the axicon tip to the detector (z_1) is 23 mm. These values were mainly chosen due to the constraints of the system, and the desire to have at least a small propagation distance (z_1), even for the initial scan. The scan was performed for 5 unique z-values; the initial setup, and also for increased z-distances in steps of 30 mm up to 150 mm. Note that, including the original z_1 value, the second scan will represent a z_1 value not of 30 mm but of 30 + 23= 53 mm. Scans were also performed for each of these distances without the axicon in place for comparison, i.e. the field produced by the horn alone without the axicon is observed. Figure 3.14 shows the result of the first of these scans, that where z_1=23 mm and z_2=16 mm. All results have been normalised for the purposes of comparison. We find that we achieve quite good agreement between the measured profile for the axicon field and the simulated shape. The two fields do vary slightly outside

of the main beam. The difference between the axicon field and the field due to the horn is significant, illustrating the extremely collimated axcion profile within the overlap region of the axicon.

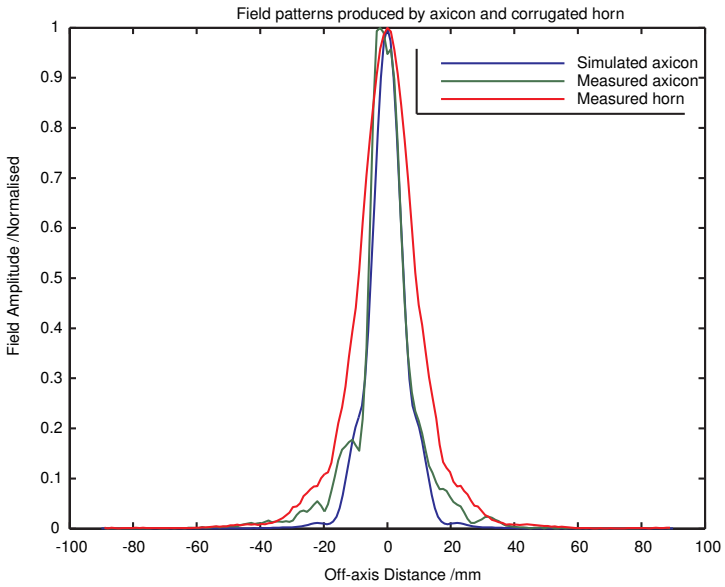

Figure 3.14: Comparison of field amplitudes in one dimensional cut for axicon (measured and simulated) and corrugated horn alone, for initial propagation distance of 23 mm after the axicon, performed at 100 GHz.

Figure 3.16 shows the equivalent results for different propagation distances after the axicon (at 100 GHz). Note that in each case, the total distance travelled by the beam is 16 mm from the horn to the axicon, then it must travel through the axicon, which has a depth of 13 mm, and subsequently the stated propagation distance. Therefore, for the measurements with a corrugated horn alone, the beam has travelled 29 mm in free space *plus* the stated propagation distance. We find that the measured and simulated field profiles for the axicon generally agree relatively well, particularly in the main beam. There is generally slight disagreement between the two when we examine slightly outside the main beam. We also notice that the measured axicon beam is slightly asymmetric and tends to show slightly better agreement in the positive x-direction. The fact that there is an asymmetry may suggest non-perfect alignment of the measurement arrangement. We also find that the corrugated horn profile is much wider than the profiles produced by the axicon, as expected, illustrating its collimating effect. Figure 3.15 shows the phase profiles for both the measured axicon and corrugated horn, for the initial propagation distance of 23 mm after the axicon. We have only included these two, as it is so difficult to see the profiles in the plot with three plots

together. We see that the phase profiles do not agree. This shows that the axicon does indeed introduce a phase transformation. We notice this particularly on-axis and within a short distance off-axis, where the two beams are significantly out of phase. This should not be surprising; the axicon has a radius of 30 mm, and within this distance the beam is significantly transformed due to the axicon.

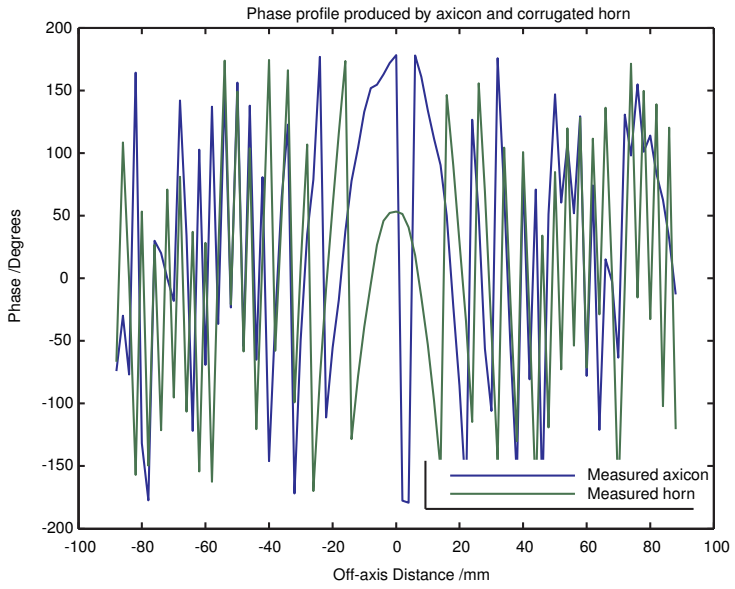

Figure 3.15: Comparison of phase profiles in one dimensional cut for axicon (measured) and corrugated horn alone, for initial propagation distance of 23 mm after the axicon.

3.4 Design and Manufacture of Axicon for particular Application

We shall now discuss the design and manufacture of an axicon for a particular application, and the considerations that need to be made, as well as the parameters that may be varied. An axicon could be designed for a number of potential applications where a focused beam is required and diffraction is highly undesirable. This could have potential applications in projects involving space telescopes, for example. The Experimental Physics department has involvement in many such projects, including the proposed SAFARI project, which will be discussed in much more detail in chapter 6. Although axicons are not planned to be used in that project, they may have potential future applications in other projects not yet envisaged.

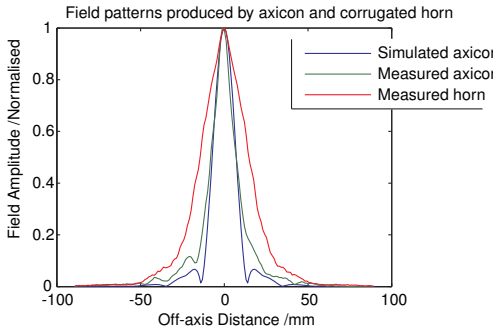

(a) Propagation distance of 53 mm after axicon.

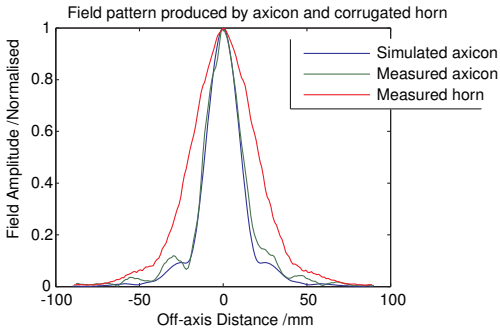

(b) Propagation distance of 83 mm after axicon.

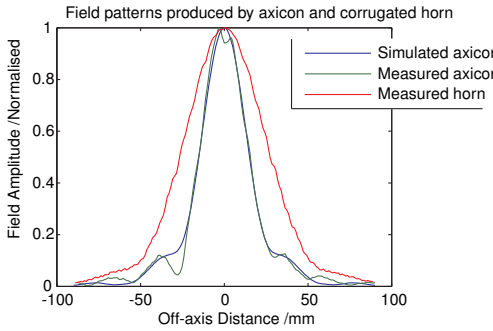

(c) Propagation distance of 113 mm after axicon.

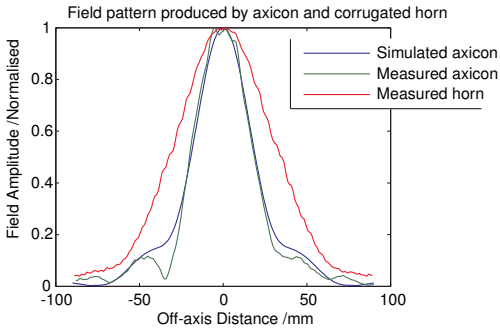

(d) Propagation distance of 143 mm after axicon.

Figure 3.16: Comparison of field amplitudes for axicon (measured and simulated) and corrugated horn alone, for initial propagation distances of 53 mm, 83 mm, 113 mm and 143 mm after the axicon.

We have previously examined different axicon geometries (altering the prism angle), and noted the effect that this parameter has on the on-axis intensity of the resultant beam over a large propagation distance. This is a useful exercise in designing an axicon for particular applications. For example, one may require an axicon which produces a beam that peaks in intensity very rapidly but falls off very rapidly, if collimation is only required over a short distance. Alternatively, an axicon which produces a relatively steady but lower intensity field output over a longer distance may be necessary if the free space collimation distance is relatively large, and it is required that a beam does not spread out over this distance. We have already peformed measurements on an axicon having prism angle 10°, and also radius a=30 mm, and index of refraction $n = 1.52$ (HDPE). We wish to design and produce another axicon, and perform simulations and measurements on it also. With reference to figures 3.6 and 3.10, we see that an axicon having prism angle of either 20° or 30° produces a beam that peaks in intensity at around 100 mm of propagation after passing through the axicon. This would be interesting

for direct comparison with the 10° axicon. We shall again use an axicon of radius 30 mm and a refractive index of 1.52, so that we are only varying one parameter. Also, a radius of 30 mm should certainly be sufficient for our purposes, as it will always be placed very close to a corrugated horn having a radius of 7.14 mm, and therefore the beam is much smaller than the axicon.

An axicon having the following parameters was produced within the departmental workshop: a=30 mm, $\alpha = 20°$, $n = 1.52$. A measurement campaign

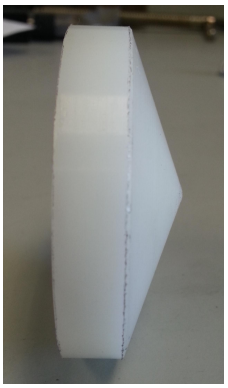

Figure 3.17: 20° axicon.

was performed for this axicon, in a similar manner to those described in 3.3. In this case, the measurement is set up in much the same way as the previous measurements for the 10° axicon. The distance from the input corrugated horn to the axicon is 16 mm, and the distance from the axicon to the waveguide probe detector is initially 52 mm. The z distance is then varied in steps of 30 mm, up to an axicon-probe distance of 142 mm. Figure 3.18 shows the results of one of these measurement scans, the initial separation of 52 mm from axicon-detector probe. We observe from the results similar levels of agreement as those found for the 10° axicon and shown in 3.14 and figure 3.16. We do still observe a similar asymmetry in the measured axicon amplitude profile. We also notice that the horn amplitude profile is again much wider than those for the axicon.

Figure 3.19 shows the results of the other three measurement scans involving the 20° axicon.

Figure 3.20 shows a comparison for the 10° and 20° axicons where propagation has occured over a distance of the initial setup plus 60 mm, i.e. the beam for both axicons has propagated over the same distance as in 3.19(b).

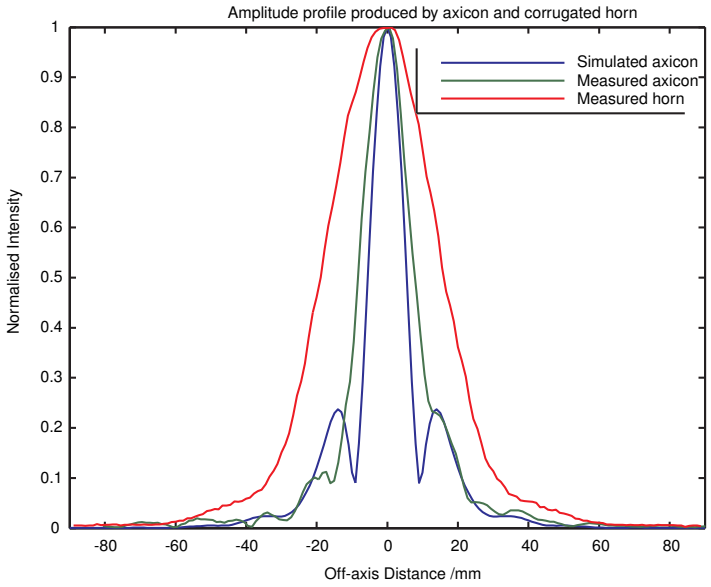

Figure 3.18: Comparison of amplitude profiles in one dimensional cut for axicon (measured & simulated) and corrugated horn alone, for initial propagation distance of 52 mm after the axicon.

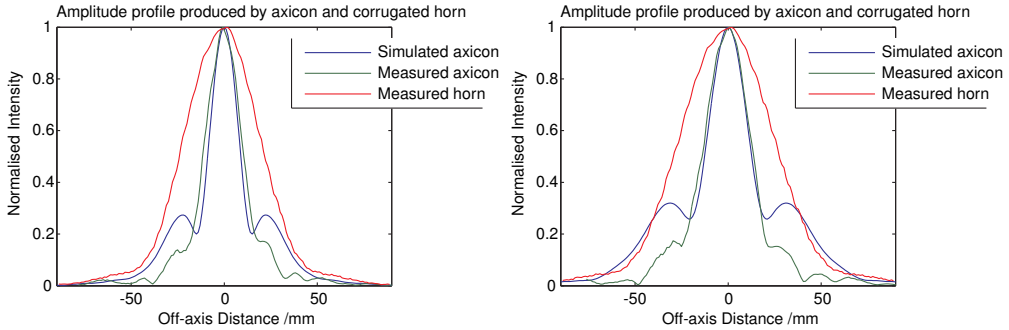

(a) Propagation distance of 82 mm after axicon.

(b) Propagation distance of 112 mm after axicon.

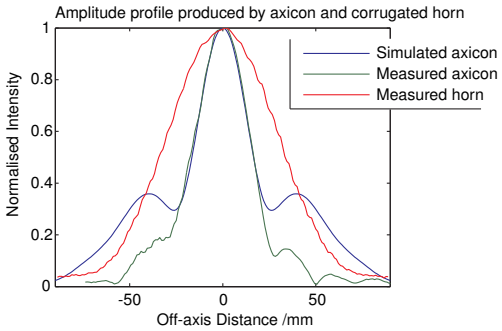

(c) Propagation distance of 142 mm after axicon.

Figure 3.19: Comparison of field amplitudes for axicon (measured and simulated) and corrugated horn alone, for initial propagation distances of 82 mm, 112 mm, and 142 mm after the axicon.

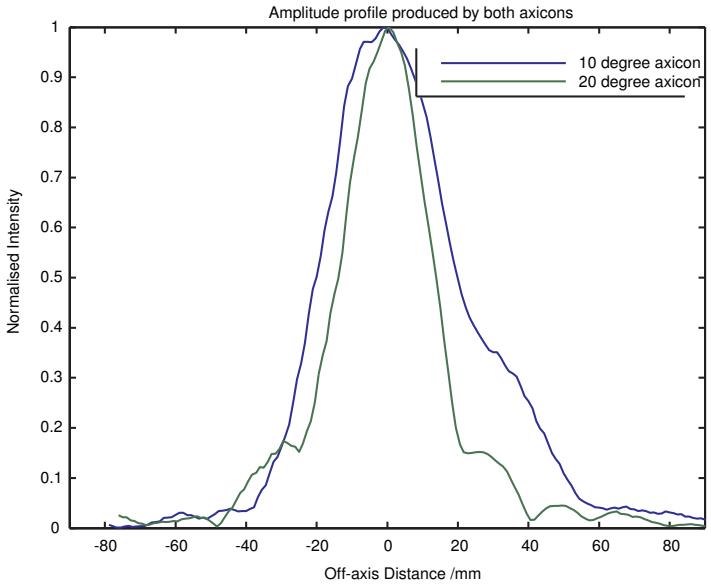

Figure 3.20: Comparison of amplitude profiles in one dimensional cut for both axicons after a propagation distance of 60 mm after the axicon.

We have shown measurement results performed at 100 GHz, as our axicon has been designed for use at 100 GHz. As an exercise, we wish to show results from other frequencies. The VNA van perform measurements in the band from 75-110 GHz, and so we will show a result from 75 GHz and 110 GHz and plot alongside our 100 GHz result from above. The example we will choose is the field due the 20° axicon at a propagation distance of 52 mm after the axicon, i.e. the same distance as in figure 3.18.

Figure 3.21 shows these 3 profiles plotted together. We have not normalised the beams as had been done previously, so that the comparison is clearer. We find that the profile with the highest power on-axis is at 100 GHz. This is to be expected, as the axicon was designed with the intention of it being used mainly at 100 GHz. This is also the narrowest beam, although it is very close to the profile at 110 GHz in shape and in on-axis power content, with the 75 GHz profile containing less power on-axis as well as being mre spread out. Neither is it surprising that there are closer resemblances between the two profiles at 100 GHz and 110 GHz than at 75 GHz and 100 GHz, as they are much closer in frequency to one another.

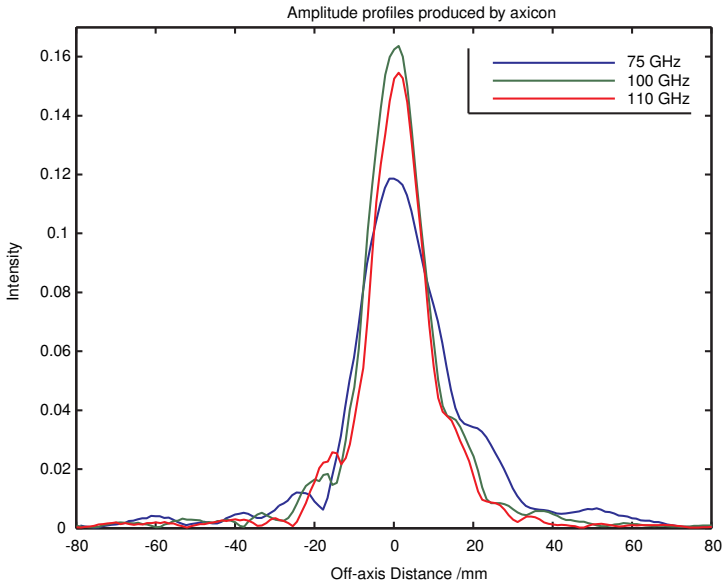

Figure 3.21: Comparison of amplitude profiles in one dimensional cut for 20° axicon after a propagation distance of 52 mm after the axicon, at frequencies of 75 GHz, 100 GHz and 110 GHz.

3.5 Gaussian Beam Coupling

An important quantity to consider when dealing with the propagation of millimetre-wave radiation, especially in a measurement system is the *coupling efficiency*, i.e. for perfect coupling, this would have a value of 1. This describes how well the radiation propagating from a source couples to receiver, and it is expressed as a fraction. It is obtained by multiplying the input field by the field which would be present at the detector, and dividing by an appropriate normalisation factor [14]. For example, assume we have a field produced by an axicon and propagated a certain distance, and this field is described by E_{axi}, and we wish to measure this field at a corrugated horn attached to a detector, and the field produced by the horn is E_{horn}. Then, the coupling efficiency, c, is given by

$$c = \frac{E_{axi} \cdot E^*_{horn}}{\sqrt{Abs(E_{axi})^2} \cdot \sqrt{Abs(E_{horn})^2}}, \tag{3.10}$$

where the product is performed over every individual value of the two fields. As an example, for a beam which has propagated 50 mm from an 10° axicon, we obtain a coupling fraction of only 0.29, or 29%, to a corrugated horn. This is clearly very low, and we would like to improve this. This is compared with a horn to horn propagation of the same distance without an axicon present,

where we obtain a coupling of 0.56, or 56%. The axicon introduces a very specific phase profile to the beam, with many zero crossings associated with the annular rings, and it is likely this fact which causes the beam to be unable to couple well back to a corrugated horn. Naively, one might expect to be able to undo this effect to an extent, by introducing a phase directly *opposite* to that due to the axicon. This can be simply done in the GBMA, by simply adding a negative sign in the phase. It is not clear however how this may be done in an experimental arrangement. An identical axicon simply facing in the opposite direction may be too much of a simplification. In any case, we attempt this using GBMA.

In an ideal model with no propagation between source and detector we can manipulate the phase front analytically to simulate its effect on coupling. When we model an axicon using GBMA, we insert the appropriate phase term describing the axicon (equation 3.4). By simply applying this phase term, and not propagating the beam any distance, the beam (which originates at the horn) now has a coupling efficiency of only 88%. Remember that the beam has not propagated any distance and so should couple to itself with 100% efficiency, but due to this phase term being introduced, it no longer couples as well to a corrugated horn. As the beam would propagate, it diverges to some extent, and couple even less efficiently, as we saw in our example above (29% coupling), as is always the case with the propagation of millimetre-wave radiation. The interesting point to note here, howerver, is that this reduction in coupling efficiency is due to the *axicon alone*. If we now introduce the opposite phase term to our beam at the corrugated horn which has not propagated but has been transformed by the first axicon, we find that it now has a coupling efficiency of 99.8%. We see that what is required then is a phase term opposite to the axicon to reverse the phase transformation and achieve higher coupling back to a horn.
Again, it is not clear whether the opposing phase term in reality corresponds to an axicon turned 180° around, or if it involves a more complicated profile. We were not able to further investigate this due to time constraints.

Chapter 4

Kinetic Inductance Detectors

4.1 Introduction

We shall introduce here a class of superconducting detector known as Kinetic Inductance Detectors (KIDs). These devices operate at cryogenic temperatures, typically below 1K. They are being developed for high-sensitivity astronomical detection for frequencies ranging from the far-infrared to X-rays.

At NUI Maynooth we are interested in the optical efficency of these detectors and seeking techniques to analyse their optical quality in terms of absorbing incident radiation. In KID devices an absorber (usually a cryogenically cooled, thin metallic superconducting layer) is coupled to the device.
At Maynooth then the challenge of modelling these devices optically was initially investigated. Illumination of these devices can be considered as plane wave illumination as a first order approximation. Then, once a structure is illuminated with plane wave illumination at a certain frequency we can analyse what fraction of this radiation is absorbed (effectively detected) and therefore characterise its optical behaviour. As a first attempt to model KID devices the commercial package CST (section 2.9) would be used.

The challenge presented then is how to launch plane wave radiation in CST and have the ability to measure the fraction of the incident power that is absorbed. Within the research group a waveguide port was normally applied to analyse waveguide structures. The KID device is not a waveguide and so

the standard techniques could not be used.
The author has investigated the possibility of using plane wave illumination within the CST environment and used the classical optics example of diffraction at a circular aperture to verify the illumination technique in CST. Various techniques may be used in CST to produce plane wave illumination, including standard plane wave source, empty waveguide port using 2 modes, and these will be described in section 4.4.

Unfortunately the full analysis of the optical characterisation was not carried out but the analysis presented here is the initial validation of CST and the use of plane wave sources.

4.2 Background/History

A KID consists of a high-quality superconducting resonant circuit electromagnetically coupled to a transmission line. The conduction electrons in a superconductor are condensed into charge-carrying Cooper pairs, when the temperature, T, is much less than the critical temperature, T_C. Photons incident on a strip of superconducting material break Cooper pairs and create excess quasiparticles. The kinetic inductance of the superconducting strip is inversely proportional to the density of Cooper pairs, and thus the kinetic inductance increases upon photon absorption. This inductance is combined with a capacitor to form a microwave resonator whose resonant frequency changes with the absorption of photons.

The KID was first described in [34], which will be described below.

4.2.1 Initial Proposal by Day et al

The detector concept is based on microwave measurement of the complex impedance of a thin superconducting film. The results presented include single X-ray photon detection with a high signal-to-noise ratio, and measurement of the detector noise. A superconductor has zero resistance to d.c. electrical current. This supercurrent is carried by pairs of electrons (Cooper pairs). The Cooper pairs are bound together by the electron-phonon interaction with binding energy $2\ \Delta \approx 3.5 k_B T_C$, where T_C is the supercon-

ducting transition temperature. However, superconductors have a non-zero impedance for a.c. currents. An electric field applied near the surface of the superconductor causes the Cooper pairs to accelerate, allowing the storage of energy as kinetic energy. This energy may be extracted by reversing the electric field, as the supercurrent is non-dissipative. Energy may also be stored in the magnetic field inside the superconductor, which penetrates only over a short distance, $\lambda \approx 50nm$, from the surface. Overall, the effect is such that the superconductor has a surface inductance $L_S = \mu_0$, due to the reactive energy flow between the superconductor and the electromagnetic field. The total surface impedance is given by $Z_S = R_S + i\omega L_S$. R_S is the surface resistance, which describes a.c. losses at angular frequency ω caused by the small amount of electrons that are not in Cooper pairs, called quasiparticles. For temperatures much lower than T_C, $R_S \ll \omega L_S$, and it is the inductive factor that plays the most important part.

4.3 KID device analysis

Photons having sufficient energy, i.e. $h\nu > 2\Delta$ can break apart one or more Cooper pairs (see figure 4.1(a)). The absorption of a high-energy photon creates $N_{qp} \approx \eta h\nu/\Delta$ quasiparticles. The excess quasiparticles subsequently recombine into Cooper pairs on timescales $\tau \approx 10^{-3} - 10^{-6}$ s . During this time, the quasiparticles can diffuse over a distance $l = \sqrt{D\tau_{qp}}$, where D is the diffusion constant of the material. The detectors make use of the dependence of the surface impedance Z_s on quasiparticle density. Very sensitive measurements may be made using a resonant circuit (figure 4.1(b)). This schematic illustration shows the resonant circuit as a parallel LC circuit which is capacitively coupled to a through line. Changes in R_s and L_s affect both the frequency at which the resonance occurs, and its width (figure 4.2(a) and 4.2(b)). The fractional surface impedance change should be proportional to the fraction of Cooper pairs that are broken.

The device discussed in [34] is a a quarter-wavelength transmission line resonator, which is the transmission line equivalent of the lumped element resonator of figure 4.1(b). A Coplanar Waveguide (CPW) through line is used effectively to couple the incoming signal ad to detect the resonance frequency shift. This also makes use of s quarter-wavelength resonator section, as is visible at B in figure 4.3.

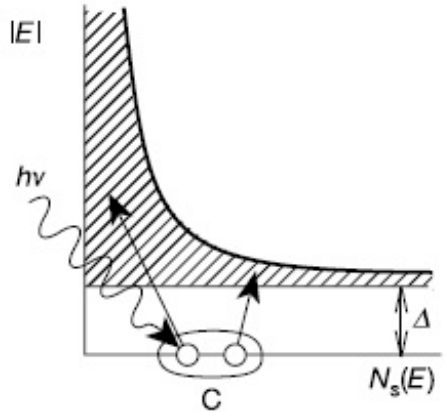

(a) Photons with sufficient energy breaking Cooper pairs in a superconducting film.

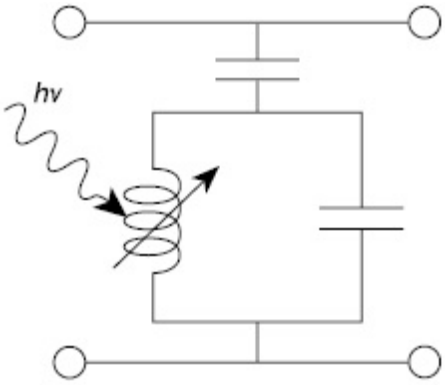

(b) Resonant circuit. The increase in quasiparticle density increases the (mainly inductive) surface impedance. Therefore, the total inductance is increased, while the effect of the surface resistance is to add a series resistance, making the inductor slightly lossy.

Figure 4.1: Power and phase profiles for equivalent circuit.

One of the more interesting applications of KIDs for our purposes here is their potential use in sub-mm astronomy. It is readily possible to multiplex a large number of these devices to create a focal plane array [35]. This is demonstrated in figure 4.4, where an image of Jupiter was recorded.

In many proposed cases, it has been suggested that lens antennas would be appropriate for effectively coupling incoming radiation to the detector plane, to improve the quality and focus of the incoming beam [36, 37]. Lens antennas exist within the department, and as well as their simplicity of manufacture, much use has been made of lens antennas previously within the department [38].

We wish to use some of the tools at our disposal in attempting to model these types of devices. As incoming radiation from an astronomical source will have a plane wave-like phase front, it is this type of radiation that we will need to model as incident on the detectors. While we may not be able to model the complex circuits themselves and replicate superconducting behaviour, we can begin by examining plane wave illumination in CST. A subsequent step may be to add optics to enhance the signal from the field from the sky, before it reaches the main detector optics. We shall begin then by examining plane wave illumination in CST.

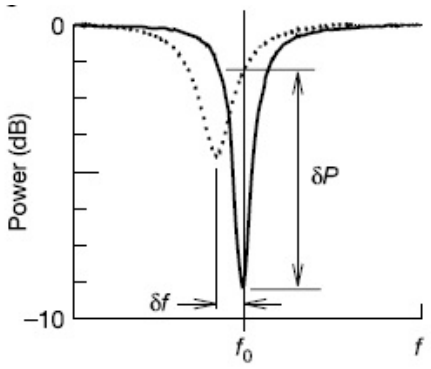

(a) Transmission dip as the LC circuit loads the through line.

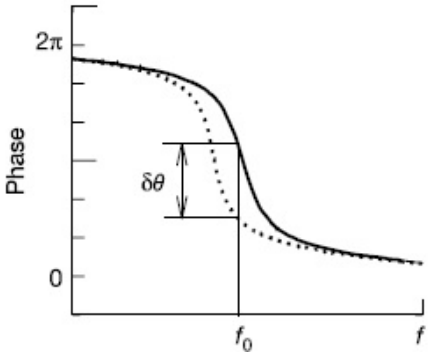

(b) Phase of signal transmitted through the circuit.

Figure 4.2: Power and phase profiles for equivalent circuit.

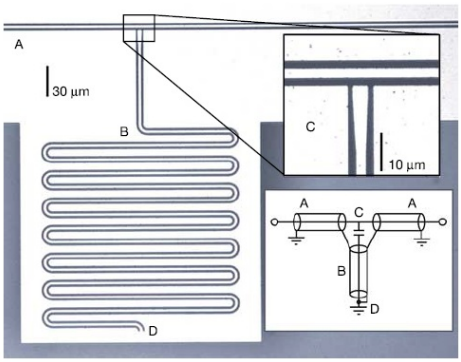

Figure 4.3: Microscope image of device used, also showing the equivalent circuit.

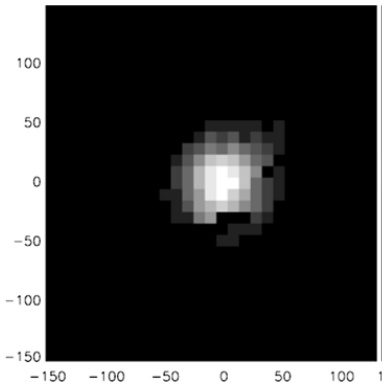

Figure 4.4: 15-minute raster scan of Jupiter obtained at 240 GHz using KID camera at Caltech Submillimeter Observatory. Source: [35]

4.4 CST Analysis of Plane Wave Source

The principles of operation and theory behind the solvers of CST Microwave Studio have previously been described in section 2.9. Now, we will illustrate the use of CST using some simple examples of how an electromagnetic beam is launched, having certain defined characteristics.

It is often useful to perform simulations involving plane wave illumination. Radiation incident on an astronomical instrument, for instance, is likely to be of plane wave form, as it has travelled a large distance from its source to the measurement plane. Thus we may often wish to use this as a starting point in our models, and it will be useful here to understand plane wave illumination in CST. We will use the well known example of diffraction from a circular aperture to verify this function in CST.

Figure 4.5 shows a sheet of *Perfect Electric Conductor* (PEC) material. PEC materials are those that exhibit inifinite electric conductivity, and therefore are not lossy. PEC materials are useful in modelling conducting materials, as they can be simulated much faster than real, lossy materials having finite conductivity. We may compare the results for the far field pattern of

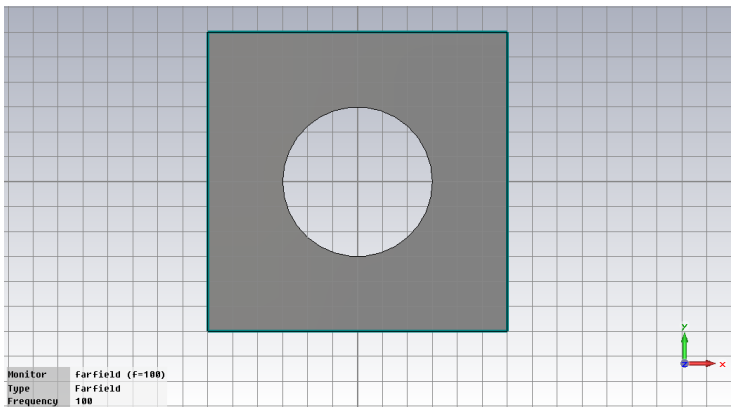

Figure 4.5: PEC sheet with circular aperture shown in the CST design environment.

a circular aperture in a metallic sheet using various methods in CST, and compare these to well known results such as the Fresnel diffraction integrals. The radius of the aperture is 9 mm and the wavelength is 3 mm.

The first method that we will use is the standard plane wave illumination in CST. This defines a plane wave having electric field vector as defined by

the user in each of the X, Y and Z planes, as well as the propagation normal defined by the user as desired. Figure 4.8 shows the far field result from CST with plane wave illumination, compared with an equivalent model created using GBMA. We find that there is very close agreement in the main beam

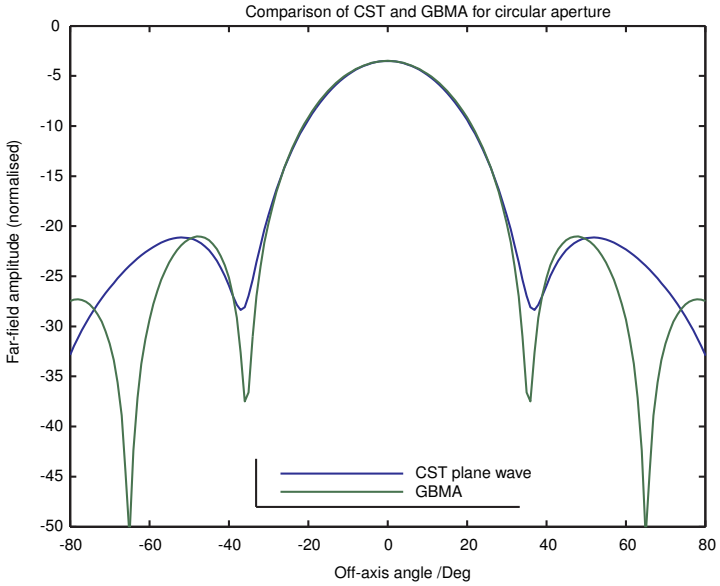

Figure 4.6: Comparison of CST plane wave source with GBMA results for far field due to a circular aperture.

and the two beams agree relatively well out to almost 40° from the axis. We also observe close agreement in the first sidelobes. We have previously discussed the validity of the scalar approximation after a large angle off-axis (section 2.12).

The second method we use for comparison in CST is using waveguide ports. These simulate the input from a metallic waveguide for a selcted number of modes (figure 4.7).

Selecting the first two modes produces two identical modes, but with differing linear polarisations (horizontal and vertical), representing a plane wave with a certain polarisation orientation.

Indeed, from figure 4.8, which includes the far field result due to using the waveguide port, the result agrees very well with the CST plane wave results.

As a final comparison, we use the classic Fresnel diffraction integral result for diffraction at a circular aperture and compare this with out CST results, i.e. an Airy diffraction pattern at the farfield of a circular aperture.

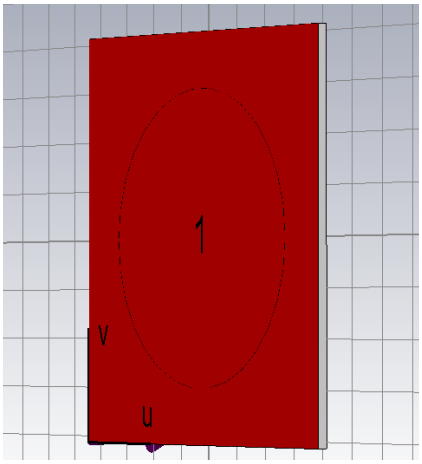

Figure 4.7: PEC sheet with circular aperture shown in the CST design environment, illuminated by a waveguide port.

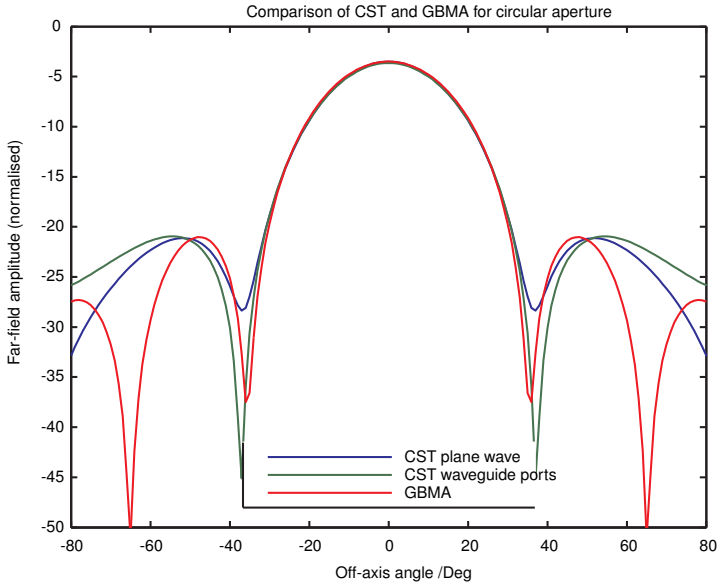

Figure 4.8: Comparison of CST plane wave source and waveguide ports with GBMA results for far field due to a circular aperture.

Figure 4.9 shows this comparison. We see that perfect agreement is found between the diffraction integral and the waveguide port result. The plane wave result and diffraction integral agree well in the main beam.

We have investigated and verified two different methods of modelling plane wave illumination in CST, in order to better understand the process in order to perform more detailed calculations into the optical efficiencies of KID devices. While these will not be performed here, the continuation of this work would involve modelling a more detailed system, with some optics, for example using a lens antenna illuminated with plane wave illumination in

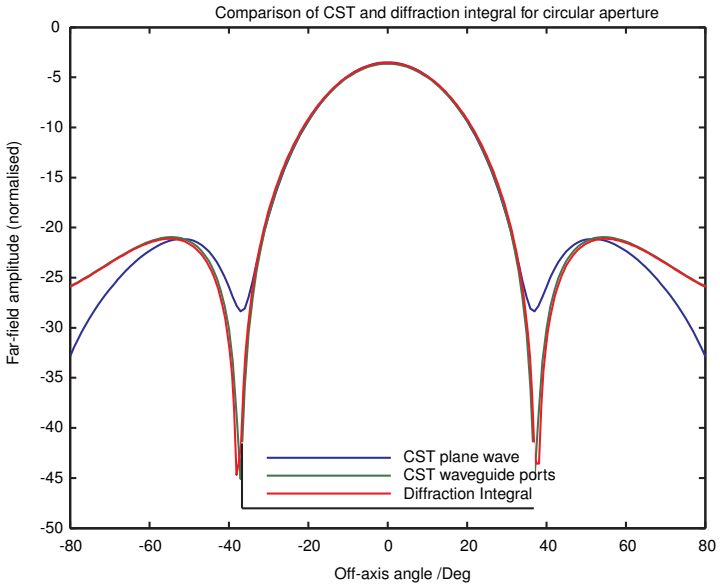

Figure 4.9: Comparison of CST plane wave source and waveguide ports with diffraction integral results for far field due to a circular aperture.

CST and optimising the output beam/ far field pattern. This could then be applied to systems involving KIDs with a layer of absorption material.
The interaction of the absorbing layer of a KID device with incoming radiation is complicated. Initially an ideal model using a resistive sheet as an equivalent absorbing layer will be used. The use of a matching layer over the absorber material could also be analysed and the use of a hemispherical could be included to investigate its influence on optical coupling.

It has been illustrated here that CST can be used using an extended waveguide port to launch a plane wave in a predictable way and this waveguide port function in CST allows the user to utilise all the S-parameter functionality of CST and track the propagation of power in all directions. The plane wave source inherent in CST does not offer this functionality and so is less attractive for the optical efficiency calculations required for KID detectors.

Chapter 5

Analysis of Multiple Reflections

5.1 Introduction

In this chapter we extend the standard GBM analysis techniques to allow the investigation of multiple reflections in quasioptcial systems. In the laboratory many quasioptcial measurements are affected by standing waves or multiple reflections from metallic holders or structures and the measured beams are modulated with periodic extra beam structure due to interference of reflected beams. There are standing waves present in most experimental setups but this can be minimised with absorptive material. In some cases, however, on-axis reflections are difficult to nullify. Here the ability to analyse standing waves is very important and we discuss an analytical technique and describe the application of the analysis in simple arrangements which best illustrate the effects of multiple reflections. In millimetre astronomy receivers the issue of standing waves is particularly troublesome if the instrument detects over a spectral range as the standing wave is a frequency dependent phenomena and appears as a ripple in the instrument response.

For example we may wish to simulate a quasioptical system consisting of a series of linearly spaced metallic rings, with electromagnetic radiation incident upon them. This is a nice example of the necessity to include multiple reflections to fully and accurately describe the output beam profile. This simple arrangement is illustrated in figure 5.1. The radius of the rings may be varied to examine the result, and indeed the ring can be made into a disc

by reducing the internal radius of the disc/torus to zero. It is also possible to vary the transmission/reflection ratios of the rings to emulate specific materials, rather than just a perfectly reflecting metallic ring, and in this way it is possible to create a classic Fabry-Perot type system in the millimetre-wave range. The simulations on the system described will be performed using GBMA primarily, in an extension of the theory described in chapter 2, and some use will be made of CST in an attempt to validate results. Figure 5.1 shows the general setup to be considered, where we have 2 metallic rings, 1 and 2, and these are separated by a distance, *Dis*. The internal radius of a ring is given by a, and the external radius by b, so that the internal radius of the first ring is a_1 and the external radius is b_1, and similarly for ring 2. Then, we are interested in the measured amplitude at ring 1, which will be the reflected amplitude or S_{11}, and the measured amplitude at ring 2, which will be the transmitted power or S_{21}, thereby including all possible reflections between ring 1 and ring 2. Figure 5.2 a side view of the system, and schematically illustrates the multiple reflections which can occur between the rings.

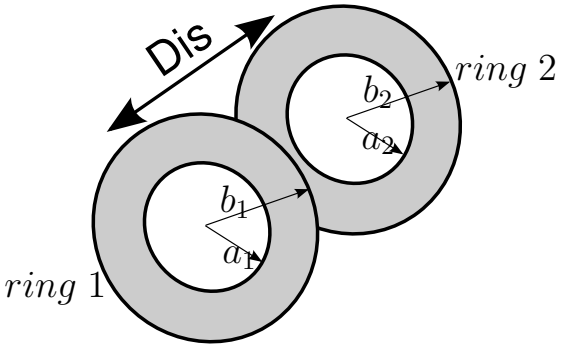

Figure 5.1: Multiple Reflections Setup. An alternative perspective is shown in figure 5.2.

Note, if we refer to reflection or transmission scattering parameter amplitude we mean the value of the S-parameter (described in section 2.11, whereas when we refer to reflection or transmission scattering parameter power or intensity, we are referring to the square of the S-parameter, or the power contained within it.

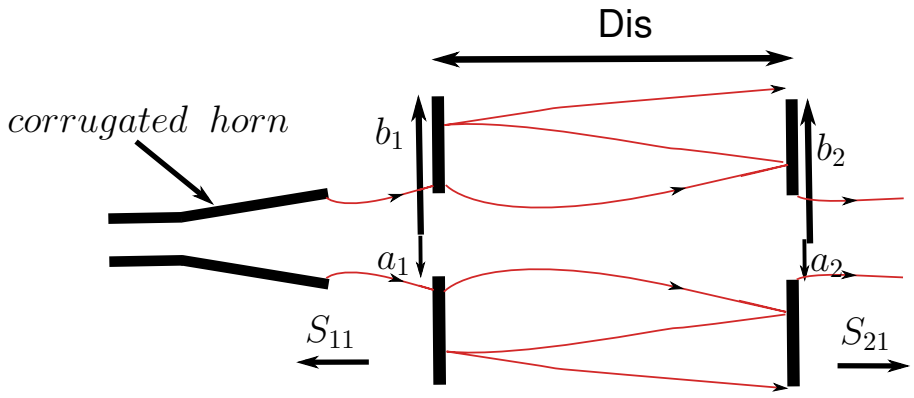

Figure 5.2: Section through multiple reflection ring setup showing corrugated horn and illustrating multiple reflections between the rings.

5.2 Description of GBMA of multiple reflections in free space

It is possible to analyse multiple reflections in this system using Gaussian Beam Mode Analysis utilising scattering matrices. The scattering matrix approach will be very similar to that used in *SCATTER* [39]. SCATTER is an in-house computational solution used for the design and analysis of feedhorns based on the propagation of waveguide TE and TM modes. Scatter uses a mode-matching technique to propagate power between neighbouring sections of the feedhorn. This is especially useful for corrugated feedhorns where the radius of the horn changes between each consecutive corrugation, but it is also used for smooth-walled horns where the radius flares linearly. While SCATTER uses waveguide modes with a TE and TM basis set, in our case freespace Gaussian modes will be required. SCATTER is complex and allows for a high number of corrugations/transitions to be considered to realise a complete waveguide structure. For our purposes with two rings, the scattering will be more elementary, where we consider power propagating from right to left and left to right. We will still require that the freespace modes are scattered in both the forward and backward direction, however, if we are to measure the S_{11} and S_{21} components.

We may think of the general procedure involved as follows:

1. *Initialise beam parameters.* This involves defining the usual beam characteristics at an input plane such as **wavelength**, **input beam radius**, **radius of curvature**, **number of modes**, and setting up the

ABCD propagation equations described in section 2.8.1 for **beam radius, phase shift, etc.** as a function of propagation distance.

2. *Introduce the first ring/disc using a scattering matrix for both the forward and backward direction.* The first ring is effectively represented by two scattering matrices (see section 2.12), and these must be computed. The matrices will be square, and the size determined by the number of modes invoked in the simulation. Each scattering matrix is calculated by integrating the Laguerre- Gaussian mode set of the input and output beams over a radial region described by the disc/ring in question. The scattering matrix for the reflected component is then calculated, and the matrix for transmission can be found by subtracting this from an identity matrix of equal dimension (i.e. T=1-R).

3. *Propagate the beam from the first ring through the distance specified,*i.e. if the distance between the two rings is e.g. 5 mm, the beam must now be propagated this distance, using ABCD matrices to find the beam parameters after such a distance to account for the beam diffraction, which will be required for the next step in the simulation.

4. *Introduce the second ring using an additional scattering formulation. Note: specific rules exist for cascading of multiple matrices and these must be followed* [40]. The process for computing the scattering matrices for the second ring is exactly the same as for the first ring. The matrix cascading processes may now be completed. We must cascade the matrix describing the reflection/transmission at ring 1 with the matrix describing propagation between the two rings. The specific rules for cascading two scattering matrices may be described as follows. Say we have two scattering matrices, S_a and S_b, such that

$$S_a = \begin{bmatrix} S_{11}^a & S_{12}^a \\ S_{21}^a & S_{22}^a \end{bmatrix} \tag{5.1a}$$

and

$$S_b = \begin{bmatrix} S_{11}^b & S_{12}^b \\ S_{21}^b & S_{22}^b \end{bmatrix}. \tag{5.1b}$$

Then, the resulting matrix, S_c, given by cascading the two matrices, is

found using the following formulation [41]:

$$S_c = \begin{bmatrix} S_{12}^a[I - S_{11}^b S_{22}^a]^{-1} S_{11}^b S_{21}^a + S_{11}^a & S_{12}^a[I - S_{11}^b S_{22}^a]^{-1} S_{12}^b \\ S_{21}^b[I - S_{22}^a S_{11}^b]^{-1} S_{21}^a & S_{21}^b[I - S_{22}^a S_{11}^b]^{-1} S_{22}^a S_{12}^b + S_{22}^b \end{bmatrix} \tag{5.2}$$

This cascading is performed, as mentioned above, for the first transmission/reflection matrix and propagation matrix. The matrix obtained from this cascading then gets cascaded with the transmission/reflection matrix describing the **second** ring, to give a final matrix, the terms in which give us our desired results. If this matrix is called S_{c1}, such that

$$S_{c1} = \begin{bmatrix} S_{11}^{c1} & S_{12}^{c1} \\ S_{21}^{c1} & S_{22}^{c1} \end{bmatrix}, . \tag{5.3}$$

then this will define our system completely in a steady state solution.

5. *Analyse the parameters of interest from the output.* As stated above, we are now interested in the terms from Equation 5.3. For instance, the term S_{11}^{c1} is the total S_{11} component, i.e. the reflected component at the first measurement plane, or that which is measured at plane 1 which also originated at plane 1. Also, the term S_{21}^{c1} will be the transmitted component, or that which is measured at plane 2 which originated at plane 1 and includes all forward reflections of the system. Both these terms are themselves also described using matrices. We will then wish to analyse these ratios of received and transmitted field magnitude, as a function of distance between the rings, and size of the rings, etc. We may find it instructive also to simply square these terms to obtain the beam intensity. This approach of using S-parameters and a cascading approach is a steady state solution and includes reflection and transmission for all internal planes when the total S_c matrix is calculated correctly.

5.3 Simulations performed using GBMA

We will now look at some results of simulations performed using Gaussian Beam Mode Analysis in the manner described above. As a very first example, we look at the situation where we have made both a_1 and a_2 zero, so that we are considering two flat reflecting discs. We make these large enough so that all of the input beam should be completely reflected, without any radiation

passing through to the detector plane at 2. The discs have a total radius of 10 mm. The incident radiation has a wavelength, $\lambda = 3$ mm (frequency of 100 GHz). The majority of these simulations will be performed at this wavelength, and if it is not explicitly stated, it can be assumed that this is the case. Considering that the input radius of the beam from the horn is ≈ 4.6 mm, this is more than enough to prevent any radiation from being detected at plane 2. Figure 5.3 shows the results of the GBM simulation for this setup. We see that the magnitude of the S_{21} component is zero, as expected. This remains constant regardless of the distance between the two discs, as it must, since no radiation can be transmitted through the first disc. Also, we find that the S_{11} component has a constant value regardless of the separation between the discs, with a value of ≈ 0.96. It seems obvious that the distance between the discs is irrelevant in this case, but this may not be the expected outcome for cases where radiation is being transmitted through the rings, as we shall see later. We note that the magnitude of the S_{11} component is ≈ 0.96, as previously stated. We may expect a value of 1, as all input radiation should be reflected backwards. However, the reason for this is the use in the simulation of a corrugated horn field. The input radius of curvature of the field from a corrugted horn is described by the slant length of the horn, in our case 80 mm. Now, the field has not propagated in space before being reflected from the metallic boundary, and when it is reflected it will have a radius of curvature which is negative. This beam will then not couple completely with our detector plane, as it is not a plane wave with a flat phase front.

Next, we look at the situation shown in Fig. 5.4, where both internal radii are equal to 3 mm, and both external radii are equal to 5 mm. i.e. we have rings with apertures of 3 mm and a reflective (metallic) surface from 3 mm to 5 mm.

When this setup is run using GBMA, we get the result shown in Fig. 5.5. We note that the S_{21} decreases as the distance between the two rings increases. This may be explained by the divergence or spreading out radially of the beam as it propagates. When the beam has not travelled any distance, its radius is around 4.5 mm. Therefore, a large proportion of the amplitude of the entire beam (1) actually makes it through the first and second rings. As the distance between both rings increases, however, the beam spreads out and so more power is reflected off the ring. Travelling even farther than the

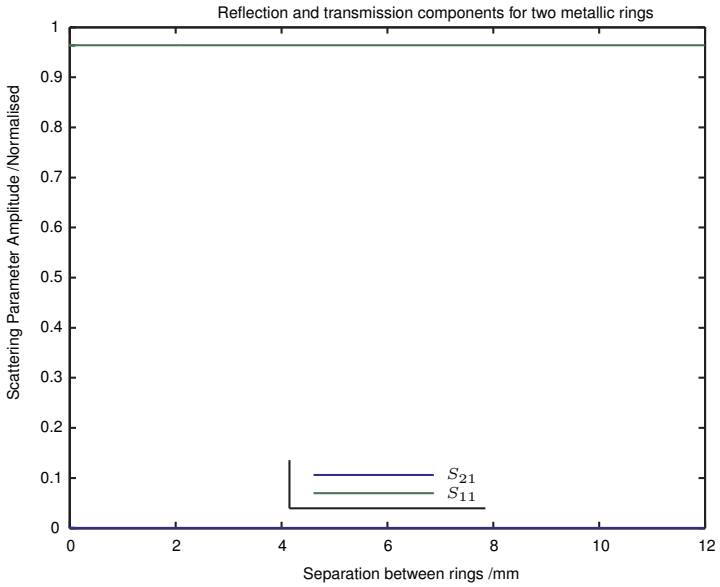

Figure 5.3: S-parameters for two rings (discs) having a1, a2=0 mm, b1, b2=10 mm, for ring separations from 0-12 mm.

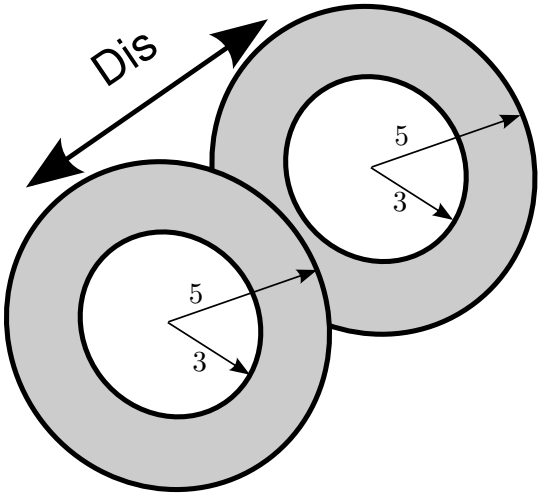

Figure 5.4: Multiple Reflections Setup with both internal and external radii equal, at 3 mm and 5 mm respectively.

12 mm we have simulated here should result in an increase again in the S_{21} figure, as we also measure the radiation which has spread to farther than the external radius of the ring. Now looking at the S_{11} for this problem, or the reflected component, we note that it is on average increasing, as our propagation distance increases. Also of note is that we obtain a series of maxima and minima in the reflection profile. Closer inspection shows the separation between successive maxima and minima to be of the order of $\lambda/2$, in this case 1.5 mm.

We now perform a similar simulation, with one parameter changed. We keep

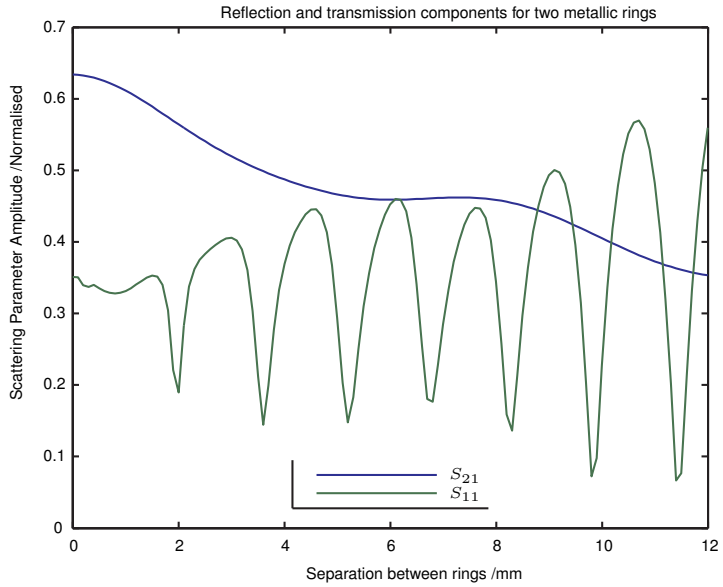

Figure 5.5: S-parameters for two rings having a1, a2=3 mm, b1, b2=5 mm, for ring separations from 0-12 mm.

a_1= 3mm , but make a_2= 0 mm, while fixing both b_1 and b_2 at 5 mm. Thus, we are keeping the first ring the same, but making the second ring a reflecting disc.

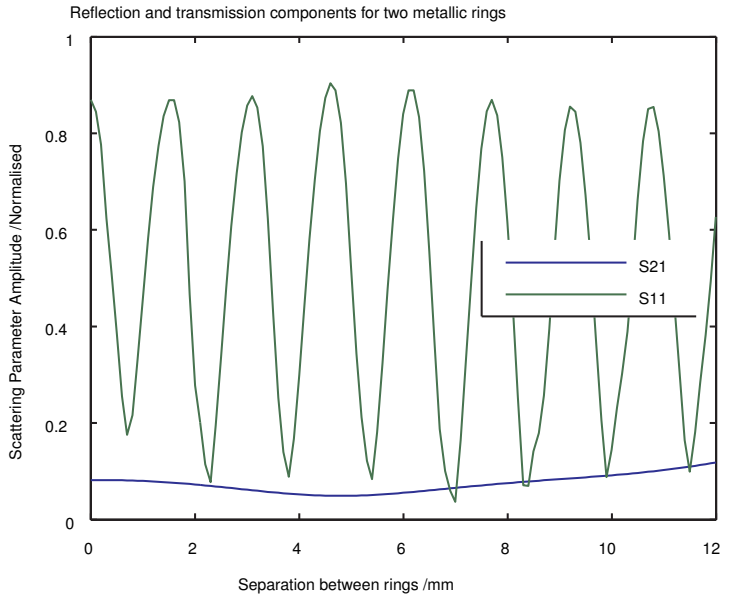

Figure 5.6: S-parameters for two rings having a1=3 a2=0 mm, b1=5 mm b2=5 mm, for ring separations from 0-12 mm.

Figure 5.6 shows the result of this simulation. We obtain a much lower value for the S_{21} parameter in this case, explained by the fact that we have a reflecting disc of radius 5 mm where most of the radiation would likely be

incident, and this radiation is reflected back to the first ring, where it is either measured at plane 1, or reflects again, perhaps multiple times, between the two metallic rings. Also, the S_{11} has correspondingly high values, which are relativley consistent on average, with propagation distance. As in figure 5.5, we again observe the half-wavelength characteristic of maxima and minima. For our next simulation, we shall again vary one parameter, and simply make the disc at plane 2 bigger, so that in fact more radiation should in fact be reflected from it. We will set it as being a disc of radius 25 mm, so that our parameters are $a_1 = 3$ mm, $a_2 = 0$ mm, $b_1 = 5$ mm $b_2 = 25$ mm.

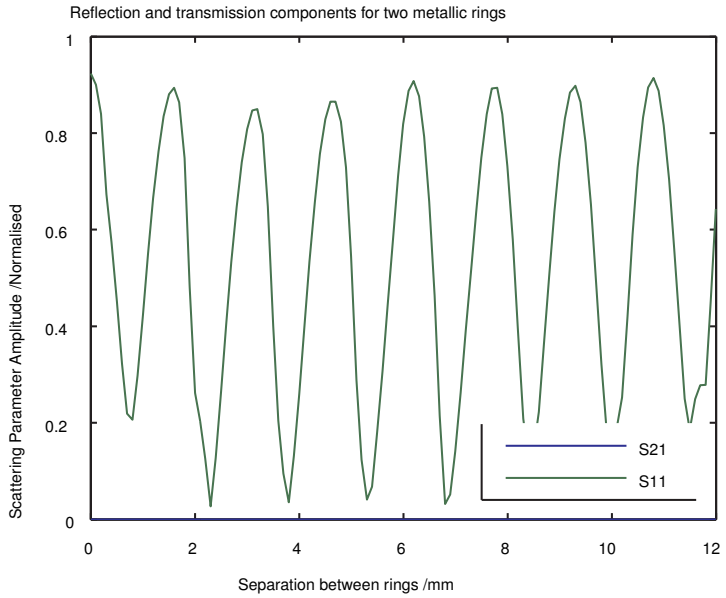

Figure 5.7: S-parameters for two rings having a1=3 a2=0 mm, b1=5 mm b2=25 mm, for ring separations from 0-12 mm.

Figure 5.7 shows the results of this simulation. We find that the significant increase in the radius of ring 2 indeed prevents any signal from being recorded at that plane. The measured S_{11} appears to be approximately the same as in the previous case, with a very small on average increase, and the period of the maxima and minima in the S_{11} pattern equal to $\lambda/2$, as in the previous cases.

As another example, we wish to examine a case where we expect a high value in the S_{21}, at least when the separation is very small. We will set both rings as the same size, and set the aperture to be approximately the same size as the input beam. Then, the S_{21} should have a maximum value when the separation between both rings is at its smallest and most of the radiation will pass directly through to plane 2 and will be included in the S_{21} parameter. We thus set our parameters as follows: We will set it as being a disc of radius

25 mm, so that our parameters are a_1= 4.6 mm, a_2= 4.6 mm, b_1= 6 mm b_2= 6 mm. Figure 5.8 shows the resultant beams in this case. We observe

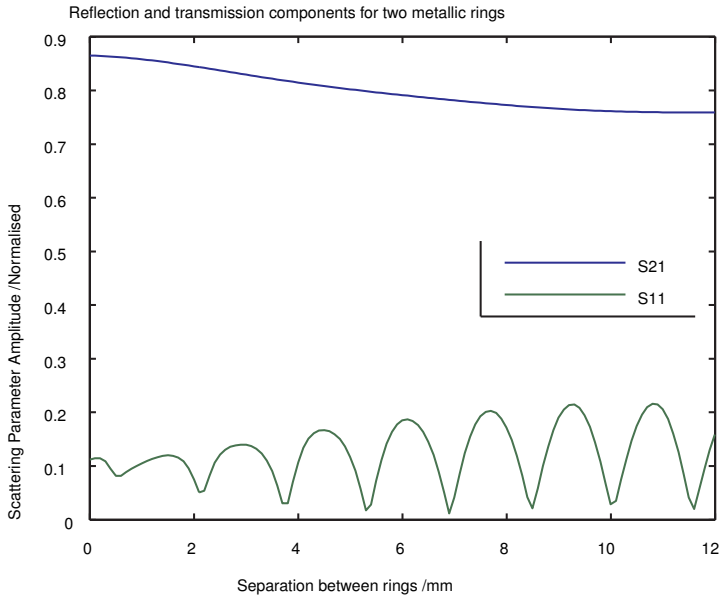

Figure 5.8: S-parameters for two rings having a1= 4.6 mm a2= 4.6 mm, b1= 6 mm, b2= 6 mm, for ring separations from 0-12 mm.

that indeed the S_{21} has its maximum value when the separation betwen the rings is zero, and only decreases marginally as the separation increases. As the beam diverges upon propagation, some of the beam will be reflected from the ring and may be measured at plane 1 as the S_{11} or may reflect back again, etc. However, the metallic ring is very narrow, and therefore this accounts for only a small portion of the beam, especially as the beam diverges significantly, and that radiation is then measured again at plane 2. For this reason, the S_{11} is much lower than in any of our previous examples, although it does increase on average as the distance between the rings increases.

Now, we wish to investigate the effect of varying the transmission ratio of the rings. Figure 5.9 shows the result for two discs of radius 10 mm. The first disc has been modified so that it has both a reflection and transmission ratio of 0.5. We compare this to figure 5.3, for discs of the same size, but with 100% reflection as in all previous cases. Rather than having a constant value of zero for the S_{21}, we now obtain a constant value of ≈ 0.25. the value is constant with propagation distance up to 12 mm as the beam is still narrow enough to be contained entirely within the radius of disc 2, and so 50% of the radiation that makes it through the first ring (itself 50%) is measured at plane 2. The S_{11} shows similar characteristics as previously, with a lower

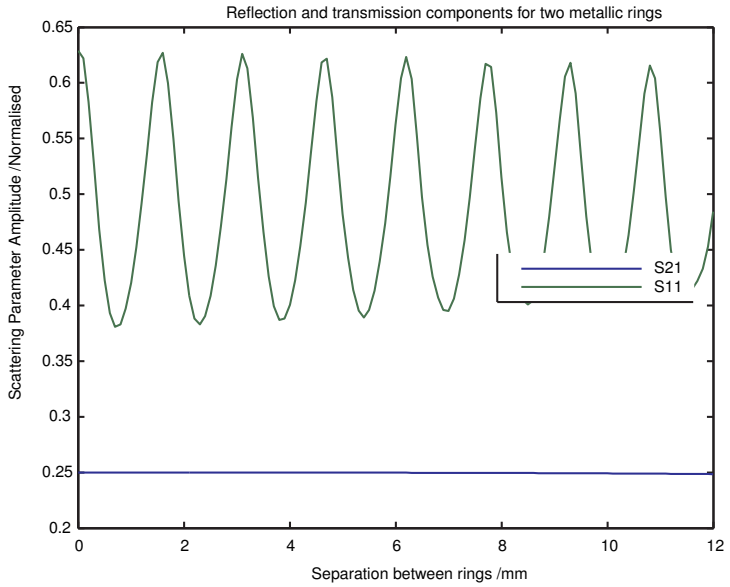

Figure 5.9: S-parameters for two rings having a1= 0 a2=0 mm, b1= 10 mm, b2= 10 mm, for 50 % transmission, 50 % reflection in disc 1, for ring separations from 0-12 mm.

average value (as some of the radiation is now not reflected).

5.4 Cavity Standing Wave Investigation

Using the cascading matrix approach with freespace GBMA modes we have investigated the form of multiple reflections themselves between two metallic rings/discs, of varying size and transmission, etc. We have continuously found standing wave effects present in such systems and we can analyse its form. These would appear as a function of the distance between our two metallic objects, periodically at values of $\lambda/2$. We would like to investigate the mechanism behind this effect. We may look at a true Fabry-Perot type system, as decribed in figure 5.10. Here, we have set the wavelength to 0.6 mm.

A method of identifying the modes present inside the cavity involves examining a specific component of the cascaded system matrix described in section 5.2. The component in question is $[S^a_{22}][S^b_{11}]$. After some investigation it can be shown that this component describes the round trip component in the system [42], and it is this component that we wish to analyse the form of the standing wave. A method for isolating the cavity modes that propagate between the discs in the cavity is described in [42]. This technique will involve the use of eigenmodes and eigenvectors, components of a square matrix. The

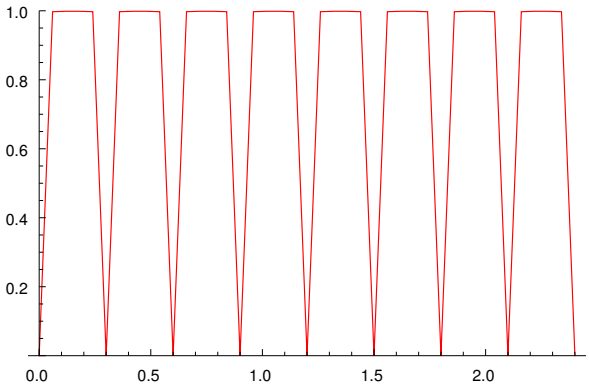

(a) S_{11} as a function of distance between discs for Fabry-Perot cavity.

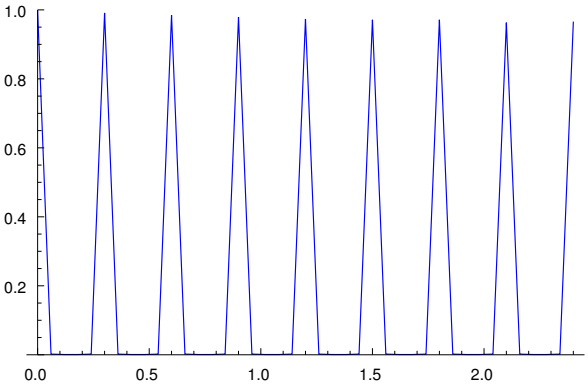

(b) S_{21} as a function of distance (in mm) between discs for Fabry-Perot cavity.

Figure 5.10: S_{11} & S_{21} patterns as a function of distance (in mm) between discs for Fabry-Perot cavity at a wavelength $\lambda = 0.6$ mm.

eigenmode of a matrix is a solution to the equation

$$S \cdot a = \lambda \cdot a, \tag{5.4}$$

where S is a scattering matrix, here representing the round trip through the system, a is a vector, and λ is the eigenvalue, where a is known as the eigenvectors. λ can be a real or complex number. The eigenmodes of an optical system can be determined numerically, and the spatial form of these modes, $\sigma_{forward}$, are described by

$$\sigma_{forward} = \Psi_{out} P, \tag{5.5}$$

where Ψ_{out} are the basis set evaluated at the output plane and the P are columns of eigenvectors from the matrix. The round trip component is then decomposed into its eigenvalues and eigenvectors through the equation

$$S = PDP^{-1}, \tag{5.6}$$

where P is a matrix composed of the eigenvectors of S and D is a diagonal matrix of the corresponding eigenvalues $\lambda_1, \lambda_2, \ldots, \lambda_n$.

Then, we track the eigenvalues and eigenvectors of the round trip component as the distance between the discs is changed and the standing wave profile changes. The reason that we track these parameters is that we wish to find out if there is a characteristic change in any of these parameters as a resonance point is reached in integral values of $\lambda/2$ as with all multiple reflections, and a sudden peak is observed in the transmission profile. We examine a resonant peak in transmission in terms of its eigenvalues, and the results are presented in table 5.1 and we want to investigate what is different in the SVD decomposition at this special resonant case.

Table 5.1: First 10 eigenvalues of the cavity round trip matrix at a distance betwen the discs of 0.3 mm corresponding to a resonant peak in the transmitted power.

Eigenvalue /#	Abs. value	Argument /Rad
1	0.9498	0.0003
2	0.9416	0.1495
3	0.8829	0.6153
4	0.7068	1.6850
5	0.4020	-2.6090
6	0.2238	-0.0330
7	0.0008	-1.7686
8	0.0000	-2.4311
9	0.0000	-2.8590
10	0.0000	0.2681

In [42] it was found that certain eigenmode arguments are zero at resonant points. Analytically setting this eigenmode to zero and performing the analysis again should confirm or deny this, as, if that eigenmode is mainly responsible for the resonance, then its removal should cause the resomance to diminish.

From table 5.1, the argument of the first eigenvalue is closest to zero. We attempt setting this eigenvalue to zero and observing the results. The matrix of eigenvalues in the SVD analysis is a diagonal matrix so we can set any eigenmode to zero analytically by multiplying this eigenvalue by zero.

Figure 5.11 shows the S_{21} profile for the case where the $1^{\mathbf{st}}$ eigenvalue has been analytically set to zero. Virtually no power remains in the S_{21}, showing that

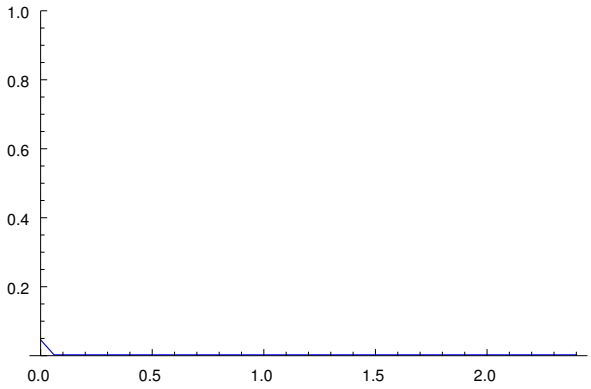

Figure 5.11: S_{21} profile as a function of distance (in mm) when 1st eigenvalue has been analytically set to zero.

removing this mode from the simulation completely removes the S_{21} power. This indicates that this eigenmode actually contains all round trip power and is responsible for the resonant peaks in the S_{21} profile. We confirm this by removing another randomly chosen mode, giving the result shown in figure 5.12. We have instead removed the $4^{\mathbf{th}}$ mode in this case, and we observe that all of the resonances are inded still present, indicating that it is the 1st eigenmode which contributes to the resonances in the transmission profile. We are considering a very simple system, and perhaps it is not surprising

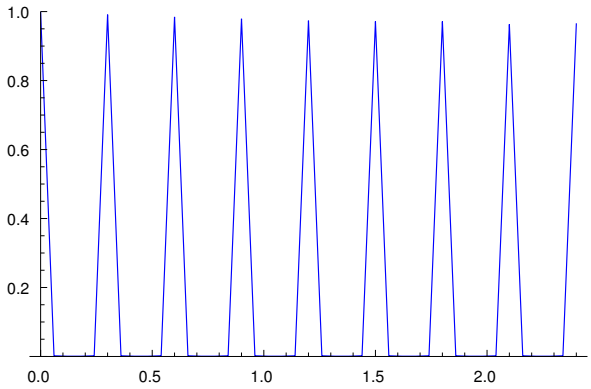

Figure 5.12: S_{21} profile as a function of distance (in mm) when 4th eigenvalue has been analytically set to zero.

that only one mode is responsible for the resonances inside the cavity.

We shall now examine the form of this mode and compare it with a Laguerre-Gaussian mode of the same order. (the expected cavity mode for such a geometry). By isolating the first mode from the cavity field and performing the standard modal summation, we plot the form of this mode and compare with the Laguerre-Gaussian mode of order zero. The result, as shown in figure 5.13(a) and figure 5.13(b), is complete agreement between the two

modes, showing that our dominant cavity mode which is responsible for the resonances is indeed the fundamental Laguerre-Gaussian mode.

We also wish to examine the form of some of the other eigenmodes. We plot these along with the equivalent order Laguerre-Gaussian modes to show their equivalences. Figure 5.14 shows the second and third cavity eigenmodes plot-

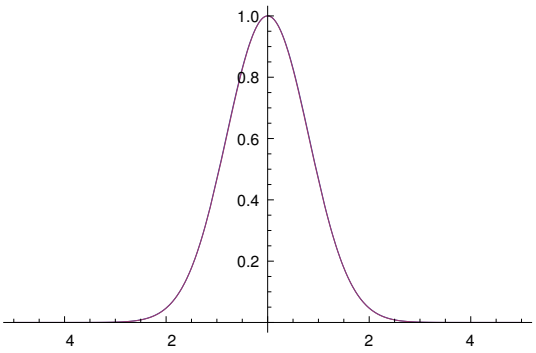

(a) Comparison (overlay) of 1st cavity eigenmode and equivalent Laguerre-Gaussian mode (2D).

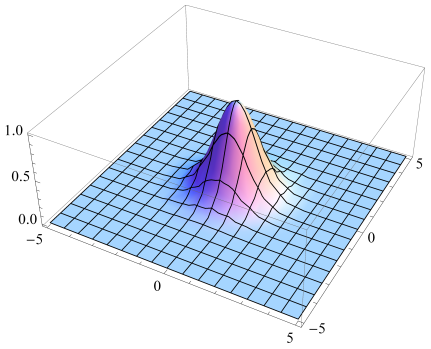

(b) Comparison (overlay) of 1st cavity eigenmode and equivalent Laguerre-Gaussian mode (3D).

Figure 5.13: Comparison of 1st cavity eigenmode and equivalent Laguerre-Gaussian mode.

ted with the corresponding Laguerre-Gaussian mode of the same order. We see that in both cases, we obtain perfect agreement, as in figure 5.13. Note that we have just plotted these modes to confirm that the modes present in the cavity are the Laguerre-Gaussian modes, and they are normalised to give unity power on-axis. They are not dominant in the cavity, as we have proven that the fundamental eigenmode is responsible for the resonances.

We have investigated the form of cavity modes in a Fabry-Perot type cavity with circular geometry, and we were able to isolate the mode which was resposible for the resonant conditions and illustrate that the form of the cavity modes present were of the expected Laguerre-Gaussian profile. This was done using decomposition of the matrix into its eigenvalues and eigenvectors, and from this we were able to show the form of the mode and relate it to standard Laguerre-Gaussian shape.

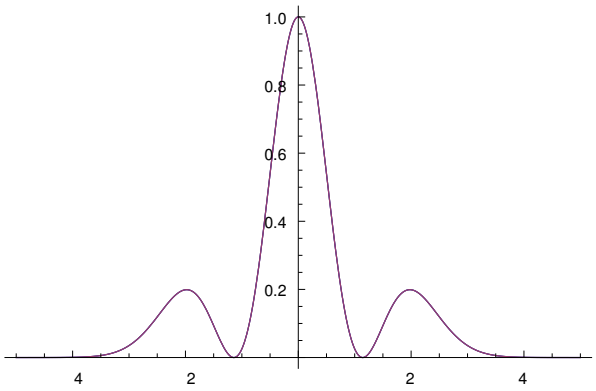

(a) Comparison of 2nd cavity eigenmode and equivalent Laguerre-Gaussian mode .

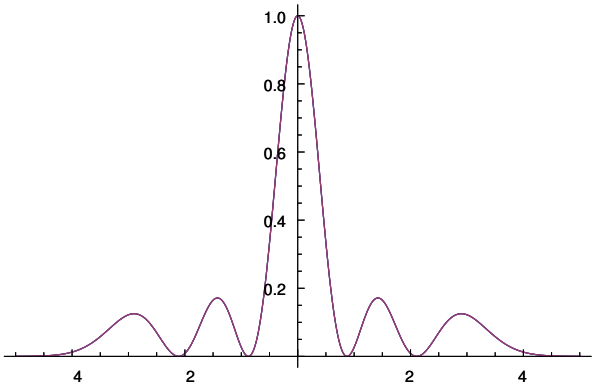

(b) Comparison of 3rd cavity eigenmode and equivalent Laguerre-Gaussian mode .

Figure 5.14: Comparison of 2nd and 3rd cavity eigenmodes and equivalent Laguerre-Gaussian modes.

Chapter 6

SAFARI Cavity Analysis

6.1 Introduction/Background

The **SP**ace **I**nfrared Telescope for **C**osmology and **A**strophysics (SPICA) is a proposed Japanese-led joint JAXA-ESA mission, and an artist's impression is shown in figure 6.1. SPICA is provisionally scheduled for launch to Earth's second Lagrangian point (L2) in 2022. At the present time (autumn 2013), a final decision is to be made to commit resources and make the mission official. Europe, through the European Space Agency (ESA), will contribute significantly to the mission with technical expertise gained from the successful Herschel mission. SPICA's specific focus will be planetary system formation and galactic evolution [43]. The telescope itself will have a diameter of 3.5 m and will be cryogenically cooled to < 6K. At such a temperature, the telescope's thermal emission will be lower than the sky background over the far-infrared range down to 1.4 THz. This will enable the use of instruments having sensitivities much higher than on Herschel (section 1.2.3). SPICA will consist of three main instruments:

- a mid-infrared (MIR) coronagraph ($\sim$3.5 to $\sim$27 μm) with photometric and spectral capabilities (R $\sim$200)
- a MIR wide-field camera and high resolution spectrometer (R $\sim$30,000)
- a far-infrared (FIR $\sim$34 to $\sim$210 μm) imaging spectrometer (SAFARI)

SAFARI is the instrument to be delivered by the European Space Agency (ESA) and we shall give a brief description of it here. ESA will also develop the 3.5 m telescope itself.

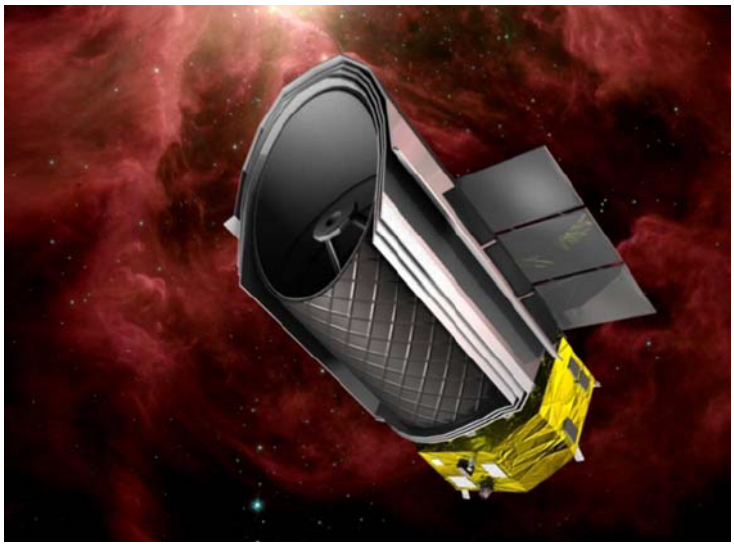

Figure 6.1: Artist's impression of the SPICA spacecraft. Source:[44]

Two important areas where SAFARI will make improvements are in the areas of photometry and spectroscopy. In terms of photometry, SPICA's cold telescope will enable deeper and faster mapping of large areas of sky than Herschel's PACS instrument [44]. SAFARI will have the ability to make maps of 10's of square degrees af sky area, resolving structures at a maximum of around 1°. In spectroscopy, SAFARI will make even bigger breakthroughs. SPICA's high sensitivity will enable spectoscopic mapping of large areas of sky and large numbers of soucre samples over the far-infrared spectrum, rather than observations of small numbers of relatively bright sources and individual spectral line mapping.

SAFARI's $\sim$34 to $\sim$210 μm range is to be divided into sub-bands, the short wavelength limit being defined by the overlap with the MIR instrument, while the long wavelength limit is to be defined by the [NII] fine structure line. An array of detectors are used in each band. The three bands which will be included are the L- $35 - 70\mu$m, M- $70 - 110\mu$m and S-bands $110 - 210\mu$m referring to the long, medium and short wavelength bands, respectively. The proposed detector arrays are of the following sizes

- L-band: 64×64 (4096 pixels)
- M-band: 38×38 (1444 pixels)

- S-band: 20×20 (400 pixels)

giving a total across all three bands of 5940 pixels [45].

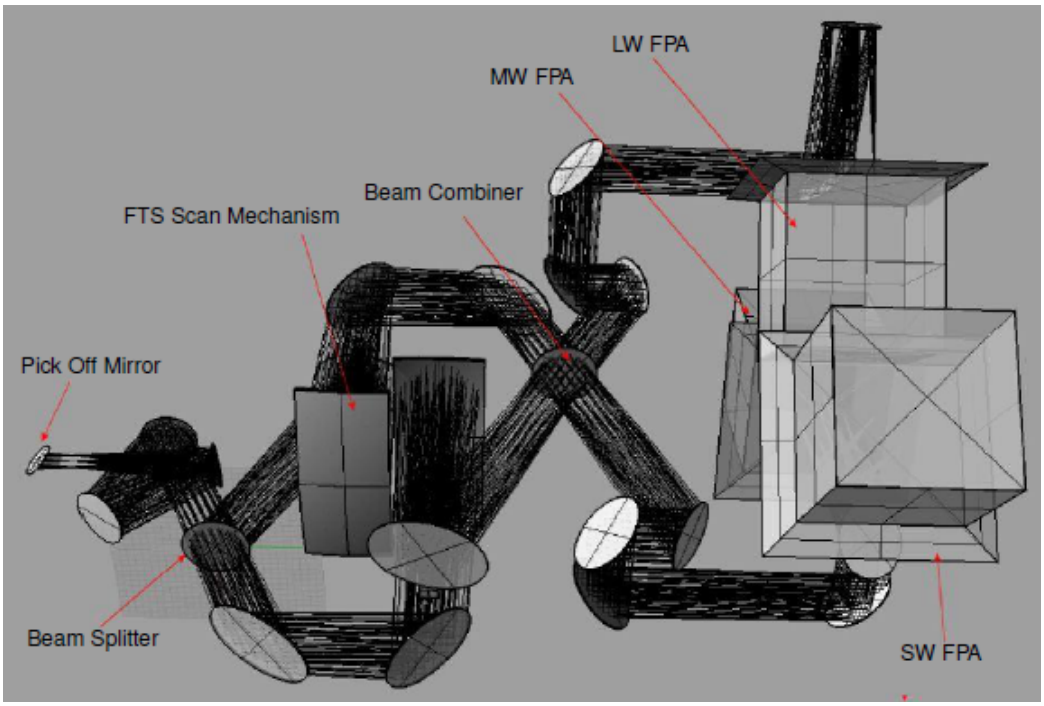

Figure 6.2: SAFARI Front End Optics (FRE). Source:[46]

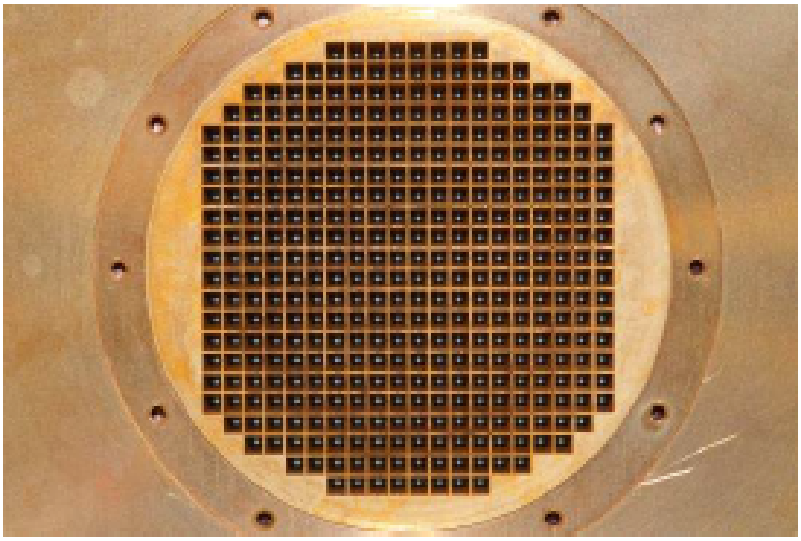

Figure 6.3: Photograph of L-Band 388 pyramidal horn array (front). Source: [44]

The proposed optical setup is shown in figure 6.2, and a brief glossary of relevant terms is as follows: FTS- Fourier Transform Spectrometer, FPA- Focal Plane Array, LW- Long Wavelength, MW- Mid-Wavelength, SW- Short Wavelength. The input optics re-image the pupil for stray light control, and expands and partially collimates the beam entering the spectrometer. The

beam combiner produces interference beams in the two output arms [43]. The beams are then focused onto the FPAs. The Focal Plane Arrays consist of an array of horns feeding into detector cavities. The chosen detectors are Transistion Edge Sensor (TES) bolometers. Their use is complicated by the fact that they must be operated at very low temperatures (<1K), their spectral response in the wavelength band around 40 μ m is much better than photoconductors, another considered technology. TES bolometers are thermal sensors that measure temperature changes by the increase in resistance of a superconducting film biased within the superconducting-to-normal transition. Figure 6.4 illustrates the TES principle in a molybdenum-copper thin

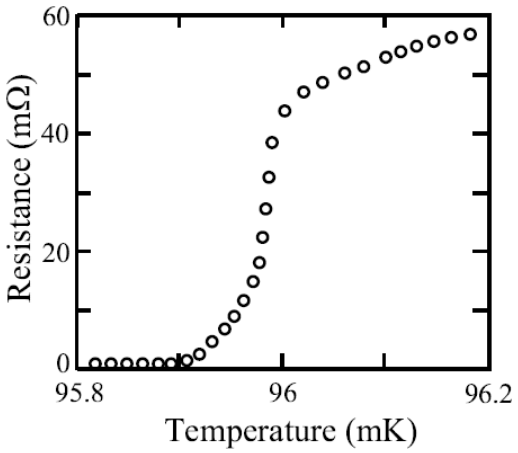

Figure 6.4: Illustration of the superconducting transition in a Mo/Cu film near 96 mK. Source:[47]

film. The sharpness of the phase transition illustrates its use as a sensitive thermometer [47]. The properties of the TES can be adjusted, i.e. changing the relative thickness in the film of the normal metal (copper here) and the superconducting metal (molybdenum here) changes the transition temperature. The physics of the operation of TES detectors and the readout electronics are not described in detail here. NUI Maynooth are commissioned to characterise the optical behaviour and performance of these detectors which are to be housed in waveguide structures. This analysis is complicated by the fact that the detectors are housed in waveguide structures, requiring a waveguide modal analysis and are also multimoded (partially coherent rather than the traditional coherent radio astronomy detector).

As SAFARI is targeting the THz region of the EM spectrum, this is truly far-infrared (FIR) astronomy. Radio and submillimetre astronomy would typically use single moded devices as detectors and this could be described

completely as coherent radiation. To make a horn antenna feed a single moded detector, the waveguide cross sectional area (usually either a circular or rectangular waveguide) is reduced in diameter to ensure only one mode can propagate. The presence of only one mode means that the radiation is fully coherent. In FIR astronomy multimoded (the waveguide cross section is increased to allow n modes to propagate and what is detected is a sum of partially coherent modes) detectors are used to help increase the sensitivity to potentially detect fainter astronomical signals. As more than one mode is detected and modes all propagate independently the signal detected is effectively incoherent and is more complex to analyse compared with traditional radio astronomy detectors.

The challenge for the optical analysis of the SAFARI detectors is to build a complete optical model of the waveguide structure (horn antenna and detector cavity) so that we may model its interaction with the optical train in front of the detector array in the focal plane of SAFARI. In this chapter a number of waveguide structures will be investigated to analyse their ability to successfully absorb incident radiation.

Practically, by illluminating a waveguide structure and monitoring the returned (undetected) power referred to as the S_{11} component we can measure how efficient the waveguide structure (with detector modelled) is at operating at a certain wavelength.

Optical power coupling to the detector system is of great importance. Each horn in the horn array feeds into a cavity containing an absorber and TES detector.

Figure 6.5(a) shows a schematic of a proposed design for a SAFARI detector pixel in the optical testbed, illustrating effectively one single pixel of the detector array. Incoming radiation from the horn is fed into the cavity containg the TES absorber. The absorber is attached to the TES detector which sensitively monitors the absorbed power through the relationship shown in figure 6.4. Note the air gap which is required as the horn array has to be mechanically attached to the detector array, and each is physically maufactured seperately. The spherical backshort then creates a cavity effect, and the function of this is that power not absorbed by the detector on its initial pass should be reflected in the cavity and absorbed. The "500" in the figure refers to the diameter of the cyclindrical backshort, which is 500μm.

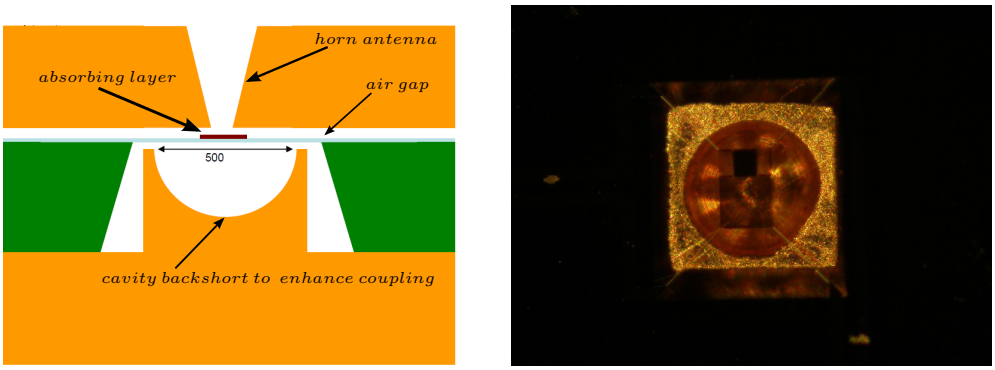

(a) Illustration of proposed detector system optical testbed.

(b) Photograph of an S-band pixel mounted in front of a gold plated copper machined hemispherical cavity.

Figure 6.5: SAFARI pixel schematic and TES photgraph. Source: [45].

Figure 6.5(b) contains a photograph of a TES absorber mounted in front of a cavity. The SAFARI consortium have initiated a development programme for the TES detector focal plane array and NUI Maynooth are involved in investigating different geometries and waveguide structures to house the TES detectors in order to maximise optical coupling of the incident beam.

In modelling the optical coupling to a TES detector the behaviour of the bolometer in relation to the incident radiation must be modelled. The operation of the bolometer is dependent on an absorbing layer of material that is exposed to EM radiation and responds with very subtle temperature changes which affects the resistance of the material. This involves the solid state interaction of the absorbing material and the FIR photons. This is a complex physical interaction to model so in the optical models described here we use a *resistive sheet model* of the absorbing layer. In fact, some software packages such as CST include an ideal infinitely thin resistive sheet element. Normally the sheet resistance is a function of the bulk resistivity of a metallic film and its thickness. Sheet resistance R_{sh} is given in units of Ohms per square, where squares are the unitless dimension of the length divided by the width.

In SAFARI the absorbing layer will be a thin metallic layer of Tantalum deposited on silicon nitride and will be given a sheet resistance (through manufacturing) to match the impedance of the incident radiation (having a value close to 377 Ω). In our optical models an equivalent ideal absorber will be used and we will monitor the optical efficiency (returned power back

out of the waveguide (S_{11})). A resistive sheet model has also been used in SCATTER (in-house mode matching code). Use will be made of this in section 6.3, where a resistive sheet is placed insde a waveguide and the absrorbed power is measured. This will allow for a comparison of the resistive sheet models in both SCATTER and CST for a simple case to verify their operation.

6.2 Investigating the Optical Behaviour of a Simple Detector Cavity

As part of designing the SAFARI detector system, analysis has been carried out at NUI Maynooth in modelling the cavity and horn setup with absorber material, in CST and SCATTER, the inhouse software developed at NUI Maynooth. Much of the cavity modelling is presented in the thesis of Dr. Stephen Doherty, as well as analysis of pyramidal horns using a custom version of SCATTER, and more information on this can be found in his PhD thesis [43]. Experimental measurements were also performed on cavities at Maynooth, with different cavity geometries in order to validate simulation results. The facilities do not allow for exact experimental measurements with an equivalent SAFARI type TES detector arrangement, as cryogenic cooling facilities are not available. However, performing simple cavity measurements at room temperature on various different cavity geometries should still enable us to understand the physics involved and allow optimization of the cavity geometry for the optimum optical efficiency for these simpler optical setups.

To this end, a cavity housing which may be adjusted in size has been conceived. Figure 6.6(a) shows a narrow opening into a hollow cavity. The back wall of the cavity may be moved using a plunger mechanism, so that the cavity size may be easily adjusted. Also, the plunger may be removed completely so that an item such as an abosrber may be placed into the cavity and measurements performed. Figure 6.6(b) then shows the same system containing a number of detectors, with electronics to read out the signal. Figure 6.6(c) then shows a face view of the plunger mechanism/ back of the cavity, as seen through the entrance slit or waveguide, assuming it were cyclindrical. By rotating the plunger in a controlled manner, it may be possible to map the

field at every point inside the cavity.

It is intended that such a device may be produced for experimental measurements at the Tyndall National Institute in Cork. A potential method of realising the detector(s) inside the cavity is to use patch antennas, which will be discussed later in section 6.5.

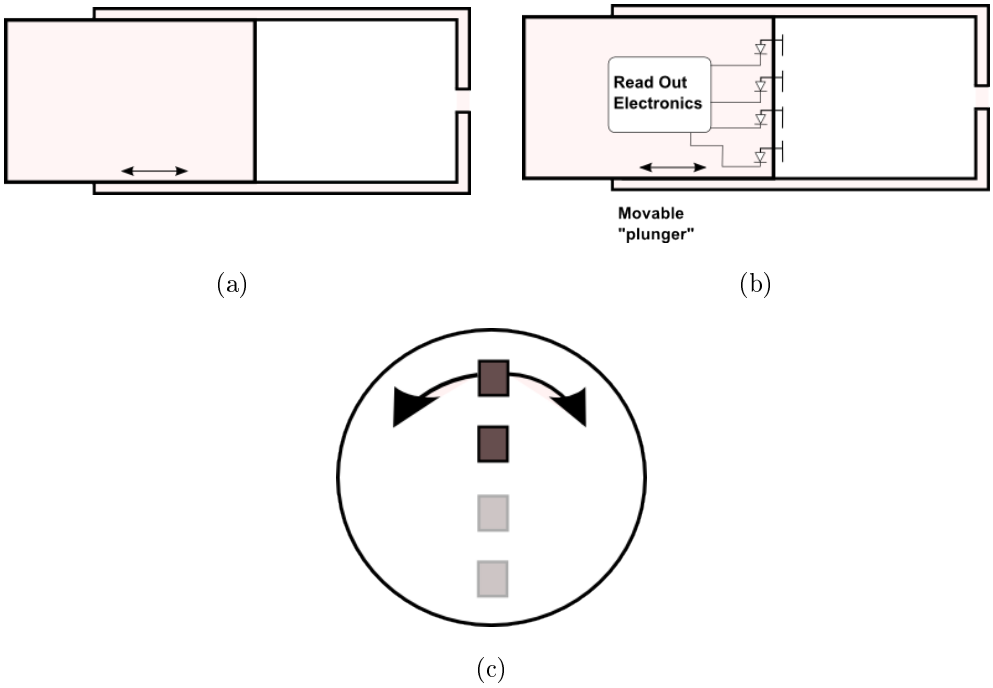

Figure 6.6: Cavity with rotatable plunger mechanism.

Simulations will be performed using CST on simple cavity geometries, which are small enough to be meshed and modelled using CST on a standard PC. These structures may be smaller and simpler than the SAFARI cavities, but they will allow us to further undersand and verify the optical performance of cavities containing absorbing material. We will require the use of absorbing material to approximate the absorbing TES material in SAFARI itself. An empty closed cavity will always reflect 100% of the incident input power as it contains no loss mechanism. We plan to use thin metallic films to simulate the superconducting TES layer of SAFARI.

6.3 CST Comparison with SCATTER

As we are planning to make extensive use of CST in this chapter for the analysis of cavities containing absorber material and patch antennas, it is impor-

tant that we undertake to verify the methods used and results found using CST. To this end, we will make a comparison with SCATTER, the previously mentioned in-house software package designed for analysing waveguides and feedhorns using waveguide modes and mode matching.

We will first take a very simple example of a circular waveguide containing a circular absorbing ohmic sheet which completely fills the width of the waveguide. The waveguide is set to 20 mm long and has a radius of 1.5 mm, i.e. $\lambda/2$ at 100 GHz (λ= 3 mm). The absorber then is modelled as an infinitely thin disc of diameter 3 mm, which is equal to λ at 100 GHz. The waveguide size is chosen so that it will be single-moded, that is to say it will only support the propagation of the fundamental TE_{11} mode. We will perform the simulations at 100 GHz and vary the surface impedance of an infinitely thin sheet from (close to) 0 Ω to $2z_0$, where z_0=377 Ω is the impedance of free space, in steps of 0.25 z_0. The second, closely related example will be using a circular wavguide of the same dimensions, except that this waveguide will be closed at one end to simulate the simplest possible cavity, i.e. a resonant single moded cavity. The absorber will then be placed $\lambda/4$ (0.75 mm) from the closed end. We expect to find resonance with the absorber at or near this point for a single-moded waveguide, and achieve maximum absorption with the ohmic sheet. Figure 6.7 shows both of these cases setup in CST.

These simulations are in fact very straightforward for SCATTER, as they do not contain a large number of waveguide sections to scatter across. By contrast, the simulations take considerably longer in CST, as they are generally performed across a bandwidth, whereas we desire only a spot frequency of 100 GHz for our comparison with SCATTER. This is the reason that we have only performed the CST simulation at a small number of surface impedances, as each unique impedance value requires a unique simulation. For example, each CST simulation with a unique impedance value takes of the order of 1 hour on a high-end PC within the department which contains 64 GB of RAM. In contrast, the simple SCATTER simulation for a large number of impedance values at a spot frequency takes of the order of 1 minute.

Figure 6.8 shows the result of the simulations performed using both SCATTER and CST for the open waveguide. As previously stated, the CST simulations were performed in increments of the absorber surface impedance of $0.25 \times z_0$, for a total of 9 simulations, whereas the SCATTER simulation was performed over using a very fine step. The result shows excellent agreement

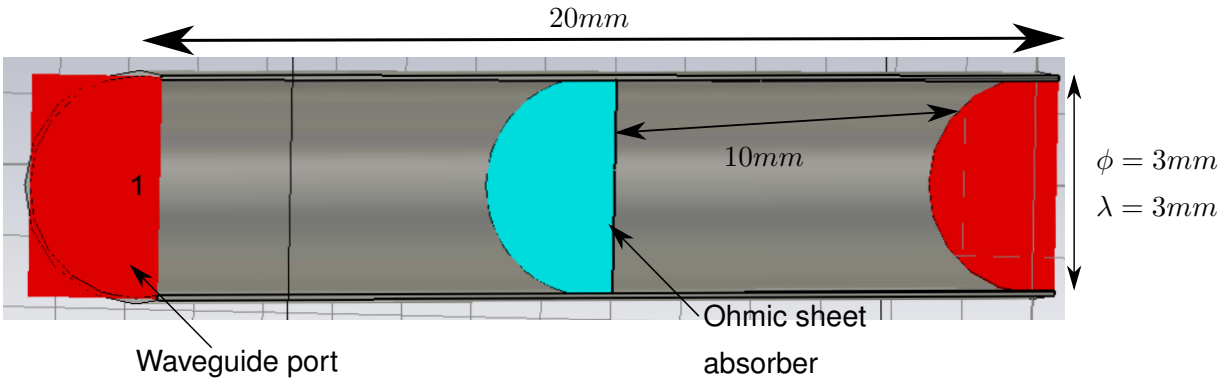

(a) Circular waveguide open at both ends containing absorber midway along its length.

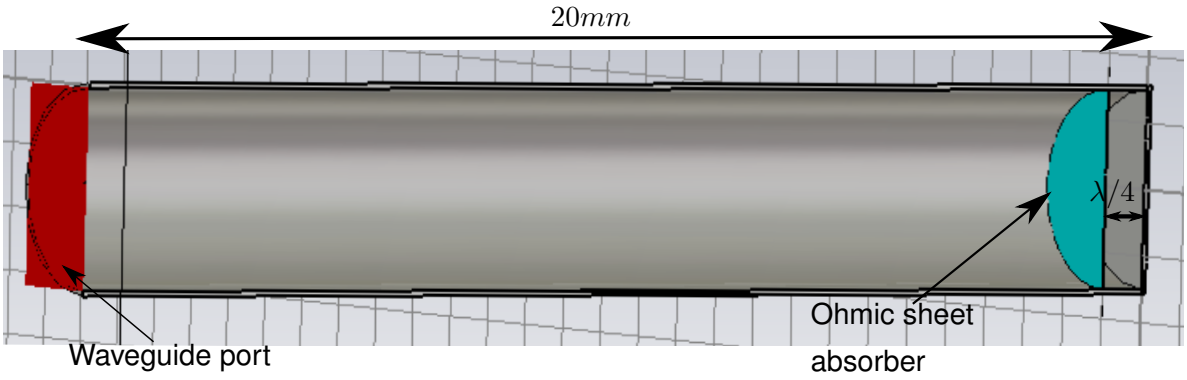

(b) Circular waveguide closed at one end containing absorber at $\lambda/4$ from the closed end.

Figure 6.7: Circular waveguide of length 20 mm and radius 1.5 mm containing an ohmic sheet absorber shown both with both end open and with one end closed.

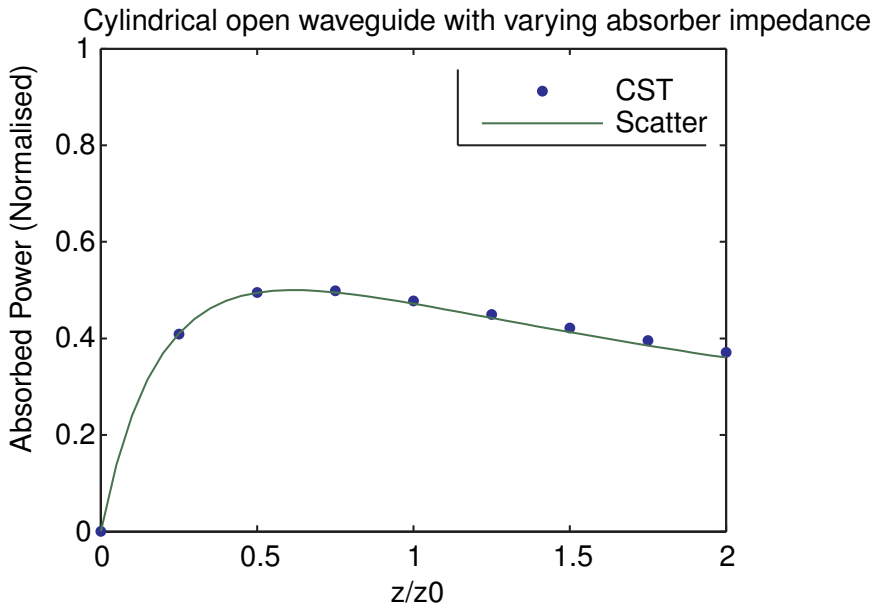

Figure 6.8: Total absorbed power for cylindrical open waveguide containing absorber halfway along its length as absorber impedance is varied.

between SCATTER and CST. In the figure, we plot the power absorbed by the ohmic sheet absorber. This is calculated by noting that the total power measured at both ports is given by:

$$Pow_{meas} = Abs(S_{11})^2 + Abs(S_{21})^2. \tag{6.1}$$

Now, if the total power in the system is normalised to 1, then the power absorbed by the absorber will simply be given by:

$$Pow_{abs} = 1 - (Abs(S_{11})^2 + Abs(S_{21})^2). \tag{6.2}$$

We note that the power absorbed by the ohmic sheet in this configuration reaches a maximum of about 0.5 at $0.75 \times z_0$ or 282.75Ω, i.e. half of the power is absorbed by the ohmic sheet at this point. Figure 6.9 shows the results of

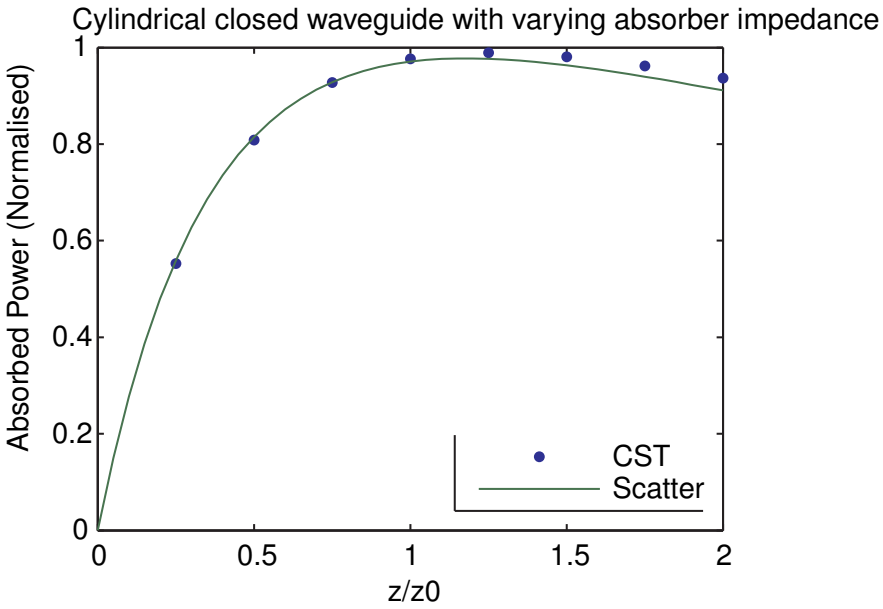

Figure 6.9: Total absorbed power for cylindrical closed waveguide containing absorber at $\lambda/4$ from the closed end as absorber impedance is varied.

the simulation for the closed waveguide with absorber placed at $\lambda/4$ from the closed end (figure 6.7(b)), and the absorber impedance is varied. We see that the $\lambda/4$ position does indeed seem to be a type of resonance, as the absorbed power reaches almost 100% at an absorber impedance of $1 - 1.25 \times z_0$. We again notice the excellent agreement, although we do also notice that the agreement becomes slightly less exact as the absorber impedance increases. However, even at the point of largest disagreement, the difference between the two values is of the order of 0.02, and the trend of the two "curves" still agree.

As we have verified the CST simulations for the waveguide with absorber

using SCATTER, we may now extensively carry out cavity simulations using CST, and trust that the analysis present is consistent with the equivalent mode matching analysis, which is always limited to simpler structures.

6.4 Cavity Analysis

We will perform simulations on a number of different geometries of cavity; namely circular and rectangular cavities. For both the circular and rectangular cavities, however, we will vary the type of input waveguide, using both a circular and rectangular waveguide, to investigate their effects on optical performance. We generally wish to use single-moded input waveguides. We shall also investigate the position of the absorber and its influence on the cavity power, realising a situation similar to SAFARI, where the cavity will contain a superconducting layer of tantalum metal. We assume throughout that the resistive sheet model of CST will accurately account for the physics of the absorbing tantalum layer. We will first look at the behaviour of an empty cavity fed by a waveguide. We will use just one type of cavity in this case as an introduction; a cylindrical cavity fed by a cylindrical waveguide, as a first example to introduce the correct analytical technique in CST. Figure 6.10 shows a schematic of the cavity setup being described. This is

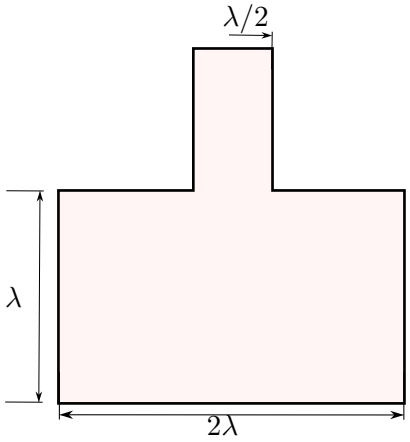

Figure 6.10: Cross section of empty cylindrical cavity, fed by a cylindrical waveguide.

a section through the cavity with waveguide. The cavity has a depth in the propagation direction of λ, the freespace wavelength, and has a radius of λ. The radius of the waveguide is $\lambda/2$ and it has a length of $\lambda/2$. The actual SAFARI cavity is larger in volume but due to the computational intensity of the calculation in CST we will limit the cavity size to keep the calculation

time reduced. Once the cavity is large enough to support multiple modes we should have a good insight into the nature of multi modes cavities. Also, if the problem is symmetric we can introduce symmetries in the computation to reduce the meshing volume to one quarter. Note the schematic drawing is not to scale. Figure 6.11(a) shows the result of the time domain simulation in CST of the empty cavity described with a circular waveguide. The S_{11} result oscillates around the 0 dB return value. Considering we are examining an empty cavity composed of PEC walls and containing no optically absorptive material, all of the power which enters the cavity should be reflected back out, when a steady state has been reached. The fact that the S_{11} osciallates around 0 dB suggests that a steady state solution has not been reached, with power at some frequencies still trapped within the system. This effect was discussed very briefly in section 2.9.1, i.e. that the time domain solver often exhibits these effects for highly resonant structures, due to the long settling time in reaching a steady state solution. Therefore, for this type of solution such as in an empty cavity where we expect a constant 0 dB return, we may expect that these oscillations may generally be ignored.

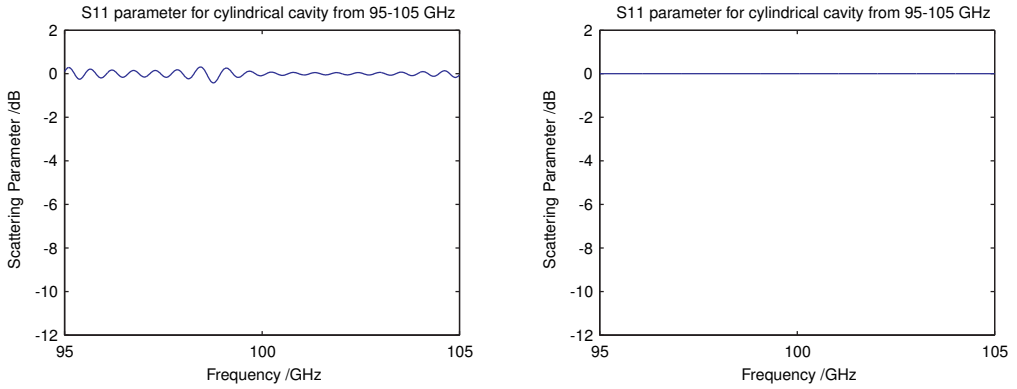

(a) S11 for empty cylindrical cavity using time domain solver.

(b) S11 for empty cylindrical cavity using frequency domain solver.

Figure 6.11: S11 for empty rectangular cavity using both time and frequency domain solvers over the range 95-105 GHz.

We can confirm this by examining figure 6.11(b), where we have performed the same simulation as 6.11(a), except in this case we have used the frequency domain solver, in its resonant mode, which gives us the S-parameters. The resonant S-parameter option of the frequency domain solver takes much less time to run than the general frequency domain solver, however this is still significantly longer than the standard time domain solver. We may generally then ignore the oscillatory nature of the S_{11} result about 0 dB in the time

domain solver, as we know the reasons for these oscillations.
We have examined the form of the returned power from an empty waveguide-fed resonant cavity. The comparison of both the time domain and transient solvers outlined in figure 6.11 shows that the frequency domain solver gives a more reliable representation of the S_{11} values for such a highly resonant problem. However, we wish to model the cavity containing absorbing material. In this type of situation there usually is no issue with using the time domain solver, as the problems reaching a steady state tend to be more noticable with highly resonant problems.

We will perform cavity simulations using an absorber where several parameters are adjusted, including:

1. Size of absorber
2. Shape of absorber, e.g. circular or square absorber
3. Position of absorber in the cavity.

These simulations will be carried out in varying cavity geometries, primarily:

1. Cylindrical cavity with cylindrical waveguide
2. Rectangular cavity with rectangular waveguide
3. Combination of cylindrical/rectangular geometries

To make a comparison of the frequency domain and time domain solvers for problems involving absorbers, we show an example here with the rectangular cavity with circular waveguide, and an absorber sheet filling the cavity at the halfway point in the propagation direction (figure 6.12). Note that the absorber sheet is realised by creating a material in CST of the type "ohmic sheet", with a surface impedance of 377 Ω.

Figure 6.12(b) shows the S_{11} results for both solvers. We note the almost identical values, with an apparent shift upwards in frequency of the effects when using the time domain solver. These differing results had been obtained previously, and steps were taken in an attempt to resolve the differences between the solvers. It was thought that the disparity between the results from both solvers was due to the time domain solver again having more trouble settling on a steady state solution and so the number of mesh cells

were increased and the adaptive meshing turned on. However, 6.12(b) is the results after these steps had been taken, and yet we still have a slight difference between the two results. The frequency domain solver is technically better and more accurate than the time domain solver, as it does not suffer from the same problems in reaching a steady state solution for highly resonant problems. However, when we are dealing with such a problem and it is advantageous in terms of time and computational efficency to use the time domin solver instead, we must be careful to realise that the fluctuations around 0 dB in the returned power are not physical, and merely a product of the simulation method. In any case, we will not often deal with such highly resonant problems that this is a significant issue. For the same physical problem, the difference in computational power required between the two solvers is very significant. An empty cavity problem performed using the frequency domain solver using the high end computer in the department will take of the order of 1 day to complete. The same problem using the time domain solver will usually take less than 1 hour to complete. Despite the shortcomings of the time domain solver in some cases then, it is our solver of choice for most problems, and if not explicitly stated, it is assumed that this is the solver that is being used.

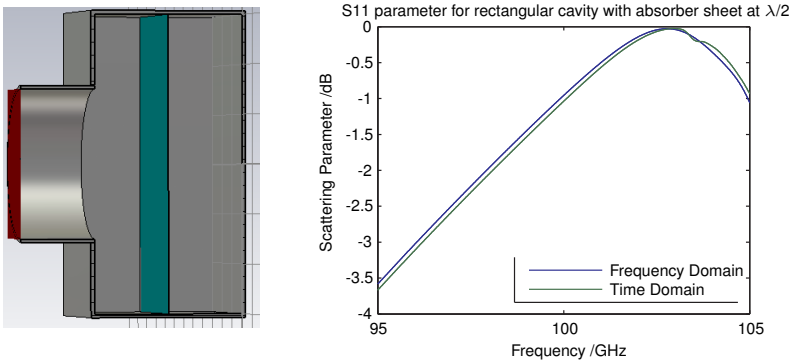

(a) CST CAD model of the cavity with the absorber sheet.

(b) S11 for square cavity with absorber using time and frequency domain solvers.

Figure 6.12: S11 for rectangular cavity with ohmic sheet absorber using both time and frequency domain solvers over the range 95-105 GHz.

We will now examine the optical behaviour of various cavity geometries with including absorbing material when illuminated through a single mode input waveguide, in terms of its S_{11} parameters.

6.4.1 Cylindrical Cavity with Cylindrical Waveguide

The first cavity type which we will examine in detail is that of a cylindrical cavity fed by a cylindrical single moded waveguide. The reason for this is that it is most similar to the waveguide examples considered in section 6.3 in verifying CST. We shall use a cylindrical cavity of radius λ, with a waveguide of radius $\lambda/2$ and length $\lambda/2$. This radius is chosen so that the waveguide will be single-moded at 100 GHz. The radius of the cavity as λ is relatively arbitrary, as it is indeed smaller in terms of wavelengths than the proposed SAFARI cavity, but we wish to use a smaller cavity for speed and efficiency of modelling. Also, the depth of the cavity will initially be λ. We will firstly vary the position of the absorber relative to the backwall or backshort of the cavity. Refer to figure 6.13. For example, if, in a simulation, if we wish the absorber to be placed at a distance $\lambda/10$ from the backshort, then if our initial total cavity depth is λ, our depth parameters for the cavity will have values of $z_1 = 9\lambda/10$ and $z_2 = \lambda/10$. We will initially vary the value of z_2 and perform a simulation for each value, in order to find the optimum position of the absorber relative to the backshort, i.e. the position at which the absorber absorbs most power. However, as we are varying z_2 we shall wish z_1 to remain constant, to avoid adjusting two variables simultaneously. Therefore, as z_2 increases while z_1 remains constant, the total depth of the cavity will clearly increase.

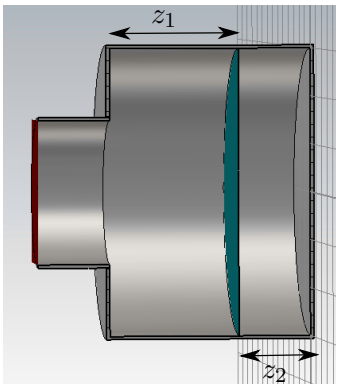

Figure 6.13: Illustration of the variable depth parameters, z_1 and z_2, applicable to all cavity geometries.

We begin then, using a cylindrical cavity with cylindrical waveguide in CST, and set z_1 to $9\lambda/10$. Then, we vary z_2 from $\lambda/10$ to λ in steps of $\lambda/10$, for a total of 10 simulations.

Figure 6.14 shows the S_{11} results for these 10 simulations. The S_{11} value

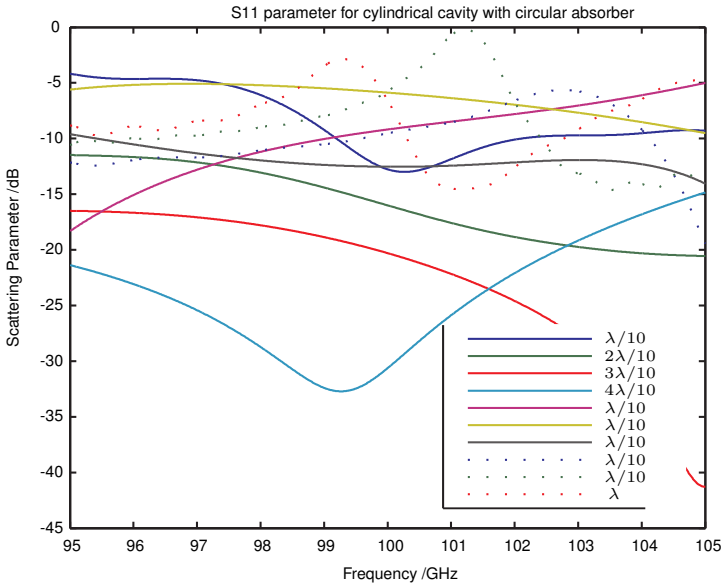

Figure 6.14: Plot of S_{11} for $z_1 = 9\lambda/10$, z_2 varying from $\lambda/10$ to $\lambda/$ for circular absorber in cylindrical cavity with cylindrical waveguide.

corresponds to the returned power (not absorbed), and so the best cavity for our purposes is the cavity with the lowest S_{11} over the bandwidth of interest. We will take the average value of the S_{11} over the band from $95 - 105$ GHz when searching for the optimum position. The reason for this is that it gives an indication of the performance of the absorber over what is still a narrow bandwidth, and is more representative of a physical situation. Table

Table 6.1: Average S_{11} values and absorbed power for varied z_2 position for $z_1 = 9\lambda/10$ over the frequency band $95 - 105$ GHz.

z_2 position	Avg. S_{11} /dB	Fractional Absorbed Power
$\lambda/10$	-8.5426	0.8601
$2\lambda/10$	-15.975	0.975
$3\lambda/10$	-22.749	0.995
$4\lambda/10$	-24.255	0.996
$5\lambda/10$	-9.9201	0.8981
$6\lambda/10$	-6.3788	0.7698
$7\lambda/10$	-11.921	0.936
$8\lambda/10$	-9.9597	0.8991
$9\lambda/10$	-8.8948	0.8710
λ	-8.4920	0.8584

6.1 shows the average S_{11} values and the corresponding fraction of power absorbed by the ohmic sheet in the cavity $(1 - Abs(S_{11})^2)$. We find that the position of the absober that gives the highest absorption is the absorber

located $4\lambda/10$ or 1.2 mm away from the backshort. For the single mode case outlined in figure 6.7 the value of $\lambda/4$ from the backshort gave the optimum absorption. Here of course the cavity can support more than one mode so the optimum distance is now different and we must find the best average position for all modes present.

Now that we have found the optimum value for z_2, we shall attempt to find an optimum value for z_1 also. Note: we must keep in mind that $4\lambda/10$ was found to be the optimum position of the absorber from the backshort while z_1 was also set to $9\lambda/10$. As we vary z_1, it may no longer be the case that $z_2 = 4\lambda/10$ is the optimum value. This is the complexity of simultaneously optimising for two mutually dependent parameters. However, we shall still attempt varying z_1 while fixing $z_2 = 4\lambda/10$ and observing the results.

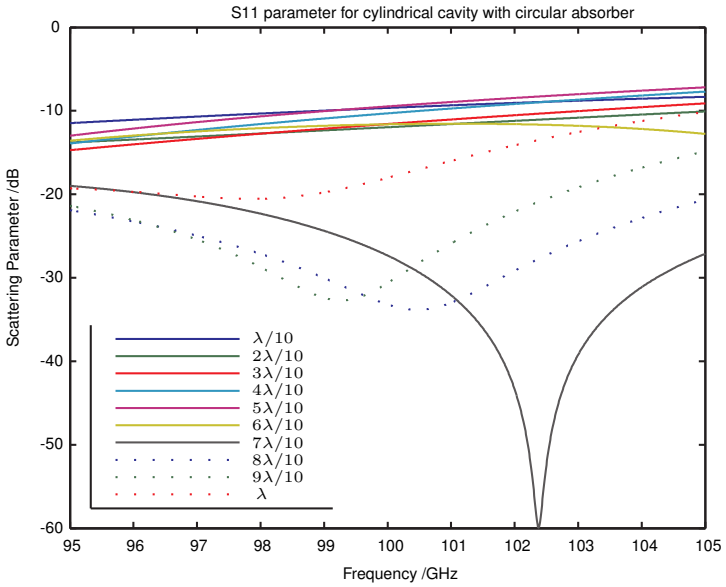

Figure 6.15: Plot of S_{11} for $z_2 = 4\lambda/10$, z_1 varying from $\lambda/10$ to λ for circular absorber in cylindrical cavity with cylindrical waveguide.

Figure 6.15 shows the results of varying z_1 while keeping z_2 fixed at $4\lambda/10$. On quick inspection, it would appear that the values of z_1 from $\lambda/10$ to $6\lambda/10$ give broadly similar results, while the values from $7\lambda/10$ to λ would appear to produce much lower S_{11} values, and hence higher absorbed power values. However, we shall again look at the average S_{11} values across the 95-105 GHz band, and the average absorbed power values. Table 6.2 shows these results. From the table, we find that the optimum position in terms of absorbed power is (marginally) $z_1 = 7\lambda/10$, and this is in fact the most prominent trace in the plot, with an apparent resonant dip at around 102.4 GHz. Our

Table 6.2: Average S_{11} values and absorbed power for varied z_1 position for $z_2 = \lambda/4$ over the frequency band 95-105 GHz.

z_1 position	Avg. S_{11} /dB	Fractional Absorbed Power
$\lambda/10$	-9.7329	0.8937
$2\lambda/10$	-11.955	0.936
$3\lambda/10$	-11.691	0.932
$4\lambda/10$	-10.470	0.910
$5\lambda/10$	-9.6703	0.8921
$6\lambda/10$	-12.110	0.938
$7\lambda/10$	-28.770	0.999
$8\lambda/10$	-27.069	0.998
$9\lambda/10$	-24.255	0.996
λ	-16.701	0.979

method of optimising both parameters individually then, appears to have yielded satisfactory results.

We now wish to examine the results of varying the absorber size. For the present time we will continue to use a circular absorber. For the previous simulations, we used an absorbing sheet having a radius which completely filled the cavity interior, i.e. having a radius of λ. Now, we shall adjust the size of the absorber by decreasing it from λ in steps of $\lambda/10$. We wish to investigate how large the absorber needs to be, i.e. what is the smallest radius at which it is still absorbing a significant amount of the power from the cavity, at these particular values of z_1 and z_2. Note that if the absorber was placed closer to the cavity entrance, we would expect to be able to make the absorber smaller without reducing the absorbing power as much as in this case. This is because most of the incoming radiation would be directly absorbed by the sheet without having been reflected around the cavity. The size of the absorber is limited in reality due to the dependency of the speed of the TES detector on the absorber size. A larger absorber is better for absorption but the heat capacitance increases and so the speed of the detector is reduced, which is not ideal.

Figure 6.16 shows the result of this simulation performed for an absorber having radius of λ, down to a radius of $\lambda/10$. We see that, as we decrease the absorber radius, the S_{11} value increases (i.e. absorbed power decreases) dramatically. We realise the effect the cavity plays, as when the power is free to reflect multiple times inside the cavity, such as when the absorber does not fill the majority of the cavity radius, the absorbed power decreases

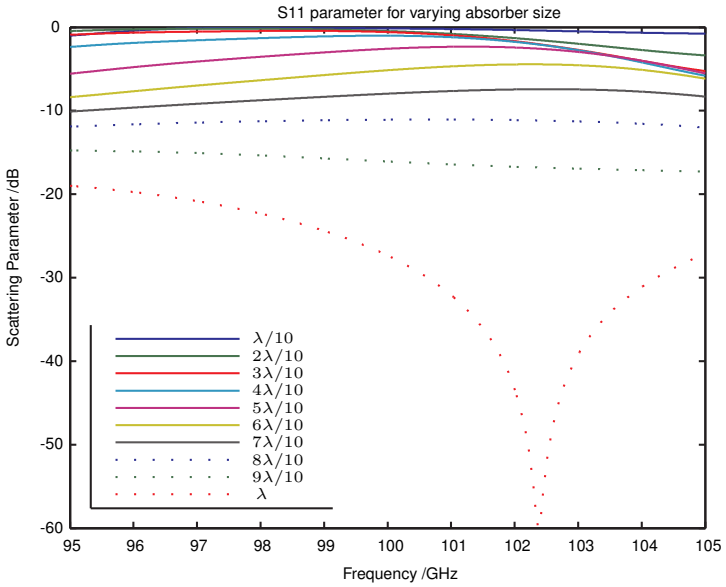

Figure 6.16: Plot of S_{11} for $z_2 = 4\lambda/10$, $z_1 = 7\lambda/10$ varying absorber radius from $\lambda/10$ to λ for circular absorber in cylindrical cavity with cylindrical waveguide.

dramatically. We note that the absorber is currently placed at a depth of $\lambda/7$ inside the cavity, and indeed the waveguide has a radius of $\lambda/2$. Therefore, even for an absorber having the same size as the input waveguide, after having travelled such a distance much of the incoming radiation will be missed by the absorber, as alluded to above. We wish then, to move the absorber closer to the input waveguide, to increase the absorbed power for an absorber whose radius is less than the total cavity radius. We already know that an absorber having radius of λ, i.e. completely filling the cavity, will absorb a very high level of power. As we wish to find an absorber size which is smaller than this and capable of absorbing high levels of power, we shall choose here an absorber of radius $7\lambda/10$, and move this absorber closer until we significantly increase the absorbed power. Then, we may wish to decrease the radius further, while still retaining high absorbed power, if possible. Figure 6.17 shows the results of these simulations. We notice that the absorbed power does not infact increase steadily and reach a maximum when the absorber is directly covering the cavity entrance, but instead fluctuates as the absorber is moved, reaching a maximum power absorbed at a position of $4\lambda/10$ inside the cavity entrance when the absorber radius $= 7\lambda/10$.

The next step is to fix the absorber at this position of $4\lambda/10$ inside the cavity and adjust the radius of the absorber, to examine the variability of the absorbed power as the radius is increased beyond this value of $7\lambda/10$, and indeed decreased to values which are smaller even than the input waveguide

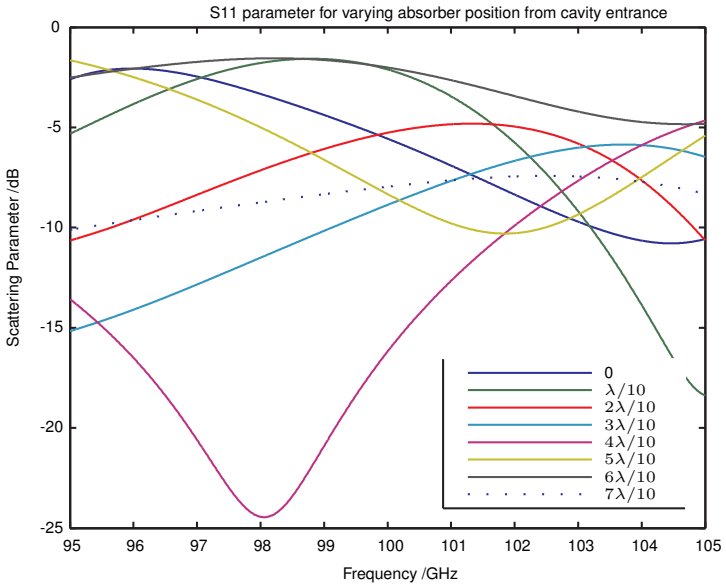

Figure 6.17: Plot of S_{11} for cavity depth of $11\lambda/10$ varying absorber position from the cavity entrance to $7\lambda/10$ inside the cavity for circular absorber in cylindrical cavity with cylindrical waveguide.

$(5\lambda/10)$.

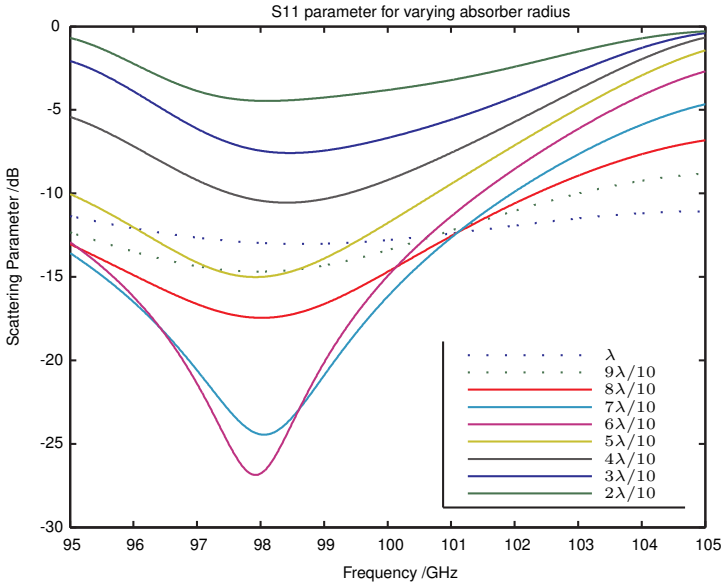

Figure 6.18: Plot of S_{11} for cavity depth of $11\lambda/10$ varying absorber radius at a position of $4\lambda/10$ from the cavity entrance for circular absorber in cylindrical cavity with cylindrical waveguide.

Figure 6.18 shows the results of this simulation for absorber radii ranging from λ down to $\lambda/5$. Table 6.3 shows the S_{11} averaged over the 95-105 GHz band, along with the correspinding average absorbed power values. We find that an absorber radius of either $6\lambda/10$ or $7\lambda/10$ gives broadly similar results.

Increasing beyond this provides no advantage, and indeed the absorbed power decreases. An absorber radius equal to that of the waveguide ($\lambda/2$) results in almost 90 % of the power being absorbed. As previously mentioned, when the radius is then increased to either $6\lambda/10$ or $7\lambda/10$ the absorbed power increases, presumably as the absorber needs to be larger than the waveguide when it is located a significant distance away from the waveguide to absorb maximum power, i.e. we need to fully illuminate the absorber. If the absorber is then larger than the incident beam initially perhaps the edges are shadowed and the effect of increasing size is not realised.

Table 6.3: Average S_{11} values and absorbed power for cavity depth of $11\lambda/10$ varying absorber radius at a position of $4\lambda/10$ from the cavity entrance over the frequency band 95-105 GHz.

Absorber radius	Avg. S_{11} /dB	Fractional Absorbed Power
λ	-12.182	0.940
$9\lambda/10$	-12.346	0.942
$8\lambda/10$	-13.016	0.950
$7\lambda/10$	-14.405	0.964
$6\lambda/10$	-13.752	0.958
$5\lambda/10$	-9.721	0.893
$4\lambda/10$	-6.857	0.794
$3\lambda/10$	-4.671	0.659
$2\lambda/10$	-2.703	0.463

It would seem clear then that an absorber having a radius of $6\lambda/10$ or $7\lambda/10$ inside such a cavity with a waveguide of radius $5\lambda/10$ is the optimum size.

Now that we have performed a range of simulations and optimised some parameters using an entirely circular geometry (i.e. cylindrical cavity, cylindrical waveguide, circular absorber), we wish to attempt to find similar levels of absorber efficiency for an equivalent entirely square geometry (i.e. rectangular cavity, rectangular waveguide, rectangular absorber).

What is evident from this analysis is that for a particular absorber size the cavity needs to be designed around it to maximise optical performance. Due to the size of the absorber setting the speed of the device this variable is usually set first and the cavity design is free to be optimised. The rule for the single moded case, which indicates that optimum absorption should be achieved when the absorber is $\lambda/4$ from the backshort no longer hold, and so

care must be taken in the optimisation of the geometry of these multi moded cavities.

6.4.2 Rectangular Cavity with Rectangular Waveguide

We now wish to take our results from 6.4.1 and attempt to recreate the optical performance using similar dimensions, but using an entirely different shaped geometry, i.e. we are moving from circular to Cartesian geometry. Naively we expect that a similar absorber area in a similar volume cavity should perform in a similar way, especially from a geometrical ray tracing point of view. We will now perform our simulations on a rectangular cavity with a rectangular input (single moded) waveguide. For simplicity, we wish our cavity to be symmetric, and so we shall use a cavity with a square cross-section. We shall also use a square waveguide, and hence we will use a square absorbing sheet. The cavity cross-section will be $2\lambda^2$, i.e. each side will have a length of 2λ. This is of comparable size to the cylindrical cavity previously examined, and is also within the limits of relatively manageable computational time with CST. We wish to use a waveguide which will be single-moded, that is it will only support the fundamental mode, for simplicity. We could use the standard WR-10 waveguide, with dimensions of 2.54 mm $\times$ 1.27 mm. However, for symmetry and simplicity purposes we would prefer to use a square waveguide profile. From analysing the port modes in CST for various sizes of waveguide, we have found that a waveguide having dimensions of 1.8 mm $\times$ 1.8 mm is effectively single moded at 100 GHz for rectangular waveguides. CST provides a method for examining which modes are present in a simulation, illustrated for this case in figure 6.19. It has two degenerate modes which are activated, or "cut on" at 83.2 GHz, and so these effectively equate to the same mode, but with a different polarisation in orthogonal directions. Also, making the length of the waveguide 3 mm or λ, as we have, ensures that some of the higher order modes which would activate at frequencies of around 166 GHz and above would not in fact be present in the cavity as they would have died off before reaching the inside of the cavity (become evanescent). There are also two other modes which would be activated at 117.7 GHz. As we are specifically chosing our simulation band as 95-105 GHz, these modes will not affect us. In any case, these modes would not affect our simulations as we have specifically chosen to only use one mode in our waveguide port in CST, as is the case through-

out all the simulations performed in CST. However, it is more appropriate for the general case to specifcally design the waveguide to only support one mode. We shall make a first attempt at an absorber simulation using a very

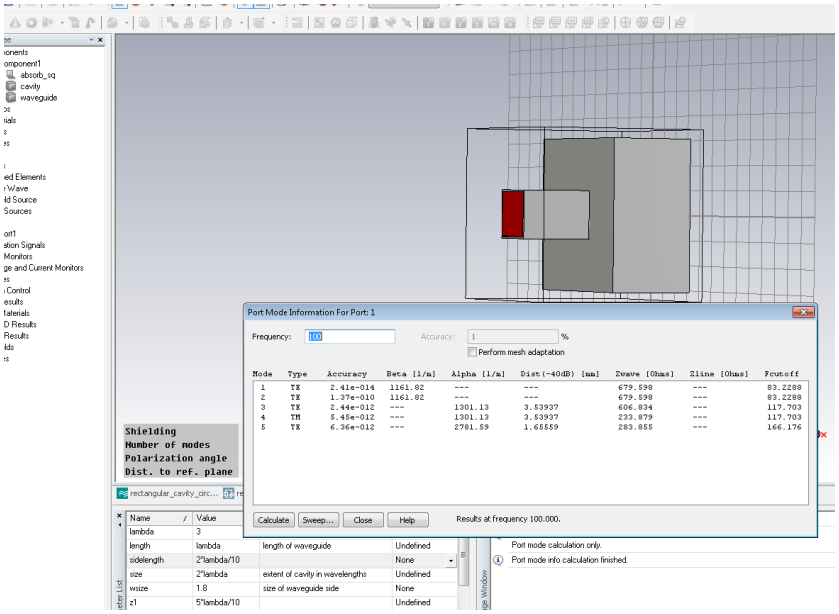

Figure 6.19: Illustration of port mode calculation facility in CST, in this case for a square waveguide of dimensions 1.5 mm $\times$ 1.5 mm excited with the first 5 modes.

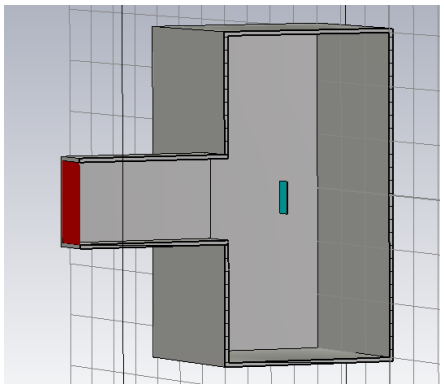

Figure 6.20: CAD model created in CST showing a rectangular cavity of cross-sectional area $2\lambda^2$ and depth $11\lambda/10$, with square absorber of side length $2\lambda/10$.

small square absober located $4\lambda/10$ from the cavity entrance.

Figure 6.20 shows the general setup here. A small absorber (side length $2\lambda/10$ is pictured.) We first attempt this simulation and the S_{11} result is shown in figure 6.21. We achieve fairly low levels of absorption (S_{11} of $-.675dB$ averaged across the band), as expected, as we have a very small absorber relative to the area of the waveguide and cavity.

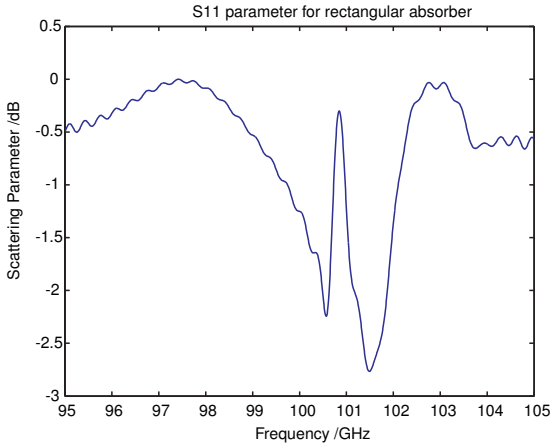

Figure 6.21: CST S_{11} result for rectangular cavity with rectangular waveguide containing square absorber of sidelength $2\lambda/10$.

Now, we wish to reproduce to some extent the results for the cylindrical cavity fed by a cylindrical waveguide, namely the result for the absorber of radius $7\lambda/10$ from figure 6.18, where the cavity has a depth of $11\lambda/10$ and the absorber is located at the position of $4\lambda/10$ from the cavity entrance. This was our optimum result for that cavity geometry, and it incurred quite a number of simulations and opimisation to achieve that result. We wish to perform the analogous simulation in a rectangular cavity of the same depth and with the absorber at the same location. The difference in this case will be that we are considering a rectangular asorber, rather than a circular one. The waveguide in this case has a much smaller cross-sectional area, but, as any size of empty perfectly resonant cavity should return 0 dB power, we assume that it is the size of the absorber relative to the size of the *waveguide* that is the key factor, rather than the absolute size of the absorber. We calculate that the optimum value of absorber radius ($7\lambda/10$) for the cylindrical cavity, corresponds to an absorber to waveguide cross-sectional area ratio of 1.96. Hence, for a square waveguide with cross-sectional area 1.8×1.8 mm^2, we require a square absorber of area 6.347 mm^2. This corresponds to an absorber sidelength of 2.52 mm. The result of the CST simulation of this setup is shown in figure 6.22, along with the result for the equivalent size circular absorber in the cylindrical cavity.

Clearly, the results are significantly different, with an average across the band in the rectangular case of -6.12 dB, compared with -14.41 dB in the cylindrical case. Also, in the rectangular case, the S_{11} approaches 0 dB briefly, indicating little or no power absorber around 103 GHz. It must be borne in

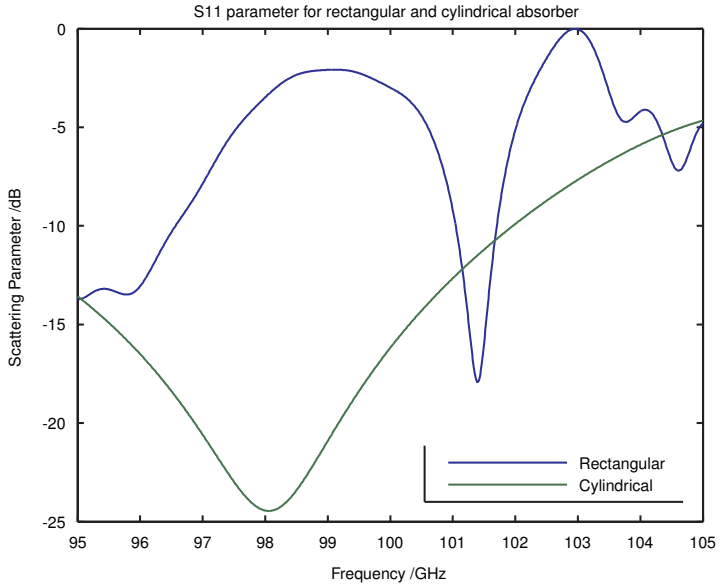

Figure 6.22: CST S_{11} result for rectangular cavity with rectangular waveguide containing square absorber of sidelength 2.52 mm.

mind, however, that the cylindrical cavity has being heavily optimised, and this has effectively been copied for the rectangular case, without the rigorous optimisation. It is clearly an oversimplification then, to asssume that the optimum result for the cylindrical case should translate directly to the rectangular cavity case. As a last example here we compare the case of the all-cylindrical geometry and the all-rectangular geometry, where the absorber fills the cavity and is located $4\lambda/10$ from the cavity entrance. This result is shown in figure 6.23. We first note that the result for the rectangular cavity is less consistent across the band. Also, it again almost reaches 0 dB at a frequency of around 103 GHz. When we calculate the average S_{11} values, it is found that, in the rectangular case, the average S_{11} is -9.17 dB, whereas in the cylindrical case the average is -12.17 dB. Again, clearly the cylindrical cavity has ben heavily optimised, whereas the rectangular cavity has not.

This initial analysis indicates that simple geometrical design rules for such an optical cavity will not work well and a full modal or electromagnetic analysis is required to optimise such structures at millimetre wavelengths.

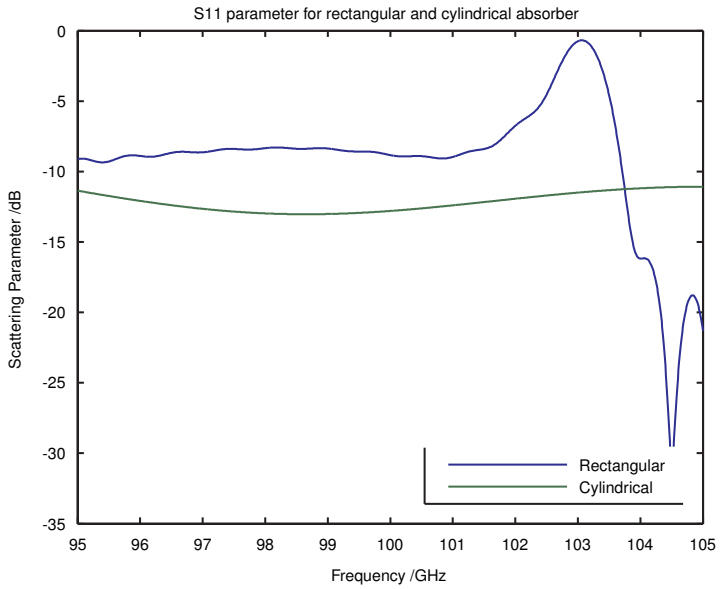

Figure 6.23: CST S_{11} result for comparing both rectangular and cylindrical cavities with an absorber filling the cavity at a location $4\lambda/10$ from the cavity entrance.

6.4.3 Cavity Variations

We have considered both a cylindrical and rectangular cavity. In each case these were fed by a waveguide of the corresponding geometry, i.e. the cylindrical cavity was fed by a cylindrical waveguide, and the rectangular cavity was fed by a rectangular waveguide. As an exercise, we will now briefly examine the effect of using the other two variation, i.e. rectangular cavity with cylindrical waveguide, and cylindrical cavity with rectangular waveguide.

Whereas we have previously rigorously optimised the cavity and absorber position and obsorber size, by performing up to around 40 unique simulations, at an excessive time cost, for these two case, we shall keep the analysis simple. We shall begin with our initial cavity of depth λ, and vary the position of the aborber inside this cavity, while keeping the cavity the same depth, and performing the simulation for three different absorber depths. This will give some small insight into these cavity geometries, and, as stated, these variations are in addition to the main analyses peformed in sections 6.4.1 and 6.4.2.

Rectangular Cavity with Cylindrical Waveguide

We shall first consider a rectangular cavity with a circular waveguide and containing an absorber sheet, as in figure 6.12(a). The cylindrical waveguide is chosen so as to be single moded at 100 GHz, with a radius of 1.5 mm. We will vary the geometry and the position of the absorber sheet within the cavity. Figure 6.24 shows the effect of varying the position of the absorber sheet in the cavity, for both a square absorber which is the size of the cavity ($2\lambda^2$), and the size of the waveguide radius (λ^2). Note, the convention is set so that the back wall of the cavity is the origin, so for example the position given as $\lambda/4$ is $\lambda/4$ from the back wall or *backshort* of the cavity, rather than from the entrance to the cavity.

Figure 6.24 shows the result of the time domain calculation using both a square absorber which completely fills the cavity (figure 6.24(a)), and which is the size of the input waveguide (figure 6.24(b)). Note: this is a square absorber and we have a circular waveguide, so when we say the absorber is the size of the waveguide, we mean it is a square of sidelength equal to the cylinder diameter, so that it is slightly larger in cross-sectional area than the waveguide.

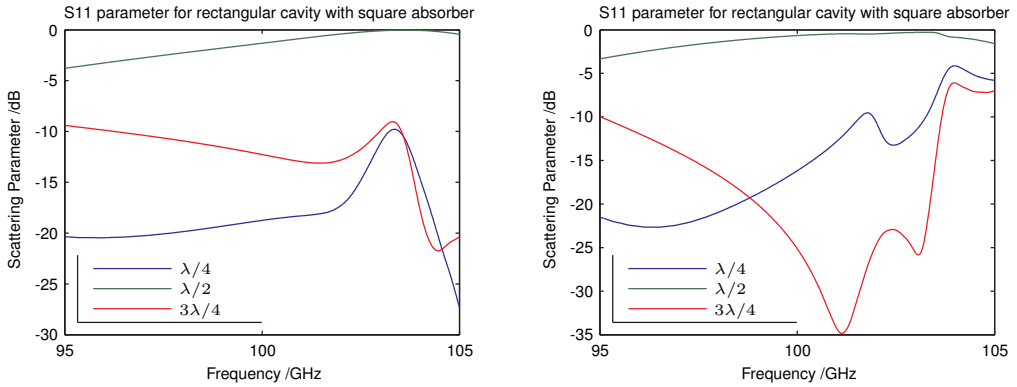

(a) S_{11} with varying position of square absorber of full cavity size.

(b) S_{11} with varying position of square absorber of waveguide size.

Figure 6.24: S11 for rectangular cavity with circular waveguide and square ohmic sheet absorber using time domain solver over the range 95-105 GHz.

Again, the results are not entirely geometrically predictable from the figure, we must average the S_{11} across the entire band. With reference to figure 6.24(a), the averaged S_{11} values for the various absorber positions are as follows: $\lambda/4$: -18.257 dB, $\lambda/2$: -1.480 dB, $3\lambda/4$: -12.291 dB. The absorber

position with the lowest S_{11} value, $\lambda/4$ from the backshort, corresponds to an absorption fraction of 98.5%. This is interesting, as we have not optimised the cavity size as rigorously as we had in secion 6.4.1, and yet we can obtain high levels of absorption. Were we to rigorously optimise this cavity geometry, or even to perform the simulation over a much larger number of absorber postitions, we would likely find a more optimum position for the absorber in relation to the backshort and increase the fraction of power absorbed. Again, this analysis suggests the resonant behaviour of the cavity is not predicatable and different geometries behave differently than expected.

Moving to an absorber of the size of the waveguide, we wish to examine the S_{11} results. With reference to figure 6.24(b), the averaged S_{11} values for the various absorber positions are as follows: $\lambda/4$: -15.455 dB, $\lambda/2$: -1.182 dB, $3\lambda/4$: -18.622 dB. In this case, the position (out of the 3 chosen positions) where we obtain the highest fraction of power absorbed is at $3\lambda/4$ ($\lambda/4$ from the entrance), with 98.6% of input power absorbed.

Cylindrical Cavity with Rectangular Waveguide

The second variation on a cavity with an alternate geometry of waveguide is a cylindrical cavity fed by a rectangular waveguide. This is again the same single moded waveguide as was used in section 6.4.2, having a square cross-section of 1.8×1.8 mm.

Figure 6.25 shows the results of the simulation for both an absorber completely filling the cavity (figure 6.25(a)), and an absorber of the same cross-sectional area as the waveguide (6.25(b)). Again, we first examine the case where the absorber completely fills the cavity. With reference to figure 6.25(a), the averaged S_{11} across the band values for the various absorber positions are as follows: $\lambda/4$: -14.955 dB, $\lambda/2$:-2.3486 dB, $3\lambda/4$:-13.767 dB. The position leading to highest absorption in this case is $\lambda/4$, with 97% of input power being absorbed. It is important to note from the figure that the position of lowest absortption is in around 102 GHz, and this is true of each absorber position, although we have chosen to examine the results across the band as a whole.

The final variation we shall examine here is for an absorber having the same cross-sectional area as the input waveguide, for the same three positions

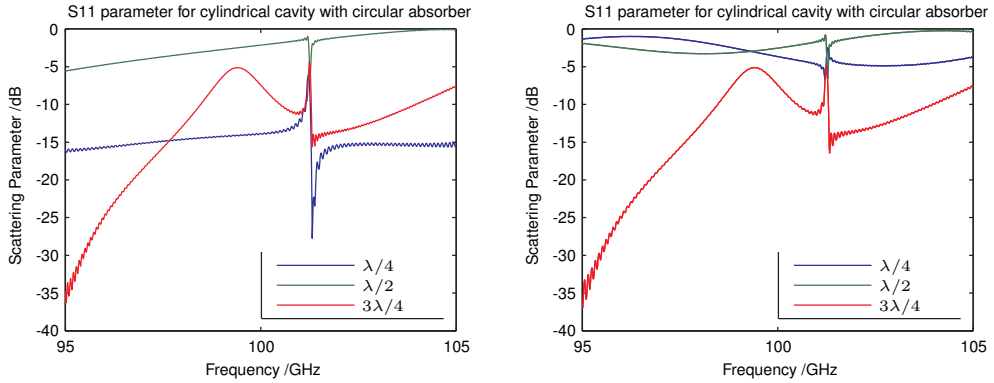

(a) S_{11} with varying position of circular absorber of full cavity radius.

(b) S_{11} with varying position of circular absorber of waveguide radius.

Figure 6.25: CST Time Domain Solver S11 profiles for circular cavity with rectangular waveguide for various absorber and dimensions over the range 95-105 GHz.

within the cavity. With reference to figure 6.25(b), the averaged S_{11} values for the various absorber positions are as follows: $\lambda/4$: -3.123 dB, $\lambda/2$:-1.946 dB, $3\lambda/4$: -13.769 dB. The absorber posiion leading to the lowest average S_{11} value is $3\lambda/4$ from the backshort, with (96%)of total input power absorbed. We note that in both the case where the absorber fills the cavity and where the absorber is the size of the waveguide, we achieve effectively exactly the same S_{11} result, indicating that as the absorber is located so close to the cavity entrance, the absorber is effectively obstructing the path for all of the input radiation.

In this brief examination of the two types of cavity which were not optimised in as much detail as the previous two cases, we have found that by performing a very low resolution variation of the absorber position throughout the cavity depth, we can gain some insight into the irregular behaviour of the cavity and perhaps by chance have found an appropriate position of the absorber within the cavity to obtain high levels of power absorption. Geometrical analysis of such cavities can clearly not be used to analyse their behaviour in this wavelength band.

6.5 Patch Antennas

Patch antennas, or *microstrip antennas*, are a class of antenna which have a low spatial profile, and for this reason they are also sometimes referred to as

planar antennas. To avoid confusion, we will generally always use the term "patch antenna". A patch antenna, then, consists of a thin metallic strip separated by a distance, h, from a metallic groundplane. The two metallic surfaces are separated by a dielectric substrate of thickness h, and $h << \lambda_0$, where λ_0 is the freespace wavelength of the radiation under consideration [48]. Figure 6.26 shows the operation of such an antenna. This example uses a microstrip line feed. Other methods exist, and another which will be considered in this chapter is coaxial probe feeding. The radiation is fed along the feedline to the patch, which has length L and width W. The patch is designed to radiate primarily in the direction normal to the patch, in this case the positive $x-$direction.

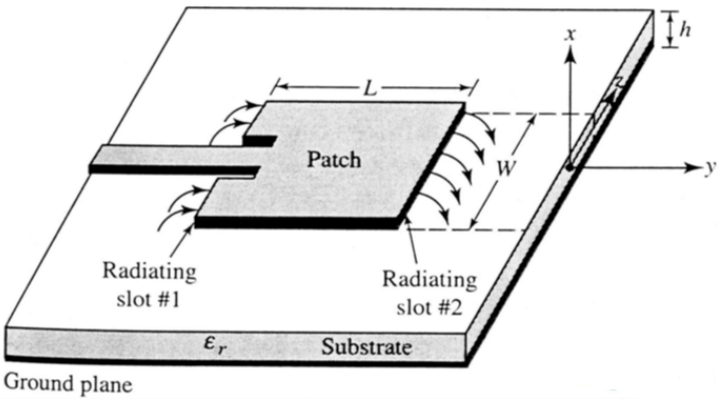

Figure 6.26: Schematic showing a patch antenna. Source: [48]

Patch antennas are generally simple and inexpensive to manufacture and can usually be created using printed circuit board technology. This, along with their low profile, is why they are commonly used in electronic devices such as mobile phones, along with having aerospace and military applications. It is also relatively simple to produce arrays of patch antennas. Some disadvantaqes of patch antennas include them having low efficency and a narrow bandwidth. For our purposes, we do not wish to operate the patch antenna as an actual radiating antenna, but as a receiver. More than this, we wish to potentially measure the field inside the cavity, without adversely affecting the cavity resonances, i.e. we do not wish to completely change the nature of the field inside the cavity by measuring it with the patch antenna.

The most common type of patch antenna is the rectangular patch, and so we shall choose to describe it in more detail here. We will use the transmission-line model.

Because the dimensions of the patch are finite, the fields at each edge of

the patch undergo *fringing*, i.e. the field exists outside the dielectric, and the effective dielectric constant is changed. The fringing is a function of the dimensions of the patch and the height of the substrate. The fringing effects may be seen in figure 6.26 at the edges of the patch. The effective dielectric constant, then, is given by:

$$\epsilon_{reff} = \frac{\epsilon_r + 1}{2} + \frac{\epsilon_r - 1}{2}\left[1 + 12\frac{h}{W}\right]^{-1/2}, \tag{6.3}$$

where ϵ_r is the dielectric constant of the substrate and W is the width of the patch. The extra length added to each edge of the patch due to the fringing effects, ΔL, may be found using expression 6.4 [48]

$$\frac{\Delta L}{h} = 0.412\frac{(\epsilon_{reff} + 0.3)\left(\frac{W}{h} + 0.264\right)}{(\epsilon_{reff} - 0.258)\left(\frac{W}{h} + 0.8\right)}. \tag{6.4}$$

For microstrip antennas, the ratio of the length, L, of the patch to the height, h, of the substrate is generally much greater than 1, and so fringing effects are reduced. To design a rectangular patch, we first specify the following parameters: ϵ_r, f_r, h/λ_0, where f_r is the resonant frequency and λ_0 is the freespace wavelength. The following set of equations may then be used to choose values for the dimensions of a rectangular patch:

$$W = \frac{c}{2f_r}\sqrt{\frac{2}{\epsilon_r + 1}} \tag{6.5a}$$

and

$$L = \frac{c}{2f_r\sqrt{\epsilon_{reff}}} - 2\Delta L. \tag{6.5b}$$

6.6 Patch Design

We will first design a rectangular patch antenna for operation at 100 GHz, using the formulae in 6.5 to calculate the parameters, and using CST to model the antenna. We wish to design a patch antenna which will be resonant at 100 GHz, and investigate its properties in free space before examining it inside a cavity. Using these formulae, and using a substrate of relative permittivity $\epsilon_r = 2$ and substrate thickness h=0.1 mm, we obtain a value for the width, W=1.225 mm, and the length, L=0.908 mm of the patch.

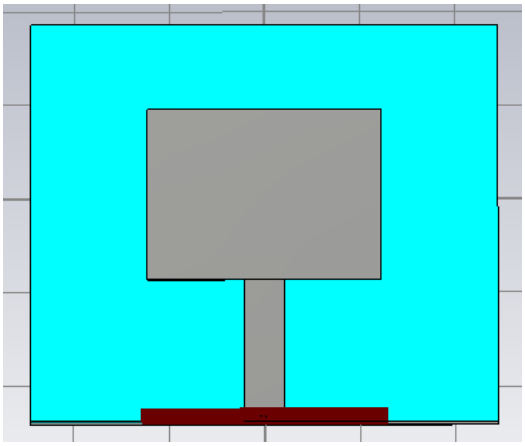

Figure 6.27: Rectangular patch designed for 100 GHz shown in the CST Microwave Studio enviroment.

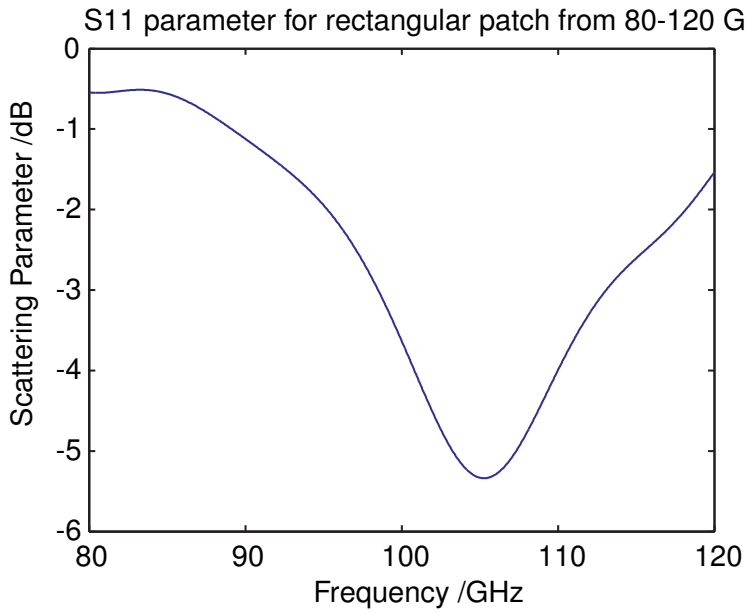

Figure 6.28: S11 in dB from 80-120 GHz for rectangular patch designed using equations 6.3-6.5.

Figure 6.27 shows the patch as it looks in the CST environment. The figure also shows the waveguide port which is feeding the patch. Figure 6.28 shows a plot of the resulting S11 calculation performed across a large band (80-120 GHz) for illustrative purposes. We note that, having designed this patch to operate at 100 GHz, the largest dip in the reflection parameter (S11) in fact occurs at around 105 GHz. The dip in the S_{11} indicates low return loss for launched power and therefore efficient radiation at this frequency as designed. This reflection dip is in fact quite wide and is much lower at 100 GHz than it is at say, 85 GHz, but nevertheless, this is not its resonant point. We must look more closely at the choosing of the parameters to optimize this antenna for 100 GHz, or at least closer to it than 105 GHz. If we now try ignoring the fringing effects in the calculations, we obtain W= 1.225 mm and L= 1.06 mm. When we simulate this using CST, we get the result as in figure 6.29. The resonant frequency is now lower, but it is much lower than 100 GHz, at around 93 GHz. We see then that the fringing influences the resonant frequency of the patch significantly, and ignoring the fringing is not feasible. As the formulae were not effective in designing for us a rectangular

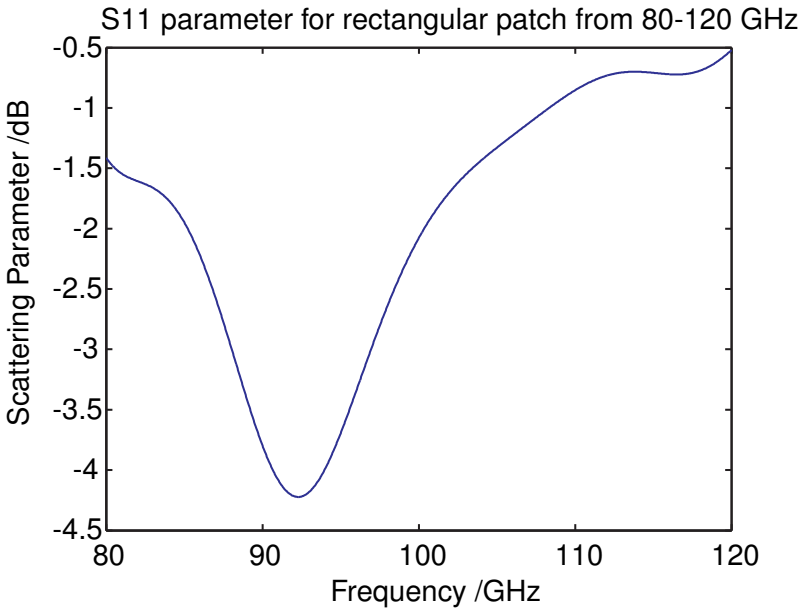

Figure 6.29: S11 in dB for rectangular patch designed ignoring fringing effects

patch with the desired resonant frequency, we will look at adjusting the patch size in an attempt to obtain resonance at 100 GHz.

By varying the parameters such that W= 1.225 mm and L= 0.966 mm, we now obtain the result as shown in figure 6.30. We now have a rectangular patch which has a reflection dip at around 100 GHz, as desired. We will also

examine the far field pattern of this antenna.

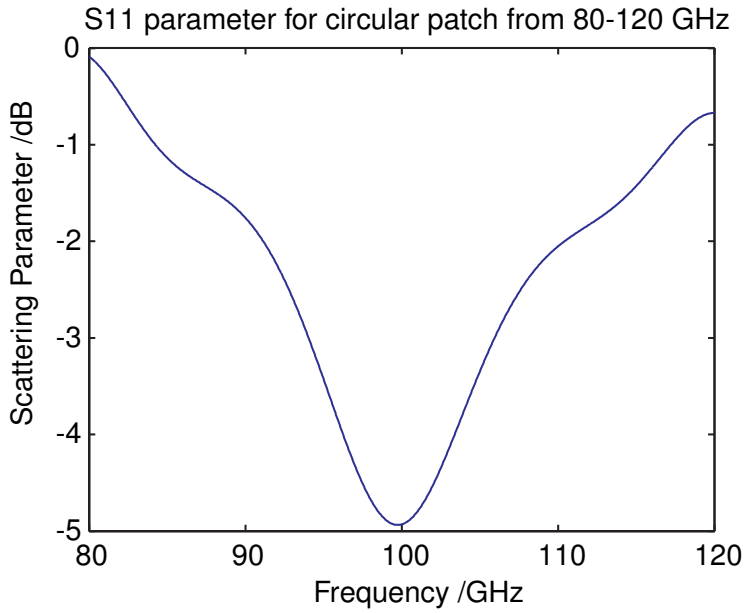

Figure 6.30: S11 in dB for rectangular patch designed by adjusting the length to obtain resonance at 100 GHz.

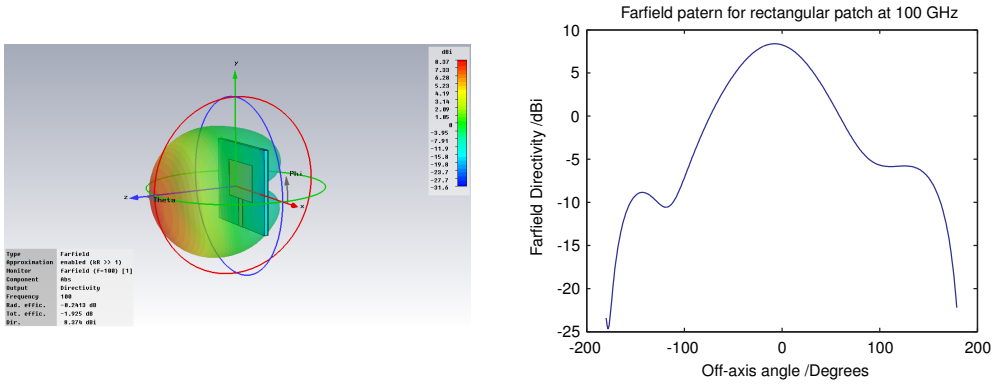

(a) 3-dimensional far field plot for the 100 GHz rectangular patch.

(b) 2-dimensional far field plot for the 100 GHz rectangular patch.

Figure 6.31: Far field patterns for 100 GHz rectangular patch.

Figure 6.31 shows the far field radiation pattern from the antenna. The important point to note here, and can be seen most clearly in the 3D plot of figure 6.31(a) is that the far field radiation pattern is strongest in the z-direction (the patch lying in the x-y plane). This shows that it is indeed operating as a patch antenna and radiating in this direction, despite being fed with radiation effectively along the y-direction. Figure 6.31(b) simply plots the same far field information using a 2D plot. Note that the farfield directivity scale is dBi, which is simply a comparison relative to an isotropic antenna, radiating uniformly in all directions.

Now that we have an antenna which works as desired at 100 GHz, this will be used later to perform further simulations. However, we would also like to examine and design another type of patch antenna to operate at 100 GHz. To this end, we shall now examine a circular patch antenna. From [48], we have an expression for the radius, a, is given by

$$a = \frac{F}{\sqrt{1 + \frac{2h}{\pi\epsilon_r F}\left[ln\left(\frac{\pi F}{2h}\right) + 1.7726\right]}} \tag{6.6a}$$

where

$$F = \frac{8.791 \times 10^9}{f_r\sqrt{\epsilon_r}}. \tag{6.6b}$$

Note: in equation 6.6a, the substrate height, h is given in cm. As well as a different geometry for the patch, an alternative feed method will be used; a coaxial feed. The CST help topics installed with the CST installation [23] provide a number of useful tutorials containg worked examples. Among these is an antenna tutorial which provides a step-by-step guide to constructing a coaxially fed circular patch antenna for operation at 2.4 GHz (see figure 6.32), and for performing simulations on same. Figure 6.33(a) shows the CAD model of the circular patch created in CST using the tutorial steps. The view is from the underside of the patch antenna, where the groundplane is hidden from view temporarily so that the outline of the patch can be seen, along with the cylinder housing the coax feed(seen slightly above the centre of the figure). This is then fed by a waveguide which is the size of the coax feed. Figure 6.33(b) shows the S11 parameter for the patch described. We

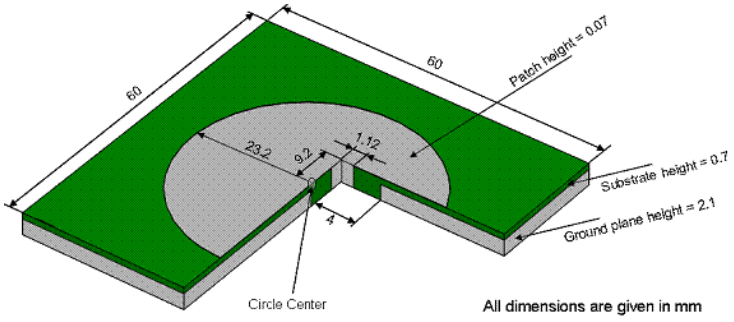

Figure 6.32: Screenshot from CST antenna tutorial showing coaxially fed patch antenna.[23]

note that it has a sharp dip in its reflection profile at around 2.4 GHz, as it was designed for. We now wish to create the same type of patch with a dip

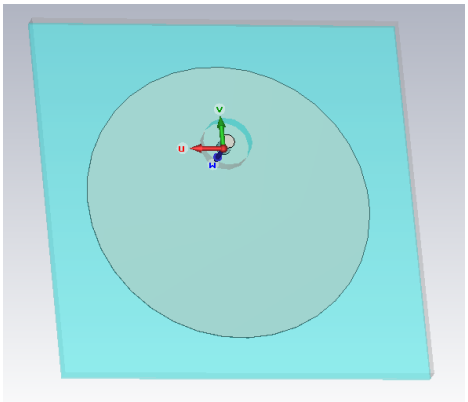

(a) CST CAD model of 2.4 GHz coaxially fed circular patch.

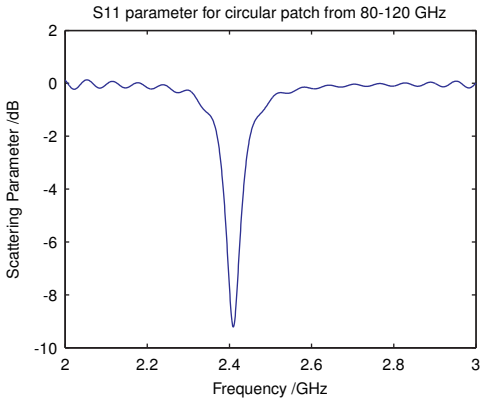

(b) S11 for circular coax fed patch at 2.4 GHz.

Figure 6.33: CAD model and S_{11} 2.4 GHz rectangular patch.

in reflection at 100 GHz, by simply scaling its dimensions by the scale factor appropriate for the difference in wavelength. This factor is

$$\frac{\lambda_{2.4GHz}}{\lambda_{100GHz}} = \frac{0.125}{0.003} = 41.67. \tag{6.7}$$

The radius of the circular patch given in the tutorial [23] is 23 mm. From application of equations 6.6 using the other stated parameters from the tutorial such as substrate height and permittivity, we obtain a radius of 23.46 mm. It would appear that the formula does not take into account fringing effects which adjust the resonant frequency.

The scaling factor mentioned in equation 6.7 in fact is based on the assumption that both patches use substrates of indentical relative permittivities. In fact this may not be as we would wish, for a strict comparison of the two alternative patch antenna geometries. As we have used a value of 2 for the rectangular antenna, we should do this also for the circular antenna. Then, we will scale the substrate height, etc. down to the correct size for the wavelength (i.e. scale by dividing by the factor of 41.67) and then find the appropriate radius using the formulae. Scaling the substrate and patch heights down to values appropriate for the shorter wavelength, and making the calculation for the radius using equations 6.6, we obtain a value for the radius of $a = 0.61mm$. Performing a simulation using this radius, we obtain the result in 6.34. We note that, in a similar way as for the rectangular patch, using the formulae has resulted in a patch with a resonant point which is not precisely at our desired frequency of 100 GHz.

Much as before then, we shall maually adjust the radius of the patch (along

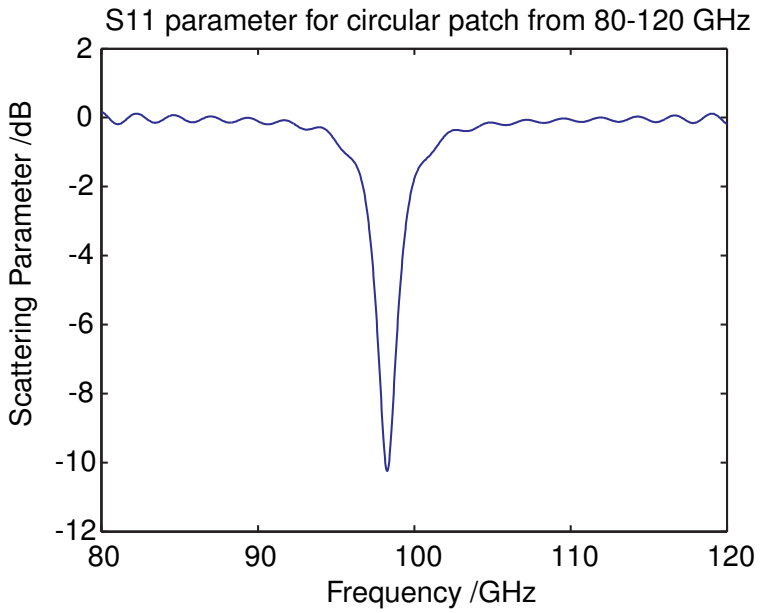

Figure 6.34: S11 for circular coax fed patch designed using equations 6.6.

with the radius of the coax feed). We find that decreasing the radius of the patch and feed increases the frequecy of the resonant dip in the reflection profile. We find that a radius of $0.596mm$ gives the desired result, i.e. we get a dip in the reflection profile at 100 GHz, as in figure 6.35(a). Figure 6.35(b) shows the far field pattern of the antenna. We note that in comparison to the 100 Ghz rectangular patch antenna (figure 6.31(b)), the antenna is radiating strongly in the z-direction, and the gain levels on-axis are broadly similar. However, the far field pattern for the circular antenna appears to be much more symmetric. The circular antenna is indeed more geometrically symmetric, in the sense that its radiating face is simply circular, and fed directly from behind this. Compare this to the rectangular feed option, where we have a strip of metal in the same plane as the radiating antenna, being fed in the plane perpendicular to the direction of radiation. We may not be surprised then, that the radiation pattern of such an antenna is not uniform, as some radiation may be actually radiated at points along the feedline. Also, the shape of the patch itself is not uniform in the x- and y-directions, whereas the shape of the circular patch is symmetric.

6.7 Patch Antenna in Cavity

Having examined both patch antenna designs in free space and resonant cavities containing absorber material, we must now turn our attentions to patch

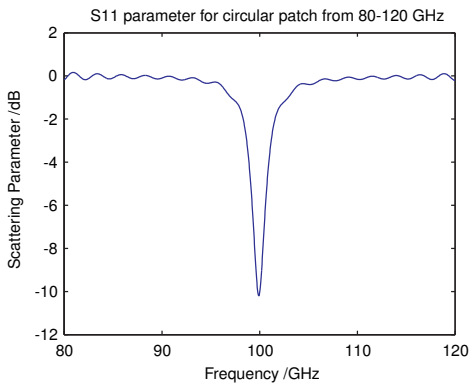

(a) S11 for circular coax fed patch at 100 GHz.

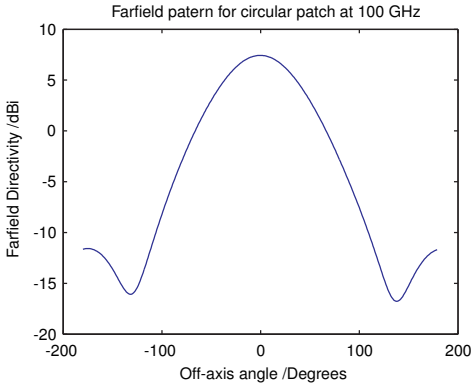

(b) Far field pattern for circular coax fed patch at 100 GHz.

Figure 6.35: S11 & far field pattern for circular patch at 100 GHz.

antennas situated inside the cavities themselves, as a means of measuring the field inside the cavity, as was our initial objective.
The use of a patch antenna within a cavity is an extremely novel technique to potentially analyse or get an insight into how the cavity behaves optically. The patch should actually act as a poor reception antenna, so as not to affect the cavity reflections and modes too much. This is the inherent problem of trying to "see" or measure the reflections within the cavity, as this cannot be done without affecting the result. We hope to have minimum disruption from the patch antenna.

The patch mounted in the back face of the cavity could detect the power incident at that point. If we can then mechanically rotate the back face of he cavity, we can potentially map out the field structure there and possibly gain some insights into the cavity multiple reflection structure.

6.7.1 Rectangular Patch Antenna

We begin initially with an empty resonant cavity fed by a waveguide port (port 1), and add the rectangular patch antenna designed for operation at 100 GHz from section 6.6, with its own waveguide port (port 2) to monitor the power received (Figure 6.36(a)), near the back face of the cavity. Figure 6.36 shows the result of the time domain simulation.

We are attempting now for the first time to use the patch antenna (specifically the waveguide port attached to its feed), as a detector, to monitor power

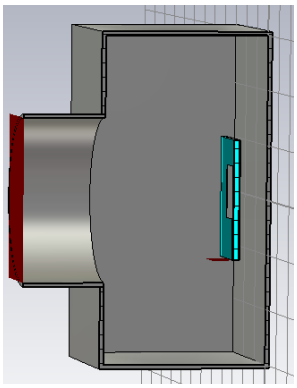

(a) CST CAD model showing rectangular 100 GHz patch inside a rectangular cavity fed by a circular waveguide.

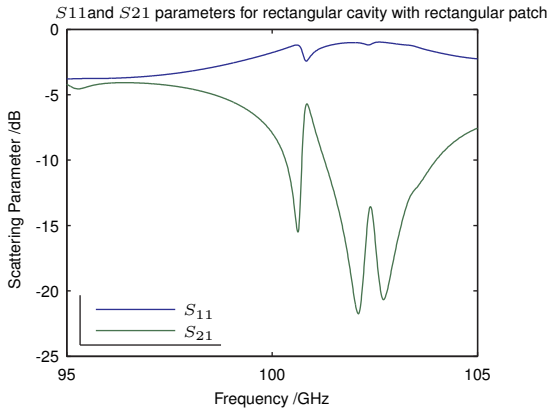

(b) S_{11} and S_{21} for the rectangular patch inside the rectangular cavity.

Figure 6.36: CST CAD model and Time Domain Solver S11 and S21 profiles for rectangular patch antenna inside over the range 95-105 GHz.

incident on the antenna and successfully coupled. We note that what we measure as the S_{21} does correspond to the S_{11} in that the frequencies at which we see maxima in the S_{11} are the same frequencies where we see minima in the S_{21}, and vice versa. Also, the presence of the patch antenna with its dielectric material reduces the S_{11} parameter of the cavity significantly, which was 0 dB return for an empty cavity of the same dimensions, suggesting that the patch has a level of influence that is quite significant.

Clearly, the S-parameters vary significantly across the band, and so it will be more illustrative to find the average value of each parameter between $95 - 105$ GHz. Performing this calculation, we find that the average S_{11} value is -1.522 dB, and the average S_{21} is -8.001 dB. By simply adding the patch into the cavity, the average returned power (S_{11}^2) decreases from 100% to 70.4%. Accounting for the contribution to this decrease due to the S_{21}, we find that the patch antenna itself (including dielectric material) seems to cause a decrease in overall measured power of 13.7%.

We also wish to investigate the effect of moving the location of the patch inside the cavity. Figure 6.37 shows the results of this. Again, it is more instructive to quote the average values. Also, it is the average S_{11} that is most instructive in quantifying the effect of the presence of the patch antenna in the cavity, as we already know that without anything present in the cavity

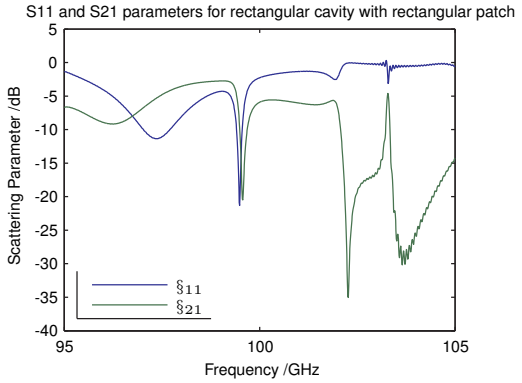

(a) S_{11} and S_{21} for rectangular patch in rectangular cavity moved to left side of cavity.

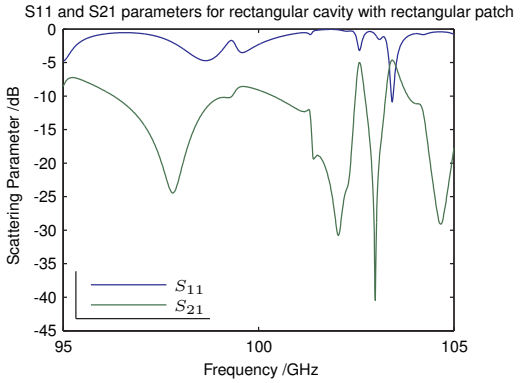

(b) S_{11} and S_{21} for rectangular patch in rectangular cavity moved to right side of cavity.

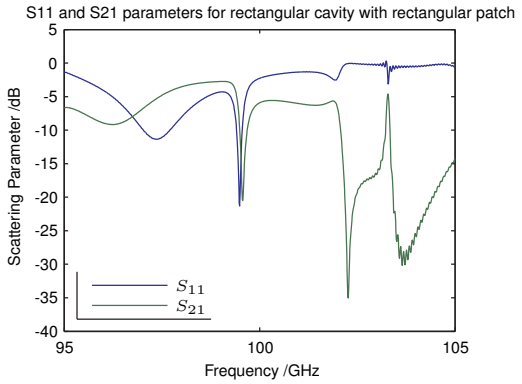

(c) S_{11} and S_{21} for rectangular patch in rectangular cavity moved to top of cavity.

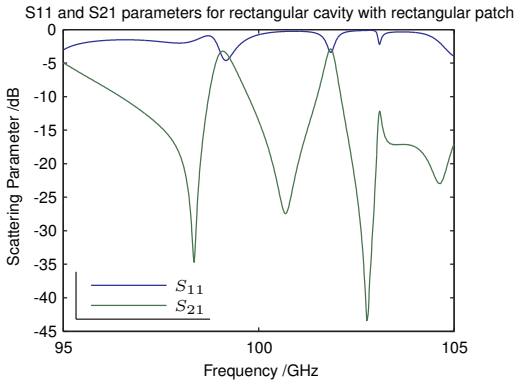

(d) S_{11} and S_{21} for rectangular patch in rectangular cavity moved to bottom of cavity.

Figure 6.37: CST Time Domain Solver S_{11} and S_{21} profiles for rectangular patch in rectangular cavity with the patch moved in each direction from the centre of the cavity over the range 95-105 GHz.

we have an average S_{11} value of 0 dB across the band. Table 6.4 shows these average values for the patch located at various positions inside the cavity, including the values discussed above (middle), and the corresponding values for the cases shown in figure 6.37. The presence of different S_{11} and S_{21} parameters suggests that there may be variation in the cavity field structure, but more rigorous analysis would be required to verify this.

We have examined placing the designed rectangular patch inside the cavity and monitoring the results. A circular patch has also been designed in section 6.6. This patch has not been integrated into the cavity, and this remains to be implemented in the future.

Table 6.4: Average S-parameter values and corresponding power values for cavity depth of $11\lambda/10$ containing a rectangular patch antenna at various locations in the cavity over the frequency band $95 - 105$ GHz.

Patch antenna location in cavity	Avg. S_{11} $/dB$	Fractional Measured S_{11} Power	Avg. S_{21} /dB	Fractional Measured S_{21} Power
middle	-1.5217	0.704	-8.0012	0.1584
left	-3.5848	0.4380	-10.2117	0.0952
right	-1.6943	0.6770	-13.9795	0.0400
top	-3.5848	0.4380	-10.2117	0.0952
bottom	-1.3838	0.7271	-14.8707	0.0326

Chapter 7

Conclusion

This thesis has been concerned broadly with the investigation and analysis of the principles and techniques which can be applied to millimetre-wave or terahertz optical systems. Specifically, the investigation of specific components applicable to these wavelengths was presented. A theoretical and experimental verification of non-dffracting axicons was presented and an outline of optical analysis for future detector devices was described, including an initial investigation of KID devices and waveguide coupled TES devices. An extension to Gaussian Beam Mode Analysis used to investigate cavities was also presented.

The background science of this specific region of the EM spectrum was described in context in Chapter 1, including a discussion of the current applications of the technology, especially for the application of astronomical receivers. The related background optical analysis theory was presented and developed in Chapter 2, and most tools and techniques that would be applied throughout the thesis were presented. An overview and description of the analytical techniques used in the commercial software CST Studio Suite®, a software package which would prove important in our analyses, was presented. Also, an overview of measurement techniques in millimetre-wave optics was given, specifically for the laboratory facilities at NUIM.

In Chapter 3 the principles of phase transforming elements were discussed, in particular axicons; quasioptical components capable of producing a highly collimated beam when incident Gaussian form radiation is incident upon them. Analysis of this particular element was performed using Gaussian

Beam Mode Analysis, an extremely useful analysis technique in the mm-wave region. This analysis described and built upon previous work described in [27]. Whereas in that work an off-axis elliptical mirror was used for initial beam collimation, our analysis employed a simpler system where the axicon was illuminated directly, suggesting possible use in much more compact systems where beam collimation is required or beneficial. Experimental measurements were performed to verify the analysis on such an axicon having a prism angle of 10°, and these were found to agree well with GBM simulations. Another axicon, with a prism angle of 20°, was designed and manufactured, and similar measurements performed on it. These measurements also verified simulations. It was found in each case that the measured beam had slight asymmetry on one side, indicating a possible alignment error in measurement setup, although this error has not been accounted for. Measurements were also performed using the same system without an axicon present, and in all cases it was found that the beam from the axicon was significantly more collimated and the potential use of axicons to collimate quasioptcical beams was illustrated.

In Chapter 4 the priciples behind a class of superconducting photon detector known as Kinetic Inductance Detectors (KIDs) were outlined and their use in astromomical applications was discussed, as well as the role that could be played by NUI Maynooth in developing front end optics for such devices. Investigations were made using plane wave analysis in CST, and this was outlined as a useful starting point in the optical analysis of such a system. In future work the optical analysis of KID devices will be undertaken using the plane wave analysis technique outlined here.

Chapter 5 discussed the extension of the standard GBM analysis to investigate multiple reflections in millimetre wave systems. The model simulated a corugated horn illuminating a system containing two metallic discs, the sizes of which were adjusted, and the reflection and transmision components were calculated as a function of distance between the rings. In this way standing waves produced between the rings were examined and found to occur at separation distances which were integral multiples of $\lambda/2$, where $\lambda = 3$ mm. Also, a method used for the analysis of standing waves between feedhorns [42] was adapted to investigate the form of the modes in the resonant Fabry-

Perot cavity. It was found that the cavity eigenmodes took the form of the Laguerre-Gaussian modes as expected, and the form of the reflected power component could be illustrated using this SVD technique briefly described.

Chapter 6 outlined the proposed SPICA mission and in particular SAFARI, an instrument onboard SPICA. A simplified cavity model which could potentially be manufactured for measurements to be performed in Maynooth was outlined. Significant use was made of the commercial software package CST, and this was initially compared with the inhouse mode matching solution SCATTER for verification purposes on a simple test case. A cylindrical cavity was manually optimised with an absorber sheet in order to obtain the optimum cavity size, and the optimum location and size of an absorber sheet within the cavity to maximise optical absorption was outlined. This was extrapolated for use within a cavity having a rectangular geometry, making assumptions based on a simple ray tracing approach, i.e. that the optimum cylindrical geometry may translate to a rectangular geometry without the need for independent optimisation. This was discovered to be an oversimplification, and in fact the optimum result for the cylindrical cavity did not translate directly to the rectangular geometry. This analysis indicates that the optical behaviour of these multimoded cavities cannot be described accurately using geometrical techniques and the use of full EM simulations such as CST or a modal analysis is required to accurately predict the optical efficiency of such waveguide coupled detectors. Brief analyses were also performed using alternating combinations of cavity and waveguide geometries, i.e. cylindrical waveguide with rectangular cavity, and rectangular waveguide with cylindrical cavity. A type of antenna known as a patch antenna was described. Such an antenna was highlighted as a potential detector to be used within our simplified physical model, and two different types of patch antenna were designed for use at 100 GHz. The rectangular patch antenna was investigated inside the cavity. It was found in this investigation that the location of the patch inside the cavity had an effect on the measured S-parameters, suggesting a possible variation in the cavity field structure incident on the patch. A more rigorous analysis is required here in the future, and also an ivestigation of the circular patch antenna within the cavity is required. The goal of this use of a patch antenna is to try to probe the cavity modes that exist in such waveguide structures. The patch antenna should be a poor antenna so as to not effect the cavity but yet return enough power to

potentially map out the cavity field by rotating the patch within the cavity. In the future it is hoped to investigate this experimentally by building on the analysis presented here.

Bibliography

[1] Laboratory of Laser Systems Novosibirsk State University. Diagram detailing electromagnetic spectrum, August 2012. Available: `http://www.nsu.ru/srd/lls/lls-pic/Electromagnetic_Spectrum.jpg`.

[2] Goutam Chattopadhyay, Ken B Cooper, Robert Dengler, Nuria Llombart, and Peter H Siegel. Imaging at a stand-off distance with terahertz FMCW radar. In *General Assembly and Scientific Symposium, 2011 XXXth URSI*, pages 1–1. IEEE, 2011.

[3] Kodo Kawase, Yuichi Ogawa, Yuuki Watanabe, and Hiroyuki Inoue. Non-destructive terahertz imaging of illicit drugs using spectral fingerprints. *Opt. Express*, 11(20):2549–2554, 2003.

[4] JB Jackson, M Mourou, JF Whitaker, IN Duling III, SL Williamson, M Menu, and GA Mourou. Terahertz imaging for non-destructive evaluation of mural paintings. *Optics Communications*, 281(4):527–532, 2008.

[5] Peter H Siegel. Terahertz technology in biology and medicine. *Microwave Theory and Techniques, IEEE Transactions on*, 52(10):2438–2447, 2004.

[6] SW Smye, JM Chamberlain, AJ Fitzgerald, and E Berry. The interaction between terahertz radiation and biological tissue. *Physics in medicine and biology*, 46(9):R101, 2001.

[7] Ruth M Woodward, Vincent P Wallace, Richard J Pye, Bryan E Cole, Donald D Arnone, Edmund H Linfield, and Michael Pepper. Terahertz pulse imaging of ex vivo basal cell carcinoma. *Journal of Investigative Dermatology*, 120(1):72–78, 2003.

[8] Robert K May, Michael J Evans, Shuncong Zhong, Ian Warr, Lynn F Gladden, Yaochun Shen, and J Axel Zeitler. Terahertz in-line sensor for direct coating thickness measurement of individual tablets during film

coating in real-time. *Journal of Pharmaceutical Sciences*, 100(4):1535–1544, 2011.

[9] ESA/Herschel/HIFI/J. Pineda et al. (2013). Tracers of molecular gas across the plane of the milky way, June 2013. Available: `http://sci.esa.int/herschel/51911-tracers-of-molecular-gas-across-the-plane-of-the-milky-way/`.

[10] ESA and the Planck Collaboration. Planck reveals an almost perfect universe, April 2013. Available: `http://www.esa.int/Our_Activities/Space_Science/Planck/Planck_reveals_an_almost_perfect_Universe`.

[11] Jean Kaplan et al. Qubic, a bolometric interferometer to measure the b modes of the cmb. *arXiv preprint arXiv:0910.0391*, 2009.

[12] A.E. Siegman. *Lasers*. University Science Books, 1986.

[13] Orazio Svelto and D.D.C. Hanna. *Principles of Lasers*. Springer, 1998.

[14] P.F. Goldsmith. *Quasioptical Systems: Gaussian Beam Quasioptical Propogation and Applications*. IEEE Press Series on RF and Microwave Technology. Wiley, 1998.

[15] James Christopher George Lesurf. *Millimetre wave optics, devices and systems*. CRC Press, 1990.

[16] Derek H Martin and John W Bowen. Long-wave optics. *Microwave Theory and Techniques, IEEE Transactions on*, 41(10):1676–1690, 1993.

[17] RJ Wylde. Millimetre-wave gaussian beam-mode optics and corrugated feed horns. *Microwaves, Optics and Antennas, IEE Proceedings H*, 131(4):258–262, 1984.

[18] HT Eyyuboğlu, Y Baykal, and X Ji. Scintillations of Laguerre Gaussian beams. *Applied Physics B*, 98(4):857–863, 2010.

[19] Créidhe O'Sullivan, John A Murphy, Marcin L Gradziel, John Lavelle, Tully Peacocke, Neil Trappe, Gareth S Curran, David R White, and Stafford Withington. Optical modelling using Gaussian beam modes for the terahertz band. In *Proc. of SPIE Vol*, volume 7215, pages 72150P–1, 2009.

[20] M. Whale. *Optical Characterisation of Astronomical Submillimetre Receivers including ALMA Bands 5 and 9.* PhD Thesis, NUI Maynooth, 2010.

[21] Max Born and Emil Wolf. *Principles of Optics: Electromagnetic Theory of Propagation, Interference and Diffraction of Light.* Cambridge University Press, 1999.

[22] CST. CST studio suite overview, May 2012. Available: `http://www.cst.com/Content/Products/CST_S2/Overview.aspx`.

[23] Computer Simulation Tecnology. *CST Studio Suite Help.* Computer Simulation Tecnology, 2012.

[24] E. McLoughlin. *Optimisation of a Near Field Scanning System.* Masters Thesis, NUI Maynooth, 2012.

[25] N. Trappe, M.L. Gradziel, C. O'Sullivan, and J.A. Murphy. New technology high efficiency horn antennas for cosmic microwave background experiments and far-infrared astronomy.

[26] N. Trappe. *Quasi-optical Analysis of the HIFI instrument for the Herschel Space Telescope.* PhD Thesis, NUI Maynooth, 2002.

[27] Neil Trappe, Ronan Mahon, William Lanigan, J Anthony Murphy, and Stafford Withington. The quasi-optical analysis of Bessel beams in the far infrared. *Infrared physics & technology*, 46(3):233–247, 2005.

[28] Martin S Heimbeck, Patrick J Reardon, John Callahan, and Henry O Everitt. Transmissive quasi-optical ronchi phase grating for terahertz frequencies. *Optics letters*, 35(21):3658–3660, 2010.

[29] James C Wiltse. Zone plate designs for terahertz frequencies. In *Defense and Security*, pages 167–179. International Society for Optics and Photonics, 2005.

[30] WM Lee, X-C Yuan, and WC Cheong. Optical vortex beam shaping by use of highly efficient irregular spiral phase plates for optical micromanipulation. *Optics letters*, 29(15):1796–1798, 2004.

[31] J Durnin. Exact solutions for nondiffracting beams. (i). the scalar theory. *J. Opt. Soc. Am. A*, 4(4):651–654, 1987.

[32] J Durnin, J Jr Miceli, and JH Eberly. Diffraction-free beams. *Physical Review Letters*, 58(15):1499–1501, 1987.

[33] Zhiping Jiang, Qisheng Lu, and Zejin Liu. Propagation of apertured Bessel beams. *Applied optics*, 34(31):7183–7185, 1995.

[34] Peter K Day, Henry G LeDuc, Benjamin A Mazin, Anastasios Vayonakis, and Jonas Zmuidzinas. A broadband superconducting detector suitable for use in large arrays. *Nature*, 425(6960):817–821, 2003.

[35] J Schlaerth, A Vayonakis, P Day, J Glenn, J Gao, S Golwala, S Kumar, H LeDuc, B Mazin, J Vaillancourt, et al. A millimeter and submillimeter kinetic inductance detector camera. *Journal of Low Temperature Physics*, 151(3-4):684–689, 2008.

[36] SJC Yates, JJA Baselmans, YJY Lankwarden, A Baryshev, HFC Hoevers, G Gerini, A Neto, DJ Bekers, R Barends, TM Klapwijk, et al. Antenna coupled kinetic inductance detectors for space based sub-mm astronomy. In *Ninteenth International Symposium on Space Terahertz Technology*, volume 1, page 140, 2008.

[37] Andrey Baryshev, Jochem JA Baselmans, Angelo Freni, Giampiero Gerini, Henk Hoevers, Annalisa Iacono, and Andrea Neto. Progress in antenna coupled kinetic inductance detectors. *Terahertz Science and Technology, IEEE Transactions on*, 1(1):112–123, 2011.

[38] I McAuley, JA Murphy, N Trappe, R Mahon, D McCarthy, and P McLaughlin. Applications of holography in the millimeter-wave and terahertz region. In *SPIE OPTO*, pages 79380H–79380H. International Society for Optics and Photonics, 2011.

[39] R. Colgan. *Electromagnetic and Quasioptcial modelling of horn antennas for Far-IR space applications*. PhD Thesis, NUI Maynooth, 2001.

[40] E Gleeson, JA Murphy, B Maffei, W Lanigan, J Brossard, G Cahill, E Cartwright, SE Church, J Hinderks, E Kirby, et al. Corrugated waveguide band edge filters for CMB experiments in the far infrared. *Infrared physics & technology*, 46(6):493–505, 2005.

[41] C.M.M. O'Sullivan and J.A. Murphy. *Field Guide to Terahertz Sources, Detectors, and Optics*. Field Guide Series. SPIE, 2012.

[42] Neil Trappe, Tim Finn, J Anthony Murphy, Stafford Withington, and Willem Jellema. Analysis of standing waves in submillimeter-wave optics. In *Integrated Optoelectronic Devices 2006*, pages 61200F–61200F. International Society for Optics and Photonics, 2006.

[43] S. Doherty. *Optical and Quasi-Optical Design and Analysis of Astronomical Instrumentation including a Prototype SAFARI Pixel.* PhD Thesis, NUI Maynooth, 2012.

[44] B. Jackson, J. van der Kuur, J.R. Gao, B.J. van Leeuwen, D. van Loon, R. den Hartog, and G. de Lange. *SAFARI Detector System Design Description.* Technical Description, 2012.

[45] Philip D Mauskopf, P Ade, J Beyer, M Bruijn, J Gao, D Glowaca, D Goldie, D Griffin, M Griffin, F Hoevers, et al. A TES focal plane for SPICA-SAFARI. In *Proceedings of the 21st International Symposium on Space Terahertz Technology (National Radio Astronomy Observatory, 2010) pp*, pages 246–255, 2010.

[46] SPICA Study Team Collaboration et al. SPICA assessment study report for esa cosmic vision 2015-2025 plan. *ESA/SRE (2009)*, 6, 2009.

[47] K.D. Irwin and G.C. Hilton. Transition-edge sensors. In *Cryogenic Particle Detection*, pages 81–97. Springer Berlin/Heidelberg, 2005.

[48] Constantine A Balanis. *Antenna theory: analysis and design.* John Wiley & Sons, 2005.